Title

Design of Carbon Nanotube Neuro-Sensor Corona Phase for Improved Biocompatibility and Neuromodulator Imaging

Author

Yang, Darwin

Publication Date

2020

Peer reviewed|Thesis/dissertation

Design of Carbon Nanotube Neuro-Sensor Corona Phase for Improved Biocompatibility and Neuromodulator Imaging

by

Darwin Yang

A dissertation submitted in partial satisfaction of the

requirements for the degree of

Doctor of Philosophy

in

Chemical Engineering

Graduate Division

University of California, Berkeley

Committee in Charge:

Professor Markita P. Landry, Chair
Professor Roya Maboudian
Professor Kaoru Saijo

Fall 2020

Design of Carbon Nanotube Neuro-Sensor Corona Phase for Improved Biocompatibility and Neuromodulator Imaging

By

Darwin Yang

Abstract

Design of Carbon Nanotube Neuro-Sensor Corona Phase for Improved Biocompatibility and Neuromodulator Imaging

by

Darwin Yang

Doctor of Philosophy in Chemical Engineering

University of California, Berkeley

Professor Markita Landry, Chair

Single-walled carbon nanotubes (SWCNT) are an emerging nanomaterial platform enabling promising advances in biomolecular imaging. Noncovalent modification of SWCNTs with amphiphilic ligands reveals intrinsic SWCNT near-infrared fluorescence and imparts molecular recognition. In particular, SWCNTs wrapped with DNA oligonucleotides develop selective fluorescent response to catecholamine neurotransmitters such as dopamine. Consequently, these DNA-SWCNT probes have been applied for recording dopamine activity in brain tissue. However, two major barriers to *in vivo* application of SWCNT dopamine probes exist. Firstly, DNA-SWCNTs are highly susceptible to biofouling by protein adsorption reducing efficacy of sensors *in vivo*. Secondly, the impact of these artificial nanomaterials on biological environments remains poorly understood. Towards the first point, we develop a novel method for the study of biomolecular adsorption to the SWCNT surface utilizing the fluorescence quenching ability of carbon nanotubes to track adsorption of fluorophore-conjugated biomolecules. We leverage multiplexing using dissimilar dyes conjugated to each molecular species in order to simultaneously monitor the competitive adsorption/desorption of proteins and single-stranded DNA, respectively. Here we show that attenuation of dopamine response is largely due to protein adsorption rather than DNA desorption. Furthermore, we identify fibrinogen as a ubiquitous protein with high affinity to the SWCNT surface.

Next, we study the effects these SWCNT probes may elicit once implanted in brain tissue. Here we utilize microglial cells as a model for neuroinflammation. Microglia are the specialized immune cells of the central nervous system which are central in maintaining the homeostasis of the neuronal environment. Microglia are activated by interaction with foreign or pathogenic material, mediating and propagating inflammatory responses throughout the brain which can elicit downstream neurotoxicity and neurodegeneration. Examining the interactions between this cell type and carbon nanotube neuro-sensors is crucial in characterizing and quantifying the net biological impact of these probes on surrounding brain tissue. We utilize high-throughput sequencing and live-cell imaging to show that exposure to SWCNT probes induces significant upregulation of inflammatory signaling pathways and cell morphology change in SIM-A9 microglia. Although inflammation response is lower in magnitude than that provoked by inflammatory simulants such as lipopolysaccharide, SWCNTs uniquely induced drastic changes

to cell morphology, where cells exposed to SWCNTs progressed from round and motile states to highly ramified and stationary within several hours. These effects suggest activation of microglia into pro-inflammatory phenotypes by SWCNTs. This must be minimized in order to accurately study chemical signaling in the brain.

Subsequently, we devise strategies for noncovalent passivation of exposed SWCNT graphene lattice to improve biocompatibility. We apply protein adsorption and microglial activation as metrics by which to test noncovalently modified SWCNT catecholamine sensors. We find that passivation of DNA-SWCNTs using PEGylated phospholipid significantly decreases nonspecific protein adsorption and SWCNT-induced microglial ramification. These passivated neuro-sensors are then applied to image striatal dopamine release and reuptake events in excised mouse brain tissue. We show that brain slices labeled with passivated neuro-sensor exhibited both improved diffusivity through tissue and higher fluorescence response to dopamine release over unmodified SWCNT probes. Hence, we present three stages of development and optimization of a carbon nanotube-based neuro-sensor through design of the nanoparticle corona phase. The methodologies presented here are readily translatable to other bionanotechnologies and represent an advancement in the field of nanomaterial biosensors for molecular imaging.

Table of Contents

Acknowledgements

Thank you to my PhD advisor Professor Markita Landry for your tireless and unending support. I am forever grateful for the care and attention you gave to my research project as well as my personal growth as a scientist.

I would like to thank all the members of my qualifying and dissertation committee members, Professor Roya Maboudian, Professor Wenjun Zhang, Professor Lydia Sohn, and Professor Kaoru Saijo, for their academic and scientific mentorship.

Thank you to Sigrid Allen and Carlet Altamirano for helping me navigate through the PhD process.

Thank you to Dr. Jackson Travis Del Bonis-O'Donnell, Sarah Yang, and Rebecca Pinals for collaborating with me both in science and in classical music.

A special thank you to Dr. Abraham Beyene, Dr. Linda Chio, and Dr. Gözde Demirer for supporting me ever since the first day of the lab.

Thank you to my Berkeley friends and housemates over the years with whom I travelled to four new countries and embarked on countless adventures.

I would like to acknowledge the National Science Foundation for their financial support.

Finally, I would like to thank my family for instilling a love of science in me from an early age. This work would not have been possible without their continued love and support throughout the years.

Abbreviations

Abbreviation	Full Description
SWCNT	Single-walled carbon nanotube
MWCNT	Multi-walled carbon nanotube
ssDNA	Single-stranded DNA
nIR	Near-infrared
PBS	Phosphate-buffered saline
DA	Dopamine
HSA	Human serum albumin
FBG	Fibrinogen
FAM	Fluorescein amidite
Cy5	Cyanine-5
SDBS	Sodium dodecylbenezenesulfonate
LPS	Lipopolysaccharide
TLR	Toll-like receptor
LDH	Lactate dehydrogenase
MS	Mass spectroscopy
AAV	Adeno-associated virus
GO	Gene ontology
MDS	Multidimensional scaling
GSEA	Gene set enrichment analysis
MSigDB	Molecular Signatures Database
PEG	Polyethylene glycol
PE	Phosphoethanolamine
RT-qPCR	Quantitative reverse transcriptase PCR
ACSF	Artificial cerebrospinal fluid
LAL	Limulus amoebocyte lysate
HiPCO	High pressure carbon monoxide

Chapter 1:
Single-Walled Carbon Nanotubes

1.1 Introduction

Carbon nanotubes are graphene carbon lattices in a high aspect ratio cylindrical configuration. Single-walled carbon nanotubes (SWCNT) comprise a single graphene layer and exhibit diameters on the order of 1 nm with typical lengths from 0.4 to 1.2 μm. The unique properties of this emerging class of nanomaterials has led to its widespread use in biomolecular delivery, molecular sensing, and fluorescence imaging.[1–3] The latter two applications utilize the bandgap photoluminescence of SWCNTs. This property is dependent on the semiconducting properties of SWCNTs which arise from their unique geometries. SWCNTs are inherently chiral molecules, with each enantiomer assigned a chiral vector or angle describing orientation of the hexagonal graphene lattice around its axis. Chiral angle ranges from 0° to 30° and are constrained by the cylindrical geometry. Carbon nanotubes with mirror symmetry within the graphene lattice (chiral angle = 0° or 30°) are classified as metallic and do not display photoluminescence upon absorption of incident light due to immediate exciton extinction by non-localized electrons. SWCNTs with other allowed chiral angles are semiconducting and vary in both geometry and optical properties leading to absorbance and fluorescence spectra in which distinct peaks correspond to SWCNTs with correspondingly distinct geometries, namely diameters (**Figure 1.1a**). Subsequent spectral deconvolution can then be applied to independently study the interactions of molecules with distinct SWCNT chiralities.[4,5]

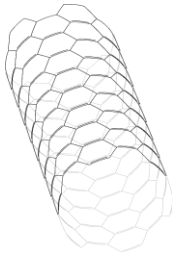

For all such chiralities, photoluminescence occurs within a region of the electromagnetic spectrum termed the near-infrared (nIR) window in which absorption of light by water and scattering by blood and tissues is minimized (**Figure 1.1a**). Consequently, greater depth of fluorescence imaging in biological tissues is enabled by use of these materials.[6] Furthermore, SWCNT bandgap photoluminescence is not subject to photobleaching, a phenomenon by which excessive excitation leads to degradation of fluorophores (**Figure 1.1b**). As such, SWCNT fluorescence can be imaged for significantly longer lifespans compared to traditional nIR fluorophores such as indocyanine green, which undergoes photobleaching within seconds of continuous laser excitation. This carries immediate benefits for the long-term imaging of SWCNTs including for *in vivo* applications.

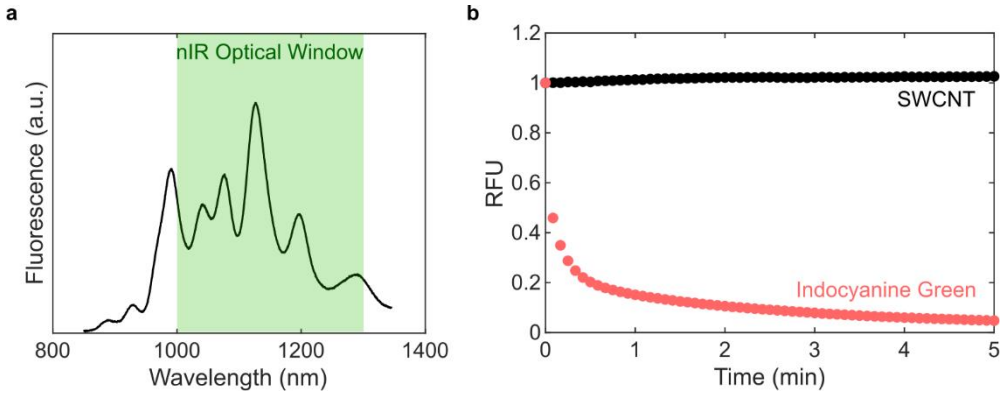

Figure 1.1 Near-infrared photoluminescence of single-walled carbon nanotubes. (a) nIR fluorescence spectra of $(GT)_6$ ssDNA wrapped SWCNTs with 721 nm laser excitation. Green shaded region represents nIRII optical window for brain imaging.[7] **(b)** Comparison of integrated fluorescence spectra (850 – 1350 nm) of $(GT)_6$-SWCNT vs. indocyanine green. Relative fluorescence values are normalized to the initial time point.

SWCNTs act as scaffolds by which physisorption of ligands can impart colloidal stabilization and molecular recognition to the resulting SWCNT suspension. Many diverse types of molecules can be used for this application, encompassing nucleic acids,[8,9] enzymes,[10] phospholipids,[11] and peptoids.[3] SWCNTs have been covalently and non-covalently modified with these ligands to develop nanoscale sensors for neurotransmitters,[2,12,13] dissolved gases,[14] proteins,[11,15] and carbohydrates.[3,16] Changes to the SWCNT nIR fluorescence spectra induced by analyte binding allow for aforementioned spectroscopic and microscopic detection.

This work will focus on the case of DNA-wrapped SWCNT neurotransmitter probes. Specifically, I present the development of a selective catecholamine nanosensor for imaging of dopamine release in the dorsal striatum of excised mouse brain tissue.

1.2 Singled-Walled Carbon Nanotube Neuro-Sensors

Signaling in the central nervous system is mediated through various mechanisms. Electrical transmission occurs via action potentials, directional changes in neuron membrane potential which propagate along neuronal axons. Action potentials trigger voltage-gated calcium channels at the terminals of neurons which leads to vesicular release of chemical neurotransmitter into the synaptic cleft. Neurotransmitters then bind to receptors on the postsynaptic neuron, propagating the signal via chemical transmission. Catecholamine neurotransmitters such as dopamine and norepinephrine belong to a subset known as neuromodulators. These molecules are distinct in that they diffuse out of the synapse and can impart long range effects on populations of neurons. Neuromodulation by molecules such as dopamine is involved in many higher order processes such as learning and memory.[17] However, much is still unknown about the role of dopamine in these phenomena and how neuromodulation is affected by neurodegenerative diseases such as Parkinson's disease and Alzheimer's disease.[18] As such, development of neuromodulator probes is highly desirable.

A nanosensor platform for detection of specific neuromodulators provides several immediate benefits. Firstly, release of chemical neurotransmitter is a highly stochastic process.[19] Therefore, imaging of extracellular neurotransmitter offers a more direct method of studying communication between neurons in the brain compared to monitoring of brain electrical activity.

Secondly, diffusion of neuromodulators out of the synapse results in activity which occurs over large distances and timespans throughout the brain tissue. Therefore, methods with high spatiotemporal resolution such as fluorescence microscopy offer substantial benefits.

Many novel fluorescent tools have been developed to image calcium release and electrical potentials across cell membranes. These tools allow for imaging of large fields of view containing multiple neurons, however, they do no directly measure chemical neurotransmission. Recently, several genetically encoded tools have been developed for imaging of dopamine and serotonin.[20] However, these approaches require transfection of cells using viral vectors, an inefficient and difficult process. New advances in single-walled carbon nanotube neuro-sensors has resulted in the development of a fluorescent probe with selective molecular recognition for catechoamines.[21]

SWCNTs noncovalently modified with single-stranded DNA become fluorescently responsive to the neuromodulator dopamine. Interaction of dopamine with the DNA phosphate backbone and SWCNT carbon lattice induce a large increase in SWCNT nIR fluorescence (**Figure 1.2**). The magnitude of response is dependent on the sequence of DNA, with sequence optimization revealing a maximal response for $(GT)_6$ DNA.[12]

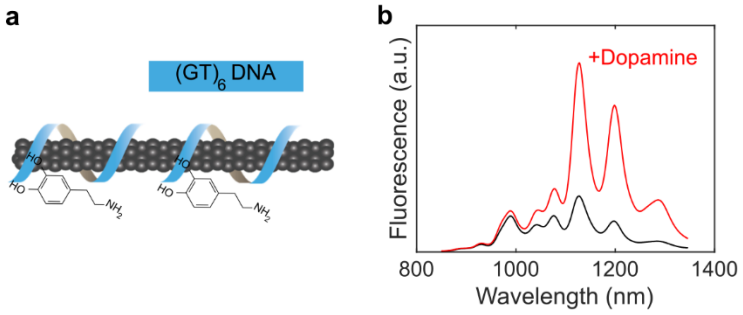

Figure 1.2 Near-infrared fluorescence response of DNA-wrapped SWCNT to dopamine. (a) Schematic of $(GT)_6$-DNA wrapped SWCNT and its interaction with dopamine. **(b)** Fluorescence spectra of $(GT)_6$-SWCNT before (black) and after (red) addition of 100 μM dopamine (721 nm laser excitation).

These $(GT)_6$-SWCNTs show robust, reversible response to dopamine at concentrations greater than approximately 10 nM.[9] Near-infrared microscopy of SWCNT neuro-sensor is demonstrated *in vitro* by surface immobilizing $(GT)_6$-SWCNTs on the glass surface of Ibidi microfluidic slide and imaging using a custom nIR fluorescence microscope with 721 nm laser excitation (**Figure 1.3a**). The channel slide is connected to a syringe pump with alternating flow of phosphate-buffered saline (PBS) and 100 μM dopamine (DA), revealing highly reversible sensor response (**Figure 1.3b**).

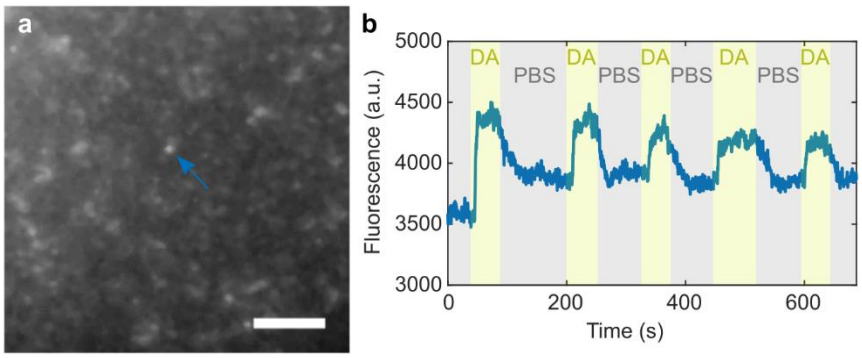

Figure 1.3 Dopamine response of surface immobilized $(GT)_6$-SWCNT. (a) Field of view capture of $(GT)_6$-SWCNTs surface immobilized on an Ibidi glass channel slide with 721 nm laser excitation and 860 nm long pass filter. Scale bar is 5 μm. **(b)** Fluorescence time trace of SWCNT identified by blue arrow in previous panel. Video was collected while alternating flow of PBS and 100 μM dopamine (DA).

This turn-on response can be leveraged for imaging dopamine release and reuptake in mouse brain tissue. Passive incubation of acute coronal mouse brain slices in a bath containing $(GT)_6$-SWCNT sensor leads diffusion to of SWCNT into the brain slice, penetrating greater than 40 μm of tissue after 15 min of incubation (**Figure 1.4**).

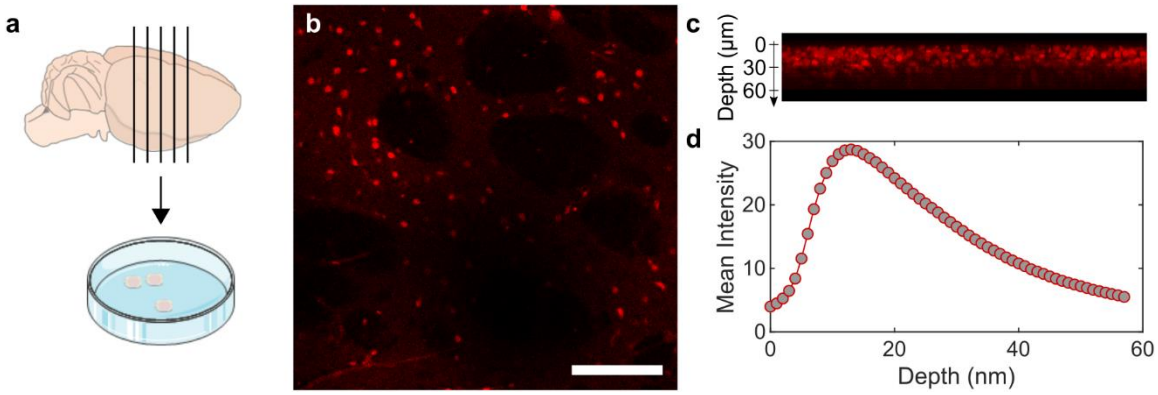

Figure 1.4 Labeling of mouse brain slice with SWCNT neuro-sensor. (a) Schematic of acute coronal brain slice orientation and subsequent incubation in a bath containing $(GT)_6$-SWCNT. Neuro-sensor diffuses into the tissue over a 15 min incubation at room temperature with 95% O_2 perfusion. **(b)** Confocal microscopy image of brain slice labeled with Cy5-$(GT)_6$ wrapped SWCNT at a depth of approximately 12 μm into the tissue. Scale bar is 100 μm. **(c)** Projection of fluorescence confocal image stack about the x axis. **(d)** Mean Cy5 fluorescence per image within the z direction scan.

However, many issues arise when these carbon nanotube neuro-sensors are introduced into brain tissue. While SWCNTs are capable of diffusing across tens of microns throughout the highly tortuous extracellular space, the above experiment revealed that much of the signal measured originated from within cell-like structure (**Figure 1.4b**). This indicates noticeable endocytosis of neuro-sensor by neurons or glial cells, which decreases the concentration of sensor available for neurotransmitter detection in the extracellular space. Furthermore, other cellular mechanisms may be affected by the presence of these nanomaterials. There remains a gap in the literature on how

these nanomaterials affect brain tissue particularly with regards to synaptic signaling, the phenomena this platform seeks to study.

In this work, I explore three aspects of DNA-wrapped carbon nanotube neuro-sensors: (1) the dynamic biomolecular surface composition of SWCNT neuro-sensor in biological environments, (2) the impact of these probe on surrounding brain tissue, and (3) the passivation of unoccupied surface to mitigate the previously established biological impact. The competitive adsorption between DNA on the SWCNT surface and proteins in solution plays a vital role in the molecular recognition ability of these constructs.[22] Furthermore, the composition of adsorbed molecules, known as the nanoparticle corona phase, affects SWCNT sensor photoluminescent response to analyte. Interactions of the SWCNT corona with biological environments also dictates how these nanomaterials affect living tissues.[23] Finally, these provide metrics by which different SWCNT constructs can be qualified in terms of biological response. Each of these facets provides valuable insights into our understanding of carbon nanotubes as emerging platforms for molecular biology applications. Collectively, this work advances SWCNT catecholamine sensors as viable and advantageous tools for neuroscience.

1.3 Dissertation Outline

The contents of this dissertation are presented in the following chapters and appendices:

Chapter 2

Here, I present an assay for real-time, multiplexed tracking of biomolecule adsorption on the carbon nanotube surface. This method utilizes carbon nanotube induced fluorescence quenching to detect binding events of fluorophore-labeled biomolecules to the SWCNT surface. We utilize this approach to track competitive ad-/de-sorption of proteins and DNA on SWCNTs. This approach was used to compare the affinity of the proteins, fibrinogen and albumin to DNA-wrapped SWCNTs. We find that fibrinogen, a protein present in blood plasma but absent in blood serum, has a significantly higher affinity for the SWCNT surface than albumin, the most abundant protein in blood. This result highlights the importance of assessing sensor efficacy in relevant biofluids such as blood plasma over the more widely used blood serum.

Chapter 3

In this chapter, I begin a discussion of how carbon nanotube neuro-sensors affect their surrounding biological environments. Specifically, I show the *in vitro* effects of SWCNTs on microglial cells, the resident immune cells of the brain. I use various techniques in microscopy to show the immediate morphological response of cells to these neuro-sensors and the fate of the neuro-sensors within the cells. Furthermore, these data in conjunction with cell viability assays provide insights into the concentrations and conditions at which SWCNTs become cytotoxic. I also present initial data utilizing a novel proteomic technique to characterize the protein corona of internalized SWCNT neuro-sensor. This provides the groundwork for subcellular localization of SWCNTs via identification of adsorbed proteins.

Chapter 4

Recent developments in high-throughput sequencing have facilitated the study of the biological impact of nanomaterials using cell transcriptomics analysis. This methodology allows for an assessment of the cellular mechanisms triggered by carbon nanotubes. Hence, I use RNA-seq to evaluate the time at which microglial activation by SWCNTs occurs. Subsequently, I compare the transcriptomic response of microglial cells exposed to SWCNT neuro-sensor to that elicited by other commonly used neuro-probes. Differential expression analysis is used to identify mRNA biomarkers for SWCNT exposure which are unique to SWCNTs over more common inflammatory agents. Finally, statistical analysis of differentially expressed genes reveals cell signaling pathways distinctively activated by SWCNTs. These provide clues which may elucidate the exact SWCNT-receptor interactions which mediate the previously established phenotypic changes in microglia.

Chapter 5

By studying the interactions between carbon nanotubes and their biological environments, we gather insights into how to mitigate unfavorable interactions. The relatively bare surface of DNA-wrapped SWCNTs allows for further noncovalent modification using molecules which decrease protein adsorption and subsequent activation of signaling proteins on cell membranes. Herein, I show that PEGylated phospholipids adsorb to bare SWCNT surface with high affinity and mitigate SWCNT induced activation of microglia. Subsequently, these modified sensors

enhance detection of dopamine release and reuptake in acute mouse brain slices, increasing both signal intensity and dispersity of neuro-sensor.

Chapter 6

This chapter summarizes the findings and conclusions of this work. Here, I discuss areas which warrant further investigation in addition to potential future directions for this work.

Appendix A

A growing concern in the field of bionanotechnology is the presence of endotoxin contaminants in nanomaterial stocks. In this appendix, I discuss the biological implications of these contaminants on the work presented herein. Furthermore, I explore proposed methods of endotoxin decontamination in carbon nanomaterials.

Appendix B

Here I present findings from preliminary protein mass spectrometry experiments aimed at characterizing the SWCNT protein corona that develops in a tissue culture. These utilized cell lysate as the model biofluid resulting in identification of over 1,000 unique adsorbed proteins. However, many of these proteins were deemed biologically irrelevant due to the low probability of the SWCNT-protein interaction given the canonical SWCNT endocytosis pathway and the location of the specific protein within the cell. Hence, this data set emphasized the importance of experimental design in obtaining a protein corona list which reflects a cell-internalized SWCNT corona. Nevertheless, this data provides important insights into the fundamental interactions between SWCNTs and proteins and hence warrants further study.

Chapter 2:
Characterization of the Carbon Nanotube Corona

Portions of this chapter are reproduced and adapted with permission from Ref 22. Copyright 2020 American Chemical Society.

2.1 Introduction

Adsorption of polymers on single-walled carbon nanotubes (SWCNTs) has enabled developments in molecular sensing,[24] in vivo imaging,[25] genetic cargo delivery,[26] and chirality sorting.[5] Noncovalent SWCNT functionalization offers a route that preserves the pristine atomic structure, thus retaining the intrinsic near-infrared (nIR) fluorescence of the SWCNTs for the aforementioned applications. However, noncovalent adsorption is an inherently dynamic process, where exchange occurs between molecules in the bulk solution and molecules on the surface, into what is known as the 'corona phase'. In the case of polymers on SWCNTs, the nature, strength, and kinetics of both the polymer binding and unbinding processes are key contributors to the success of polymer-SWCNT based technologies.[27] Understanding this exchange process is especially critical for intended uses of functionalized SWCNTs to probe biological environments. When a nanoparticle is injected into a biological system, the nanoparticle surface is spontaneously and rapidly coated with proteins to form the 'protein corona'.[28] In the case of noncovalent polymer-SWCNT complexes, we hypothesize that native biomolecules compete with the original polymer to occupy the nanoparticle surface. Binding of proteins and other biomolecules to the SWCNT can disrupt the intended functionality of the nanoparticle and lead to potentially adverse biocompatibility outcomes.[29,30] This phenomenon of protein corona formation leads to challenges in translating in vitro sensing or biomolecule delivery platforms to in vivo application. Moreover, the generally accepted method of simulating in vivo biological conditions involves testing nanotechnology performance in blood serum.[25,31] Yet, the absence of blood coagulation proteins from serum could yield a false outcome in assessing robustness of the nanotechnology and accordingly result in unpredicted failure when applied in vivo.

To clarify how nanoparticle-polymer conjugates behave in biologically relevant environments, it is pivotal to understand the kinetics describing molecular exchange on nanoparticle surfaces. Hence, we aim to gain a mechanistic understanding of how SWCNT-based neuromodulator sensors behave in protein-rich milieus. These sensors are based on noncovalent functionalization of $(GT)_6$ single-stranded DNA (ssDNA) on SWCNTs, resulting in a complex that exhibits ultrasensitive $\Delta F/F_0$ = 2400% and 3500% fluorescence turn-on responses in the presence of neuromodulators dopamine and norepinephrine, respectively.[1,9,12,19] However, the drastic enhancement of SWCNT fluorescence experienced upon in vitro exposure to dopamine is attenuated to $\Delta F/F_0 \approx 20\%$ once the sensors are applied in brain tissue,[1] presumably due to protein adsorption and/or disruption of the ssDNA corona phase originally on the SWCNT surface.

Current methods to measure dynamic, noncovalent exchange on nanoparticles exist but are limited in scope. Most research on protein-surface interactions involves characterizing macroscopic surfaces using a series of well-developed techniques that broadly entail an input signal modulated by changing adsorbate mass on the surface as a function of time, including total internal reflection fluorescence microscopy, surface plasmon resonance, biolayer interferometry,

and quartz-crystal microbalance with dissipation monitoring. To apply these surface techniques to nanoparticles, the nanoparticles must be surface-immobilized, thus introducing unrealistic topographical constraints that affect ligand exchange kinetics, lead to mass transport limitations,[32] do not reproduce solution-phase nanosensor responses,[33] and cause nonselective protein adsorption to any surface left exposed during the sparse SWCNT immobilization process.[33]

An alternative method that permits the study of SWCNTs in solution takes advantage of SWCNT sensitivity to their local dielectric environment[34–36] by monitoring SWCNT fluorescence intensity changes and solvatochromic shifts upon corona exchange.[37,38] This technique is applied to study polymer-surfactant exchange kinetics,[4,39–41] whereby SWCNTs suspended with surfactant exhibit higher quantum yield and optical transition energy (i.e. blue-shifted spectra) compared to SWCNTs suspended with most biomolecules such as protein or ssDNA. Previous work has successfully applied measurable differences in SWCNT fluorescence spectra to study relative changes in corona surface composition.[42,43] However, this approach cannot distinguish the exchange of two biomolecules (here, ssDNA to protein), nor can it distinguish between molecular rearrangement vs. molecular desorption from the SWCNT surface. Despite the advantage of undertaking corona exchange studies in the solution phase with this approach, its low sensitivity, non-quantitative nature, and inability to distinguish between adsorbed biomolecules nullifies its potential for monitoring ssDNA-protein exchange.

In this work, we present an assay that overcomes the limitations of previous characterization methods to study corona exchange dynamics between solution-phase and corona-phase biopolymers on SWCNTs, specifically applied to ssDNA and protein. This assay exploits the quenching of fluorophores when in close proximity to the SWCNT surface to monitor ligand binding and unbinding events (**Figure 2.1**).[44]

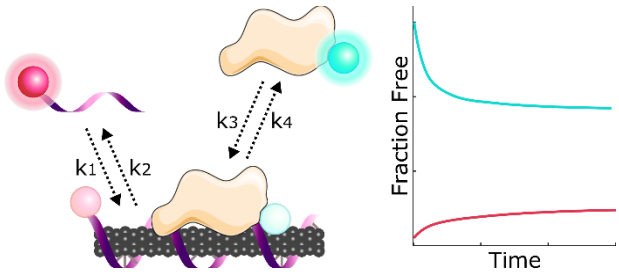

Figure 2.1 Schematic of fluorescence quenching assay for real-time tracking of competitive adsorption to SWCNT surface

While prior literature has similarly harnessed fluorophore quenching by SWCNTs to study the ssDNA-to-SWCNT binding process,[30,37,45] far less is known regarding how pre-adsorbed ssDNA and biologically native proteins exchange on the SWCNTs. To our knowledge, this method is unique in enabling real-time monitoring of SWCNT surface exchange between ssDNA and proteins, tracing the fate of all biomolecules involved in the binding exchange. We conduct multiplexed fluorescence tracking of polymer adsorption and desorption events to/from the SWCNT surface. As a case study for this assay, we focus on comparing the sorption behavior of two specific blood proteins, human serum albumin and fibrinogen, chosen because: (i) both are highly abundant in plasma, with albumin as ~55% (w/v) of blood plasma, or 35-50 mg/mL[46] and fibrinogen as ~4% (w/v) of blood plasma, or 1.5-4.5 mg/mL,[47] (ii) albumin is present in both

blood plasma and serum, whereas fibrinogen is a key coagulation protein present in plasma but depleted from serum, and (iii) albumin and fibrinogen are known to be interfacially active proteins prone to surface-adsorption and are implicated in the formation of many other nanoparticle coronas.[48–50] Binding profiles from the experimental assay in conjunction with a competitive-exchange model are used to extract kinetic parameters for each adsorbent species. Although this study specifically examines competitive adsorption of individual plasma proteins, albumin and fibrinogen, onto $(GT)_6$- and $(GT)_{15}$-SWCNTs, the assay is general to any molecules that can be fluorescently labeled and to any nanomaterial surface to which these species may adsorb and display quenched fluorescence. Binding is also compared to the orthogonal and more ubiquitously used platform monitoring solvatochromic shifting of the nIR SWCNT spectrum as a proxy for SWCNT corona coverage.[42,43] The work presented herein develops an understanding of the fundamental corona exchange mechanism, contextualizes the nature of the ligand exchange process vs. SWCNT solvatochromic shifting, and provides guidance for testing the performance of SWCNT-based systems in biologically relevant, protein-rich conditions.

2.2 Mitigation of Sensor Response by Protein Adsorption

Noncovalent modification of single-walled carbon nanotubes (SWCNTs) with single-stranded $(GT)_6$ DNA imparts nIR fluorescence responsivity to the small molecule neurotransmitter, dopamine.[1,12,19] Addition of 200 μM dopamine to 5 μg/mL solution-phase $(GT)_6$-SWCNTs in phosphate buffered saline (PBS) yields an 11.5-fold increase in nanosensor fluorescence at the 1200 nm SWCNT emission peak (**Figure 2.2a**). Nanosensor response was diminished in the presence of 40 μg/mL human serum albumin (HSA, **Figure 2.2b**) and 40 μg/mL fibrinogen (FBG, **Figure 2.2c**), proteins abundant in intravenous environments. Incubation of 40 μg/mL HSA or FBG with 5 μg/mL (GT)6-SWCNTs reduced fluorescence dopamine response by 52.2% or 78.2% after 40 min (**Figure 2.2d**), respectively. Attenuation of nanosensors was due to two effects: addition of protein led to (i) increase in baseline fluorescence intensity, likely due to protein adsorption which is predicted to be highly favorable by a thermodynamic analysis[22] and (ii) decrease in final fluorescence after addition of dopamine to $(GT)_6$-SWCNTs. HSA did not cause any wavelength shifting of the $(GT)_6$-SWCNT emission, while FBG exposure led to a red shift of 2.6 ± 0.6 nm (mean ± standard deviation of N = 3 sample replicates). Although changes in both the nIR fluorescence intensity and emission wavelength could indicate protein binding, monitoring the SWCNT fluorescence alone does not provide sufficient information to correlate these phenomena.

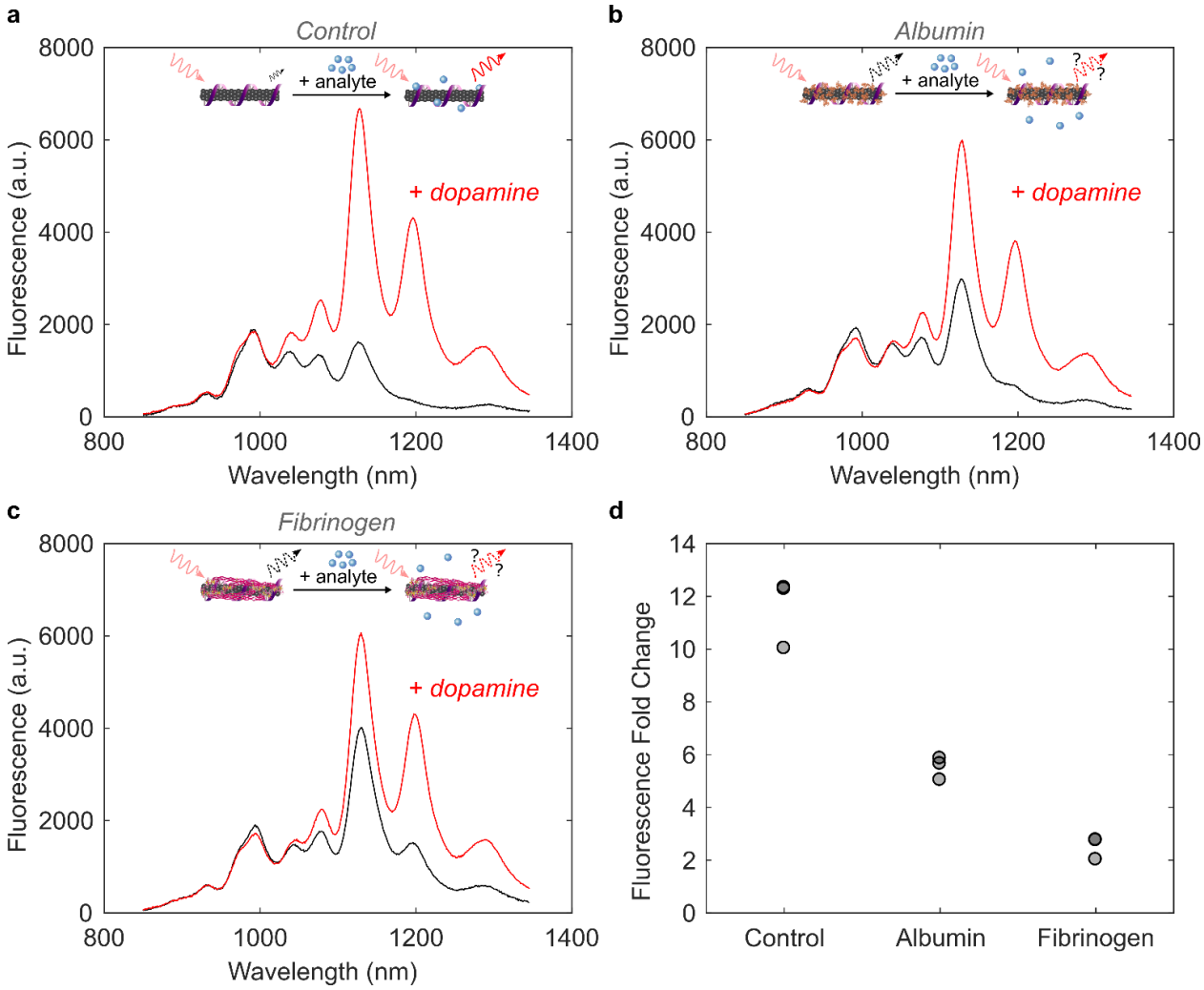

Figure 2.2 Protein adsorption attenuates $(GT)_6$-SWCNT sensor response to dopamine. (a) nIR spectra of 5 µg/mL $(GT)_6$-SWCNTs before (black) and after (red) addition of 200 µM dopamine. **(b–c)** nIR spectra of 5 µg/mL $(GT)_6$-SWCNTs incubated with 40 µg/mL **(b)** albumin or **(c)** fibrinogen for 40 minutes before (black) and after (red) addition of 200 µM dopamine. Insets depict influence of protein corona formation on ability of nanosensor to respond to analyte. **(d)** Change in $(GT)_6$-SWCNT fluorescence intensity at 1200 nm peak following 40 minutes incubation in PBS or protein solution at 40 µg/mL, then addition of 200 µM dopamine (N = 3). Nanosensor excitation was with 721 nm laser.

We first implemented the solvatochromic shift assay to study surfactant-induced fluorescence changes of 5 µg/mL $(GT)_6$-SWCNTs incubated with either 40 µg/mL HSA or FBG for 40 minutes. Displacement of the biopolymer corona phase with surfactant, here 0.5% (w/v) sodium dodecylbenzene sulfonate (SDBS), causes a change in local dielectric environment that in turn leads to a blue shift in SWCNT emission wavelength and an increase in SWCNT fluorescence emission intensity. The magnitude of these observed effects is thought to provide insight on the original SWCNT-corona stability. Interestingly, FBG incubated with $(GT)_6$-SWCNTs resulted in both the largest magnitude wavelength shift and largest fold change in fluorescence intensity upon addition of SDBS (**Figure S2.1**). In contrast, HSA incubated with $(GT)_6$-SWCNTs did not show

a significantly different wavelength shift or intensity fold change compared to the control, $(GT)_6$-SWCNTs incubated with only PBS. These results suggest albumin and fibrinogen proteins may have different binding propensities and kinetics to the SWCNT surface. However, this test fails to decouple the interactions between SWCNTs with ssDNA, protein, and then surfactant. To further study the differential attenuation of sensor response by HSA and FBG, and more thoroughly understand the exchange dynamics occurring on the SWCNT surface, we developed a method for studying SWCNT corona composition by multiplexed fluorescence monitoring.

2.3 Fluorescence Tracking of Biomolecule Adsorption

Our assay leverages fluorophore quenching induced by proximity to the SWCNT surface[44] to measure surface exchange dynamics. Proteins under study were labeled with fluorescein (FAM) fluorophore (ex/em = 494/520 nm) using NHS ester conjugation to primary amine groups (see **2.6 Materials and Methods**). Single-stranded DNA (ssDNA) were procured with a 3' terminally labeled cyanine5 (Cy5) fluorophore (ex/em = 648/668 nm), enabling spectrally resolved multiplexed tracking of protein and ssDNA. The ssDNA-Cy5 is initially quenched on the SWCNT surface, increasing in fluorescence upon desorption from the SWCNT. This methodology has been previously implemented to study thermodynamics of fluorophore-labeled ssDNA interactions on SWCNT surfaces.[51] Conversely, the FAM-labeled protein exhibits high fluorescence when added in bulk solution, quenching upon adsorption to the SWCNT surface. In this manner, FAM-labeled protein can be injected into ssDNA-Cy5-SWCNTs in a well-plate format and fluorescence changes resulting from biomolecule exchange can be read by a fluorescence plate reader (**Figure 2.3a**). We first employed this method to compare the desorption rates of $(GT)_6$-Cy5 and $(GT)_{15}$-Cy5 from SWCNTs upon addition of FAM-labeled HSA and FBG. Both proteins promoted dequenching of Cy5, as compared to the addition of PBS control (**Figure 2.3b–c**). Dequenching was due to complete desorption of ssDNA rather than partial desorption of the 3' end, as verified by confirming that the binding profiles of 3'- vs. internally Cy5-labeled ssDNA are similar (**Figure S2.2**). Additionally, presence of the Cy5 tag on ssDNA did not significantly affect protein adsorption (**Figure S2.3**). Fibrinogen generated a 3.09 ± 0.07 Cy5 fluorescence fold increase for $(GT)_6$-Cy5-SWCNTs vs. a 1.52 ± 0.04 Cy5 fluorescence fold increase for $(GT)_{15}$-Cy5-SWCNTs. This result suggests (GT)15 is less readily displaced from the SWCNT surface compared to the shorter (GT)6 construct, a result consistent with the literature.[52–54]

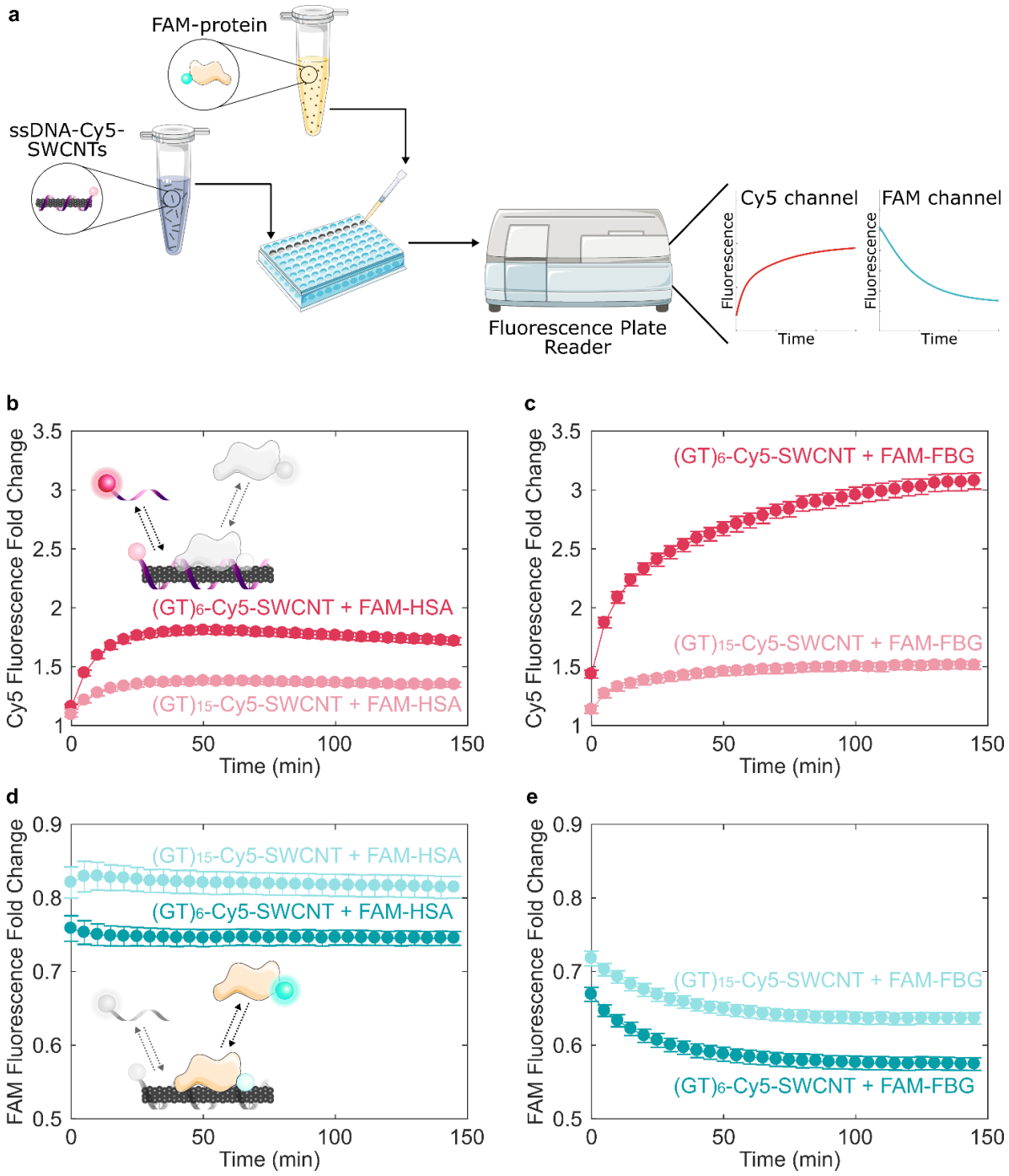

Figure 2.3 Tracking exchange of fluorophore-labeled ssDNA and protein on SWCNT surfaces demonstrates protein adsorption selectivity and ssDNA length effect. (a) Corona exchange assay workflow. ssDNA-Cy5-SWCNT solution is added to a well-plate, FAM-protein solution is injected, and the ad-/de-sorption processes are monitored in separate color channels of a fluorescence plate reader (**2.6 Materials and Methods**). Increase in ssDNA-Cy5 fluorescence induced by addition of 40 μg/mL **(b)** FAM-labeled albumin (FAM-HSA) or **(c)** FAM-labeled fibrinogen (FAM-FBG) to 5 μg/mL ssDNA-Cy5-SWCNT suspended with ssDNA, $(GT)_6$ or $(GT)_{15}$. Decrease in fluorescence of **(d)** FAM-HSA and **(e)** FAM-FBG after addition of protein to $(GT)_6$- or $(GT)_{15}$-SWCNT. Error bars represent standard error between experimental replicates (N = 3).

In the same experiment, protein adsorption onto ssDNA-Cy5-SWCNTs was concurrently tracked via fluorescence quenching of the protein-conjugated FAM. Presence of residual FAM fluorophore in the FAM-protein solution was accounted for by quantifying free FAM and subtracting the minimal change in fluorescence due to free FAM-to-SWCNT interaction (**Figure S2.4**, **Figure S2.5**, **Table S2.1**). Furthermore, the effect of FAM fluorophore labeling on the protein-exchange dynamics was minimal (**Figure S2.6**), in agreement with previous investigations demonstrating that fluorescein-labeling of proteins does not perturb protein adsorption or function, and additionally that fluorescein signals are proportional to the interfacial mass of the tagged species.[55–58] By tracking the fluorescence modulation resulting from FAM-protein interactions with ssDNA-Cy5-SWCNTs, we found that FAM-FBG exhibited a comparatively larger degree of quenching than FAM-HSA for both ssDNA-SWCNT suspensions (**Figure 2.3d–e**): upon addition of 40 μg/mL FAM-FBG to 5 μg/mL (GT)6-SWCNTs (final concentrations), FBG induced a 42.5 ± 0.9% decrease in FAM fluorescence vs. a 25.5 ± 0.9% HSA-induced decrease in FAM fluorescence. These results consistently suggest two interaction mechanisms of ssDNA and protein with SWCNTs: (i) $(GT)_{15}$ ssDNA binds to SWCNTs with a higher affinity than $(GT)_6$ ssDNA, thus reducing protein adsorption, and (ii) FBG interacts with ssDNA-SWCNTs more strongly than HSA. The former result agrees with prior work confirming that the rate of ssDNA desorption from SWCNTs decreases with increasing oligo length,34 also valid in the presence of competing biomolecules.[8] As such, our data suggest that FBG protein adsorption leads to more significant ssDNA desorption from SWCNTs, whereas HSA adsorbs less strongly and accordingly causes less ssDNA desorption from SWCNTs. These ssDNA-protein corona exchange trends were corroborated with polyacrylamide gel electrophoresis (PAGE) of the unbound species, where FAM-FBG adsorbed to $(GT)_6$-Cy5-SWCNTs 56.5% more than FAM-HSA and caused 5.20% greater desorption of ssDNA (**Figure S2.7**). From our corona exchange assay, it is interesting to note that protein adsorption occurs faster than ssDNA desorption. These experimental results motivate kinetic modeling of ssDNA and protein exchange on SWCNT surfaces.

2.4 Modeling Competitive Adsorption on SWCNT Surface

To quantitatively probe differences in protein affinities for ssDNA-SWCNTs, we fit Cy5 and FAM fluorescence data to a competitive adsorption model and extracted kinetic parameters for ssDNA and proteins. Multiplexed fluorescence tracking was repeated with 5 μg/mL $(GT)_6$-Cy5-SWCNTs and concentrations of FAM-HSA and FAM-FBG ranging from 5 to 160 μg/mL. Fluorescence values were converted to mass concentration using standard curves for ssDNA-Cy5 and both FAM-conjugated proteins (**Figure S2.8**). A model was developed for the competitive exchange between ssDNA and protein on the SWCNT surface (Equations 2.1 and 2.2). In the model, unbound ssDNA (D) and protein (P) adsorb and desorb reversibly to SWCNT surface sites (*):

$$D + * \underset{k_2}{\overset{k_1}{\rightleftarrows}} D * \qquad \text{(Eq. 2.1)}$$

$$P + * \underset{k_4}{\overset{k_3}{\rightleftarrows}} P * \qquad \text{(Eq. 2.2)}$$

Total concentration of SWCNT surface sites ($[*]_T$) was fixed, given by a site balance (Equation 2.3), where *, D*, and P* refer to vacant sites, sites occupied by bound ssDNA, and sites occupied by bound protein, respectively:

$$[*]_T = [*] + [D*] + [P*] \quad \text{(Eq. 2.3)}$$

Bound ssDNA and bound protein concentrations were calculated by species conservation, where total ssDNA was the amount added during ssDNA-SWCNT synthesis, total protein was the injected protein quantity, and total sites ($[*]_T$) was a fit parameter. Rate constants k_1, k_2 for ssDNA binding/unbinding, k_3, k_4 for protein binding/unbinding, and the total concentration of binding sites $[*]_T$ were computed using a least squares curve fit of Equations S2.1 and S2.2 to experimental data (see **2.6 Materials and Methods**).

Experimental data of FAM-HSA or FAM-FBG added to $(GT)_6$-Cy5-SWCNTs was fit to this model for each concentration tested (**Figure 2.4**). All mean relative errors comparing fits to experimental data were < 5% (**Table S2.2**). The model recapitulates the experimental observation that FBG has a higher affinity for SWCNTs (**Figure 2.4d**) than HSA (**Figure 2.4b**), where average k_3, FBG = 1.43 x 10^{-5} > k_3, HSA = 8.88 x 10^{-6} mL μg^{-1} s^{-1} (**Table 2.1**, with full fit parameter results in **Table S2.2**). These k values are in relative agreement with previous literature assessing the kinetic parameters for ssDNA desorption from SWCNTs,[59] and protein binding to nanoparticles.[60] At the same initial FAM-protein concentration of 40 μg/mL added to 5 μg/mL $(GT)_6$-Cy5-SWCNTs, FBG adsorbed to a higher fraction of bound protein (0.756) than HSA (0.284) after 1 hour. Final solution-phase concentrations of FAM-FBG and FAM-HSA were 9.04 and 28.5 μg/mL, respectively, compared to concentrations of 13.8 and 36.4 μg/mL determined by PAGE (**Figure S2.7d**). Solution-phase concentrations of $(GT)_6$-Cy5 upon addition of FAM-FBG and FAM-HSA increased from 0.106 to 0.301 μg/mL and from 0.101 to 0.128 μg/mL, respectively, compared to concentration changes of 0.331 to 0.388 μg/mL and 0.688 to 0.767 μg/mL determined by PAGE (**Figure S2.7c**). The discrepancy in concentrations across the two approaches may be due to technical differences between methods, where gel electrophoresis is limited in both sensitivity and temporal resolution.

Addition of FAM-FBG into solution with $(GT)_6$-Cy5-SWCNTs led to ssDNA desorption for all tested concentrations of injected FAM-FBG (**Figure 2.4c**), as compared to only ≥ 40 μg/mL of injected FAM-HSA led to measurable ssDNA desorption (**Figure 2.4a**). Adsorption of ssDNA was observed upon addition of PBS or low concentrations of FAM-HSA (≤ 20 μg/mL) to (GT)6-Cy5-SWCNTs, indicating an initial excess of unbound ssDNA in bulk solution. Interestingly, the intermediate concentration of FAM-HSA (40 μg/mL) added to (GT)6-Cy5-SWCNTs resulted in sigmoidal ssDNA desorption behavior that is not fully described by the model. This behavior fundamentally implies that the assumption of independent reactions made in Equations 1 and 2 may not hold for intermediate concentrations of FAM-HSA. Specifically, the dependence of ssDNA dissociation constant k_2 on total protein concentration indicates that the rate of ssDNA desorption is a function of adsorbed or free protein concentration (**Table S2.2**, **Figure S2.9**). This higher-order desorption process may account for the discrepancy between experimental data and model fit for (GT)6-Cy5 desorption induced by addition of 40 μg/mL FAM-HSA.

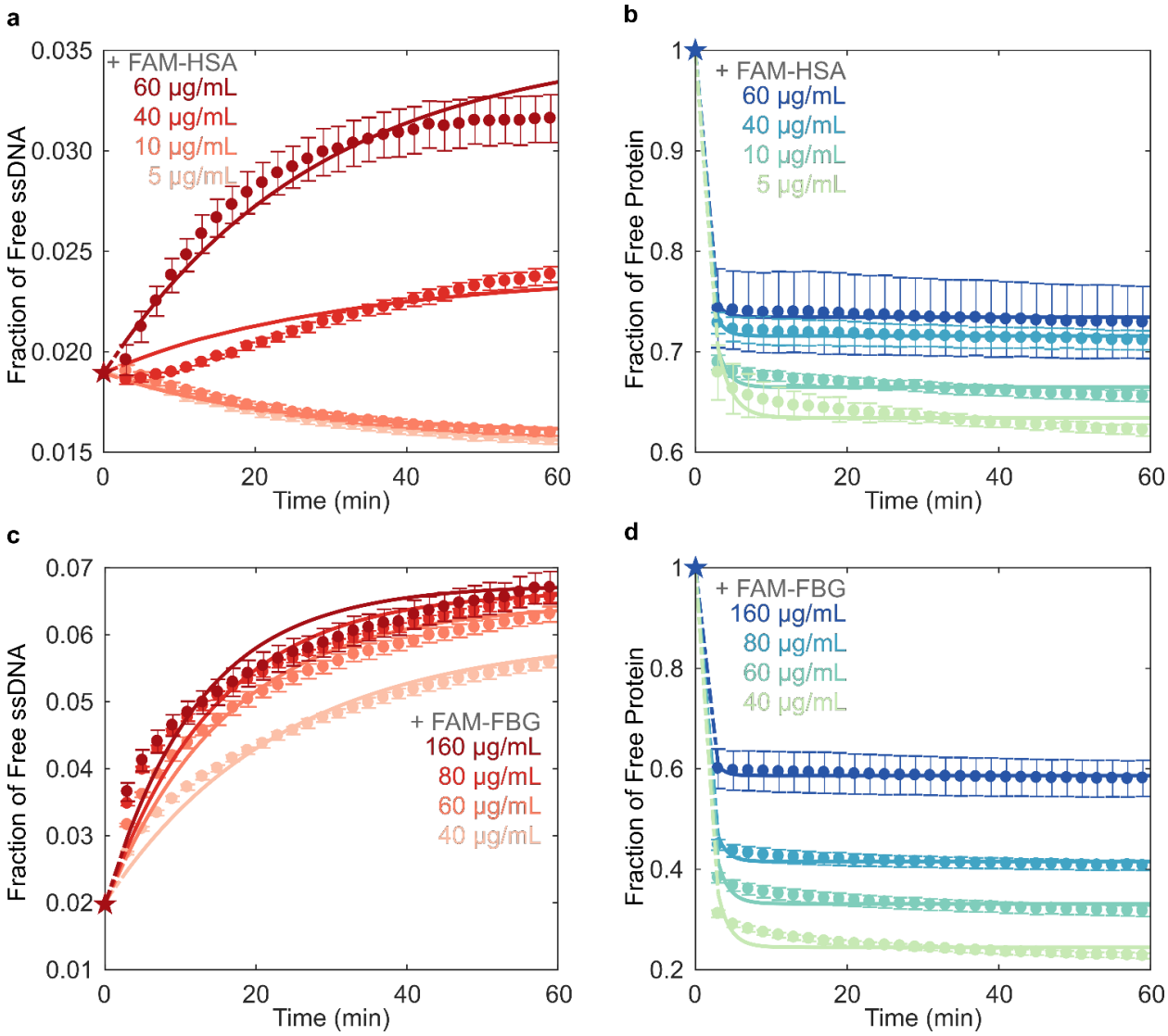

Figure 2.4 Kinetic model of competitive exchange between ssDNA and protein on SWCNTs fit to fluorescence data to extract rate constants. (a–b) Fraction of **(a)** $(GT)_6$-Cy5 ssDNA and **(b)** FAM-labeled albumin (FAM-HSA) protein free in solution for varying concentrations of FAM-HSA injected into 5 µg/mL $(GT)_6$-Cy5-SWCNT solution. **(c–d)** Fraction of **(c)** $(GT)_6$-Cy5 ssDNA and **(d)** FAM-labeled fibrinogen (FAM-FBG) protein free in solution for varying concentrations of FAM-FBG injected into $(GT)_6$-Cy5-SWCNT solution. Star data points represent initial conditions used for solving model differential equations. Error bars represent standard error between experimental replicates (N = 3).

Table 2.1 Range of kinetic model fit parameters.

Protein	$k_1 \times 10^6$ (mL µg^{-1} s^{-1})	$k_2 \times 10^6$ (s^{-1})	$k_3 \times 10^6$ (mL µg^{-1} s^{-1})	$k_4 \times 10^6$ (s^{-1})	$[*]_T$ (µg mL^{-1})
Albumin	1.10 - 1.54	8.40 - 20.7	7.86 - 9.44	5,850 - 12,000	365 - 526
Fibrinogen	1.15 - 2.30	42.7 - 90.9	11.8 - 16.9	2,610 - 9,150	486 - 620

For all concentrations tested, protein adsorption proceeded significantly faster than ssDNA desorption dynamics, indicating that protein adsorption precedes ssDNA desorption and suggesting that the two phenomena may be decoupled in time. This difference in exchange time-scales may be due to the large concentration of total SWCNT surface binding sites (with average fit values of $[*]_{T,FBG}$ = 572 μg mL^{-1} and $[*]_{T,HSA}$ = 472 μg mL^{-1}) relative to the total ssDNA and protein concentrations. We hypothesize a low initial ssDNA surface coverage, or large accessible SWCNT surface area, is a likely reason for the difference in exchange timescales. Furthermore, in the case of FAM-FBG with $(GT)_6$-Cy5-SWCNTs, while amount of adsorbed FBG reaches an apparent steady-state value within ~5 minutes (**Figure 2.4d**), ssDNA continues to gradually desorb over time at a rate seemingly independent of injected protein concentration (**Figure 2.4c**). Continued ssDNA desorption may be caused by a surface rearrangement process in the adsorbed FBG layer,[61] where protein spreading could be responsible for this observed ssDNA displacement over longer timescales.[32,56] Hydrophobic interactions are posited to be the driving force for protein spreading on the SWCNT surface[57] and consequently interfacial denaturation is presumed to be the dominant relaxation process, in addition to a smaller contribution from molecular reorientations.[55]

From the kinetic model fitting, the mass of protein adsorbed on the SWCNTs was consistently higher for FBG as compared to HSA for the same initial concentration of 40 μg/mL FAM-protein with 5 μg/mL $(GT)_6$-Cy5-SWCNTs. Previous studies of differential protein adsorption to hydrophobic surfaces has demonstrated that fibrinogen forms well-packed layers, whereas more weakly adsorbed albumin forms less tightly packed, more mobile adsorption layers.[57] Accordingly, we hypothesize that the seemingly higher protein surface coverage on the SWCNT points to the more tightly packed, if not multilayer formation, of FBG on the SWCNT surface.

Some potential shortcomings of our methodology include that the proposed elementary steps only approximate the true exchange mechanism, or that there are nonidealities present in the protein and/or ssDNA sorption behavior. Two alternative models to account for protein binding to surface-adsorbed ssDNA or protein were also attempted, but not pursued due to the poor quality of the fits (**2.6 Materials and Methods**). Constraining the total surface sites $[*]_T$ during model fitting was also pursued, whereby $[*]_T$ would presumably be constant across different concentrations of protein added. Although the model fits to the experimental data are reasonable (**Table S2.3, Figure S2.10**), we decided to fit the data with varying $[*]_T$ to capture the effect of concentration-dependent nonidealities in the system, such as nanotube-nanotube interactions, on all fit parameters. Finally, we note that the system is not truly equilibrated, therefore, a thermodynamic analysis was not pursued.[62]

2.5 Conclusions

Protein adsorption to nanoparticle surfaces is a major hindrance to the successful application of nanotechnologies in vivo. We have shown that incubation of two high-abundance blood plasma proteins, human serum albumin and fibrinogen, with ssDNA-SWCNT dopamine sensors causes significantly different degrees of sensor response attenuation. Developing an understanding of protein-sensor interactions is vital in circumventing this issue and establishing better practices for testing nanotechnologies for in vivo use. Previously established techniques to

evaluate these effects implement surface-immobilized nanoparticles or exploit the intrinsic nIR fluorescence changes of SWCNTs. Yet, these methods do not track the fate of adsorbates and cannot quantify the fraction of free biomolecules in real-time, thus precluding quantitative and temporally resolved studies of the SWCNT protein corona composition. Though the SDBS-induced solvatochromic shift assay successfully identifies FBG as a protein of interest, this assay provides no mechanistic information on FBG binding, nor can it distinguish between HSA and PBS control responses.

We have addressed these limitations in developing a method to quantitatively probe the kinetics of SWCNT corona exchange between ssDNA and protein adsorbates by monitoring fluorescence quenching of conjugated fluorophores in close proximity to SWCNT surfaces. Concentration curves were fit to a competitive adsorption model to extract kinetic parameters. Our method reveals that reduction of dopamine sensor performance correlates with quantity of adsorbed protein, where fibrinogen adsorbs to ssDNA-SWCNTs 168% more than albumin at the same concentration, and consequently leads to 26% more sensor attenuation. We demonstrate significantly greater SWCNT binding affinities for longer repeating ssDNA sequences, and for fibrinogen over albumin. These results bear significance in that albumin is the highest abundance blood protein and is therefore commonly regarded as an important component of the SWCNT corona. However, our results show that lower abundance proteins with higher SWCNT affinities may disproportionately contribute to the SWCNT corona, as has been previously suggested in orthogonal protein corona-nanoparticle studies.[63,64] Preliminary findings from blood plasma and serum samples normalized to 40 μg/mL total protein concentration show that plasma and serum both caused significant attenuation of dopamine response in $(GT)_6$-Cy5-SWCNTs, with 81.0 ± 0.9% and 80.7 ± 1.4% reduction in response, respectively (**Figure S2.11a**). However, plasma—which contains fibrinogen—caused a higher degree of ssDNA desorption, with plasma inducing a 1.64 ± 0.01 fold increase in $(GT)_6$-Cy5 fluorescence vs. a 1.39 ± 0.03 fold increase by serum (**Figure S2.11b**). Our results motivate the necessity to test SWCNT-based and other nanobiotechnologies in more representative bioenvironments, i.e. blood plasma rather than serum.

The method presented herein enables the study of corona formation dynamics of multiple biomolecular entities, with standard laboratory equipment, under varying solution conditions (e.g. ionic strength and pH). The generalizability of this assay allows for study of diverse corona exchange phenomena occurring on the surface of carbon nanotubes between a variety of biomolecular species. We demonstrate that RNA, phospholipids, and peptoids—molecules commonly used in SWCNT-mediated delivery, imaging, and sensing[11,26,65,66] —all exhibit varying degrees of corona exchange with ssDNA-SWCNTs (**Figure 2.5**). Furthermore, we can examine the competitive adsorption of multiple fluorophore-conjugated proteins, such as FAM-HSA and Cy5-FBG onto ssDNA-SWCNTs, where increasing mass ratios of FBG to HSA results in reduced adsorption of the latter (**Figure S2.12**). Careful selection of fluorophores may enable further multiplexing, allowing tracking of more than two distinct molecular species simultaneously. Rationally designed labeling methodologies such as FRET may also enable the study of more complex interactions such as protein denaturation on the SWCNT surface. Implementation of this assay will facilitate more thorough deconvolution of factors driving protein corona formation and accordingly inform design principles for nanotechnologies resistant to protein corona-based biofouling and performance attenuation. In summary, the corona exchange assay we have developed will serve to enhance our still deficient understanding of how noncovalently bound polymers exchange on nanoparticle surfaces and, accordingly, enable the design and testing of nanobiotechnologies towards effective implementation in vivo. In later chapters, this assay is

applied to quantify the degree of nonspecific protein adsorption to different SWCNT constructs as a comparative measure of biocompatibility.

One additional takeaway from the kinetic competitive adsorption model is the relatively sparse occupation of surface sites by DNA molecules. At the initial time point, the fraction of ssDNA bound to the surface is high (θ_D = 0.98). This equates to a concentration of 1.19 μM of ssDNA in the 5 μg/mL SWCNT suspension, or approximately 512 ssDNA molecules per carbon nanotube given an average SWCNT length of 500 nm and molecular weight of 2,177,000 g mol^{-1}. This value can be compared to that calculated by quantifying total adsorbed DNA through surfactant induced desorption. This method results in an estimated 364 $(GT)_6$ ssDNA molecules per SWCNT (see **2.6 Materials and Methods**). These values are consistent with the literature which reports an 850 $(GT)_5$ to SWCNT ratio and 420 for $(GT)_{10}$.[67] Molecular dynamics simulations report a $(GT)_6$ DNA contact area of 2800 $Å^2$ per molecule.[12] Subsequently, the total $(GT)_6$ DNA contact area is between 6.5 – 9.1% of the SWCNT surface. In the literature, values of DNA surface coverage are estimated to be between 20% and 25%.[42,68] This discrepancy may arise from differences in the DNA-SWCNT suspension protocols (e.g. sonication time and power, DNA to SWCNT ratio, salt concentration, etc.) and differences in the techniques used to quantify adsorbed DNA. Whereas other methods utilized surfactant adsorption and subsequent density gradient centrifugation, our approach directly measures adsorbed DNA. Nevertheless, these results commonly suggest that there remains bare carbon lattice on $(GT)_6$ ssDNA wrapped carbon nanotube suspensions. Chapters 3 and 4 of this dissertation will examine the negative biological impact caused by this exposed surface on immune cells of the central nervous system. In Chapter 5, I explore the passivation of unoccupied SWCNT surface area using phospholipids to mitigate both protein adsorption and prevent negative biological effects induced by exposed graphene carbon lattice.

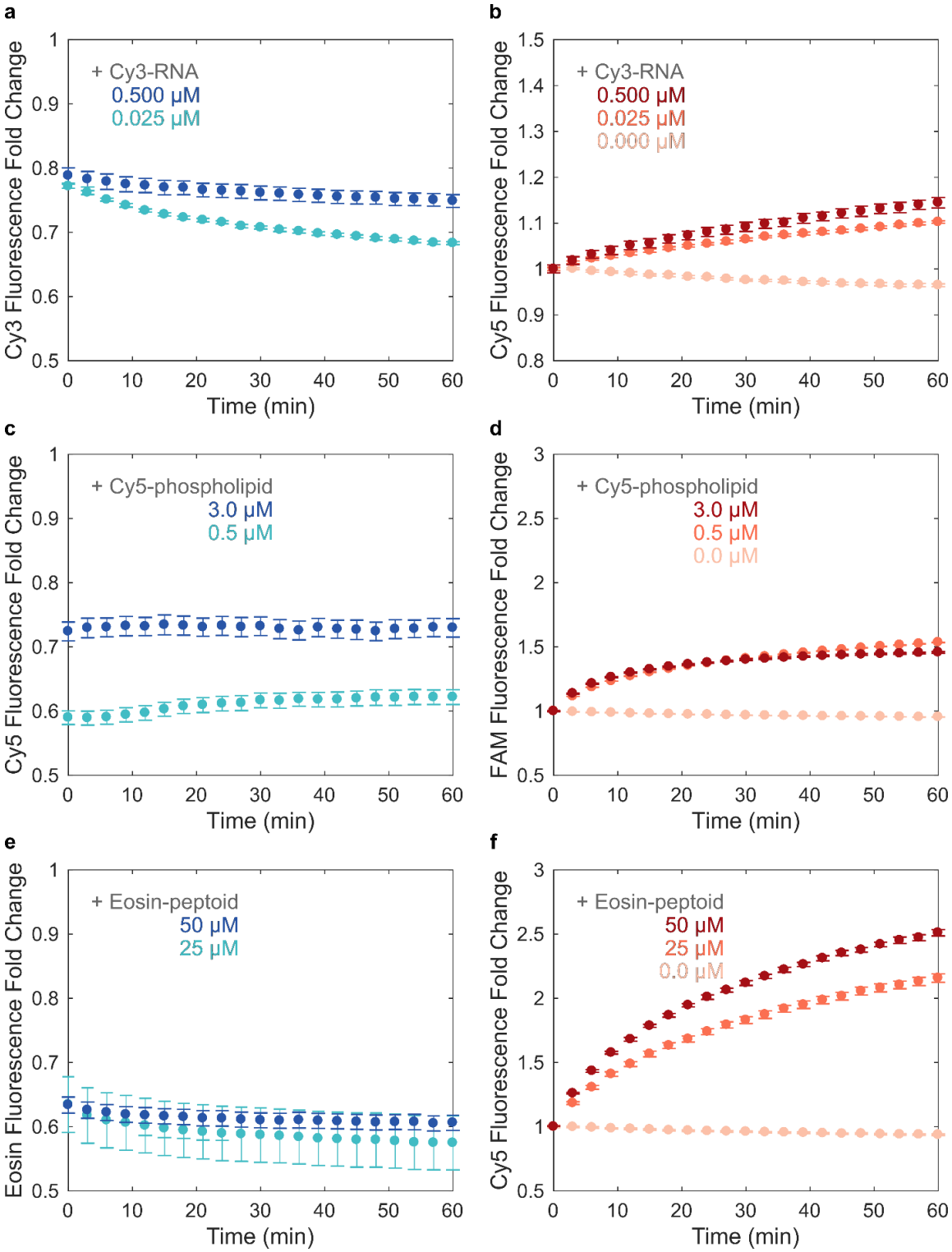

Figure 2.5. Adsorption of various fluorophore-tagged biomolecular species to ssDNA-SWCNTs. Adsorption of varying concentrations of biomolecules to 5 μg/mL $(GT)_6$-SWCNTs. (Column 1) Quenching of fluorophore-tagged biomolecules adsorbing to $(GT)_6$-SWCNTs: **(a)** Cy3-RNA, **(c)** Cy5-phospholipid (DSPE-PEG(2000)-N-Cy5), and **(e)** eosin-peptoid ($(Nae–Npe)_9$-$(Nce–Npe)_9$). (Column 2) Corresponding dequenching of fluorophore-tagged $(GT)_6$ ssDNA desorbing from SWCNT surface: **(b)** $(GT)_6$-Cy5, **(d)** $(GT)_6$-FAM, and **(f)** $(GT)_6$-Cy5. Error bars represent standard error between experimental replicates (N = 3).

2.6 Materials and Methods

Preparation of ssDNA-SWCNT complexes

Single-stranded DNA with single-walled carbon nanotube (ssDNA-SWCNT) suspensions were prepared by combining 0.2 mg of mixed-chirality SWCNTs (small diameter HiPco™ SWCNTs, NanoIntegris) and 20 μM of ssDNA (custom ssDNA oligos with standard desalting, Integrated DNA Technologies, Inc.) in 1 mL of 0.01 M phosphate-buffered saline (PBS). Solutions were probe-tip sonicated for 10 minutes in an ice bath (3 mm probe tip set at 50% amplitude, 5-6 W, Cole-Parmer Ultrasonic Processor). Samples were centrifuged to pellet insoluble SWCNT bundles and contaminants (16,100 cfg for 30 minutes). Supernatant containing the product was collected. ssDNA-SWCNT solutions were stored at 4°C until use. ssDNA-SWCNT concentration was determined via sample absorbance at 910 nm and the corresponding extinction coefficient ε_{910nm} = 0.02554 mL μg^{-1} cm^{-1}.[69] ssDNA-SWCNTs were diluted to a working concentration of 10 μg/mL in 0.1 M PBS.

Cyanine 5 (Cy5) was chosen as the ssDNA fluorophore label, with excitation maximum at 648 nm and emission maximum at 668 nm. The same suspension protocol was employed for preparation of fluorophore-labeled ssDNA-SWCNT complexes, using ssDNA-Cy5 (3' or internally labeled Cy5-labeled custom ssDNA oligos with HPLC purification, Integrated DNA Technologies, Inc.) in place of unlabeled ssDNA. Internally labeled ssDNA-Cy5 includes Cy5 conjugated to the thymine at nucleotide position 6 (GTGTGT/iCy5/GTGTGT).

Total ssDNA adsorbed to SWCNTs was determined by a heat/surfactant elution process. This molar ratio of ssDNA:SWCNT was required to calculate the fraction of free vs. bound ssDNA throughout the exchange process. Optimized elution conditions were achieved with salt and surfactant in the combination of 0.1 M PBS/0.1% (m/v) sodium dodecylbenzene sulfonate (SDBS), in agreement with prior literature demonstrating that SDBS disperses SWCNTs most effectively[37,70] and without chirality bias.[71] Freshly prepared ssDNA-Cy5-SWCNTs were diluted to a final concentration of 5 μg/mL in elution buffer, with a final volume of 150 μL in a PCR tube. Samples were heated at 95°C for 1 hour in a PCR thermocycler, transferred to a clean test tube, and centrifuged (16,100 cfg for 30 minutes) to pellet insoluble SWCNT bundles. 120 μL of supernatant containing the eluted ssDNA-Cy5 was collected. Fluorescence in the Cy5 channel was measured (see **Visible fluorescence measurements** methods section) and compared to a standard curve of known ssDNA-Cy5 concentrations (ranging 0.01 - 1 μM) to correlate the Cy5 fluorescence measurement to ssDNA eluted concentration. This resulted in a mole ratio of 364 ± 2 $(GT)_6$:SWCNT and 140 ± 7 $(GT)_{15}$:SWCNT (both N = 8), in relative agreement with previous literature for (6,5) single chirality SWCNTs.[67]

Fluorophore-labeling of proteins

N-Hydroxysuccinimide (NHS) ester chemistry was used to label proteins via conjugation to primary amine groups. Fluorescein (FAM) was chosen as the protein fluorophore label, with excitation maximum at 494 nm and emission maximum at 520 nm (FAM NHS ester 6-isomer, Lumiprobe). Lyophilized proteins were purchased: human serum albumin (HSA; from human plasma, ≤0.02% Fatty acids, Lot #SLBZ2785, Millipore Sigma) and fibrinogen (FBG; from human plasma, 20 mM sodium citrate-HCl pH 7.4, Lot #3169957, Millipore Sigma). FAM-proteins were prepared with 10 mg of protein reconstituted in 900 μL of 0.1 M sodium bicarbonate (pH 8.5) and 8-fold molar excess of FAM NHS ester solubilized in 100 μL DMSO. Solutions were combined, covered in foil, and incubated on a test tube rotator for 4 hours. FAM-protein conjugates were

twice purified to remove free FAM (Zeba™ 2 mL spin desalting columns with 40 kDa MWCO, Thermo Fisher Scientific) by washing with 0.1 M PBS three times (1,000 cfg for 2 minutes), centrifuging with sample (1,000 cfg for 3 minutes), and retaining sample in flow-through solution (repeating all steps twice with a new spin column). Protein concentration and degree of labeling (DOL) were determined by measuring the absorbance of the FAM-protein conjugate at the protein absorbance maximum, 280 nm (A_{280}), and the fluorophore emission maximum, 494 nm (A_{494}). Protein absorbance was corrected for the contribution of the fluorophore to A_{280} by subtracting A_{494} weighted by the correction factor (CF), an empirical constant of 0.17 for free FAM (from manufacturer). Protein and FAM concentrations were determined by the Beer-Lambert Law using either A_{280} for protein or A_{494} for FAM, with the corresponding extinction coefficients of $\varepsilon_{280nm,HSA}$ = 43,824 M^{-1} cm^{-1},[72] ε_{280nm}, FBG = 513,400 M^{-1} cm^{-1},[73] and $\varepsilon_{494nm,FAM}$ = 75,000 M^{-1} cm^{-1} (from manufacturer). DOL was then calculated as the ratio of FAM to protein molar concentrations, yielding $DOL_{FAM-HSA}$ = 2.773 and $DOL_{FAM-FBG}$ = 0.608.

Free FAM NHS ester remaining after purification was quantified by polyacrylamide gel electrophoresis (PAGE) run according to the Laemmli protocol[74] (adapted in Bio-Rad Mini-PROTEAN Tetra Cell manual). Briefly, purified FAM-protein conjugates were added to sodium dodecyl sulfate (SDS) reducing buffer (2% SDS, 5% β-mercaptoethanol, 0.066 M Tris-HCl) in a 1:2 ratio of sample to buffer. Samples were diluted such that 100 ng of FAM-HSA, 100 ng of FAM NHS ester, or 30 ng of FAM-FBG (due to lower labeling reaction yield) per 20 μL volume was applied per well. PAGE separation was carried out in 1 mm vertical mini gel format (Bio-Rad Mini-PROTEAN Tetra Cell) with a discontinuous buffer system under denaturing conditions. Gel composition was 12% acrylamide (total monomer), 0.375 M Tris-HCl, 0.1% SDS, 0.05% APS, 0.05% TEMED for the resolving gel and 12% acrylamide (total monomer), 0.125 M Tris-HCl, 0.1% SDS, 0.05% APS, 0.1% TEMED for the stacking gel. Electrode buffer was 25 mM Tris, 192 mM glycine, and 3.5 mM SDS (pH 8.3). Separation was run with 200 V for 35 minutes, gels were extracted, and the FAM label was visualized with a gel imager (Typhoon FLA 9500, 473 nm laser, General Electric) (**Figure S2.4**). The FAM-protein conjugate is the higher band (approximately 66 kDa for FAM-HSA, 52-95 kDa for FAM-FBG) and the free, lighter molecular weight FAM NHS ester is the lower band (approximately 0.475 kDa). FAM fluorescence intensity was quantified with ImageJ (**Table S2.1**).

Visible fluorescence measurements

Equal volumes of $(GT)_6$-Cy5-SWCNT and FAM-tagged protein at 2X working concentration were added to a 96-well PCR plate (Bio-Rad) to a total volume of 50 μL. The plate was sealed using an optically transparent adhesive seal (Bio-Rad) and briefly spun down on a benchtop centrifuge. Fluorescence time series readings were taken using a Bio-Rad CFX96 Real Time qPCR System, scanning all manufacturer set color channels (FAM, HEX, Texas Red, Cy5, Quasar 705) every 30 s at 22.5 °C (lid heating off). Fluorescence time series were analyzed without default background correction. Note that concentration ranges of FAM-HSA (5-60 μg/mL) and FAM-FBG (40-160 μg/mL) were chosen to be in the linear fluorescence regime of the qPCR.

Near-infrared fluorescence measurements

Fluorescence spectra were collected with an inverted Zeiss microscope (20x objective, Axio Observer.D1) containing a custom filter cube set (800 nm SP FESH0800, 900 nm LP dichroic DMLP900R, 900 nm LP FELH900, ThorLabs) coupled to a Princeton Instruments spectrometer (SCT 320) and liquid nitrogen cooled Princeton Instruments InGaAs detector (PyLoN-IR

1024/1.7). Fluorescence measurements were done with a beam-expanded 721 nm laser (10-500 mW, OptoEngine LLC) excitation light source and 800 - 1400 nm emission wavelength range. Solution-phase measurements were acquired in a 384 well-plate format (1 s exposure time, 1 mW laser power). Protein solutions (final concentration 40 µg/mL) or PBS control were incubated with (GT)6-SWCNTs (final concentration 5 µg/mL in 0.1 M PBS). For each time point, an aliquot of these incubation solutions was added to a well (40 µL total volume) and an initial fluorescence spectrum was acquired. 10 µL of dopamine was added to a final concentration of 200 µM prior to the second fluorescence acquisition. Fluorescence fold change was measured by taking the ratio of fluorescence intensities at 1200 nm between post- and pre-addition of dopamine spectra.

Similarly, surfactant-induced solvatochromism was performed by collecting nIR fluorescence spectra pre- and 1-minute post-addition of 0.5% (w/v) SDBS. Fluorescence fold change was defined as the ratio of integrated fluorescence intensity (800 to 1400 nm) between post- and pre-addition of SDBS. Wavelength shift was measured relative to the wavelength of the (7,6) SWCNT chirality peak emission (initially 1130 nm) post-SDBS.

Kinetic model

Corona exchange kinetics were modeled by a system of simultaneous adsorption/desorption reactions. The model assumes that both ssDNA and protein adsorb/desorb reversibly to a fixed number of vacant SWCNT surface sites (Equations 1 and 2). Note that all modeling was done on a mass basis. This is in agreement with the general use of volume fractions in polymer thermodynamics.[75] Here, we add the additional assumption that the biomolecules are of similar density. Modeling on a mass basis accounts for the widely varying molecular sizes between the two types of protein (HSA, 66.5 kDa, globular vs. FBG, 340 kDa, long) and ssDNA ($(GT)_6$, 3.7 kDa). The time-dependent differential equations governing ssDNA desorption and protein adsorption are as follows:

$$\frac{d}{dt}[D] = -k_1[*]_T[D] + (k_1[D] + k_2)([D]_T - [D]) + k_1[D]([P]_T - [P]) \qquad \text{(Eq. S2.1)}$$

$$\frac{d}{dt}[P] = -k_3[*]_T[P] + (k_3[P] + k_4)([P]_T - [P]) + k_3[P]([D]_T - [D]) \qquad \text{(Eq. S2.2)}$$

A least-squares regression was used to fit the model to fluorescence data and iterate model parameters. The ode15s function in MATLAB (MathWorks, 2019a) was implemented to solve Equations S2.1 and S2.2 for free protein and DNA concentration curves given fit rate constants k_1, k_2, k_3, k_4, and the total concentration of open sites, $[*]_T$. Relative error between the model fit and experimental data was calculated and averaged over all data points to yield mean relative error (MRE). Sensitivity analysis on initial conditions was performed to minimize this fit error. Forty-eight unique combinations of rate parameter initial conditions were analyzed as inputs to the nonlinear least-squares solver (lsqcurvefit) in our MATLAB model. The optimal set of initial conditions for each protein was chosen as that which yielded a low MRE between fit and experimental data and a low standard error among fit parameters for each of the four protein concentrations. Each rate parameter was individually fit to each experiment, yielding 20 total fit parameters from each initial condition (**Table S2.2**). Final ssDNA and protein fit MRE were all < 5% (**Table S2.2**).

Two alternative models were also attempted: in Model 2, protein was able to bind to surface-adsorbed ssDNA and in Model 3, protein was able to bind to surface-adsorbed protein.

However, these models both produced significantly higher error in fits. Model 2 addressed the possibility of protein binding on top of ssDNA bound directly to the SWCNT. For FBG experiments fit with Model 2, most fits overestimated FBG adsorption and many fits displayed incorrect concavity for the ssDNA desorption. For HSA experiments fit with Model 2, the protein data was generally fit well but the ssDNA fits exhibited either a maximum or produced linear fits. Model 3 addressed the possibility of protein binding on top of protein bound directly to the SWCNT. For FBG experiments, Model 3 overestimated both protein adsorption and ssDNA desorption. For HSA experiments, Model 3 generally fit the protein data well, yet did not capture ssDNA dynamics as a function of concentration. Although the higher errors associated with Model 2 and 3 do not rule out these nanoscale mechanistic possibilities, the simple model of independent binding does overall fit the data much more closely between both protein and ssDNA curves within the same experiment, as well as binding dynamics as a function of varying concentration.

Biomolecule corona exchange assay

Cy3-RNA: UUC CGU AUG UUG CAU CAC CTT (5' Cy3-labeled custom RNA oligo with HPLC purification, Integrated DNA Technologies, Inc.). This particular RNA sequence was chosen because it serves as the antisense strand in a gene silencing study. Exchange was monitored with $(GT)_6$-Cy5-SWCNTs.

Cy5-phospholipid: 1,2-distearoyl-sn-glycero-3-phosphoethanolamine-N-[amino(polyethylene glycol)-2000]-N-(Cyanine 5), abbreviated DSPE-PEG(2000)-N-Cy5 (Avanti Polar Lipids, Inc.). This phospholipid was chosen because it has been previously used to functionalize SWCNT for brain imaging applications.[66] Exchange was monitored with $(GT)_6$-FAM-SWCNTs.

Eosin-peptoid: $(Nae–Npe)_9$-$(Nce–Npe)_9$): N-(2-aminoethyl) glycine (Nae) and N-(2-phenethyl) glycine (Npe) units, abbreviated $(Nae–Npe)_9$, and N-(2-carboxyethyl) glycine (Nce) and Npe, abbreviated $(Nce–Npe)_9$.[76] This peptoid sequence was chosen because it has been used to construct a SWCNT-based nanosensor.[15] Exchange was monitored with $(GT)_6$-Cy5-SWCNTs.

2.7 Supporting Information

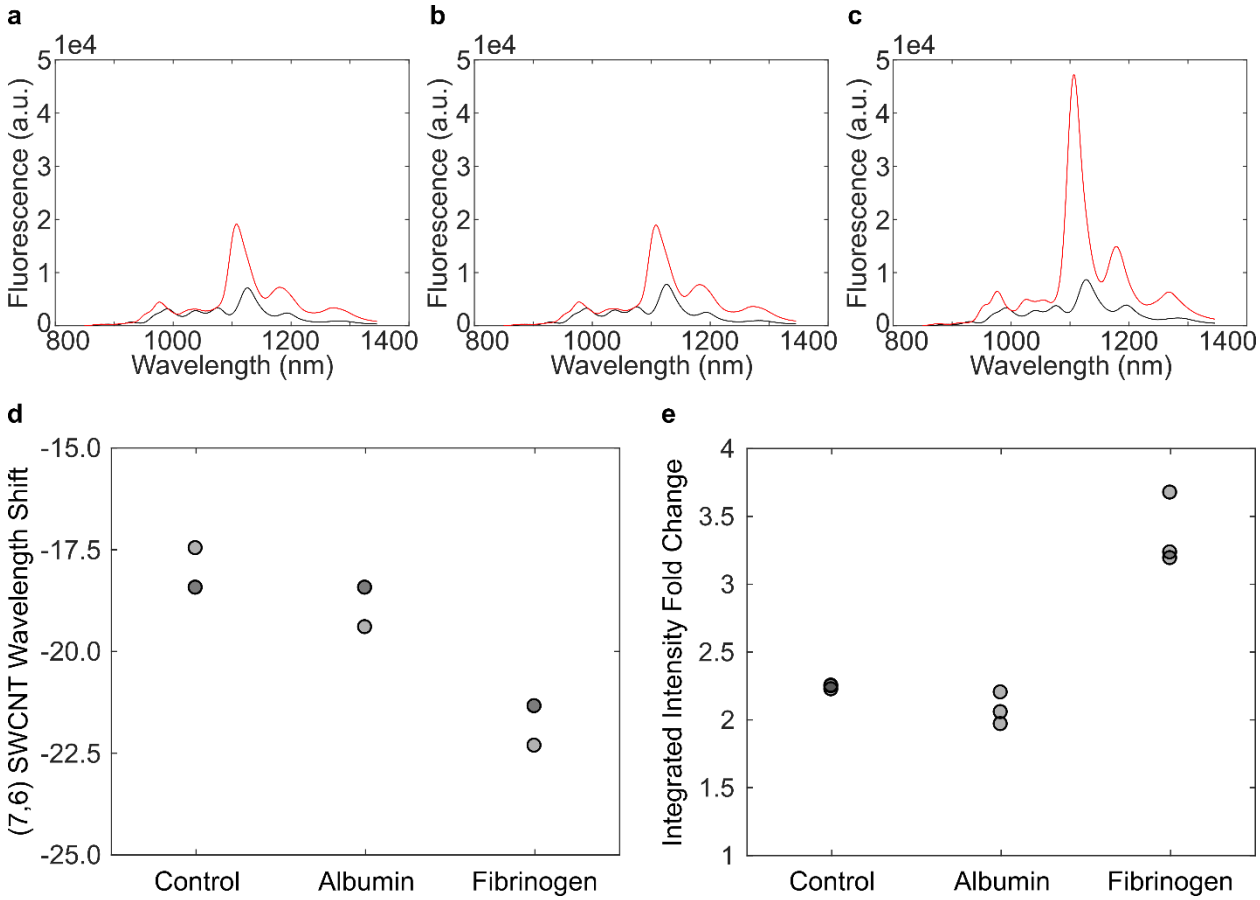

Figure S2.1 Surfactant-induced fluorescence change of ssDNA-SWCNTs incubated with protein. (a) Near-infrared (nIR) spectra of 5 µg/mL $(GT)_6$-SWCNTs before (black) and after (red) addition of 0.5% (w/v) SDBS. **(b–c)** nIR spectra of 5 µg/mL $(GT)_6$-SWCNTs incubated with 40 µg/mL **(b)** albumin or **(c)** fibrinogen for 40 min before (black) and after (red) addition of 0.5% (w/v) SDBS. Change in **(d)** (7,6) SWCNT wavelength of peak emission and **(e)** integrated fluorescence intensity (800-1400 nm) observed 1 min after addition of SDBS (N = 3). Nanosensor excitation was with 721 nm laser.

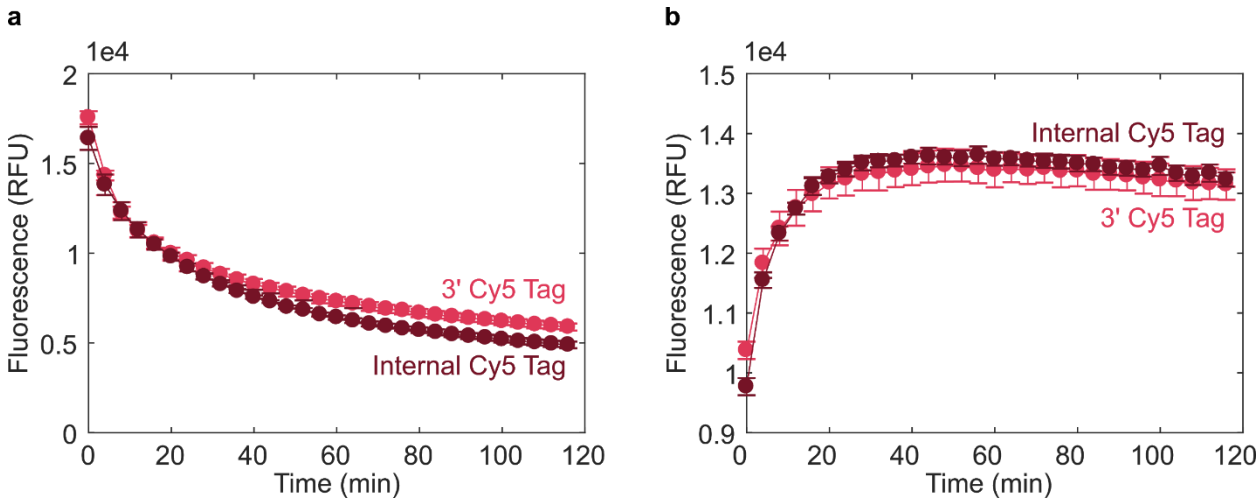

Figure S2.2 Effect of Cy5 tag location on ssDNA adsorption and protein-induced desorption. (a) Cy5 fluorescence tracking of 0.4 µM 3'- or internal-Cy5 tagged $(GT)_6$ ssDNA added to 5 µg/mL unlabeled $(GT)_6$-SWCNT. **(b)** Cy5 fluorescence tracking upon addition of 160 µg/mL fibrinogen, 3 h post-incubation with $(GT)_6$-Cy5. Error bars represent standard error between experimental replicates (N = 3).

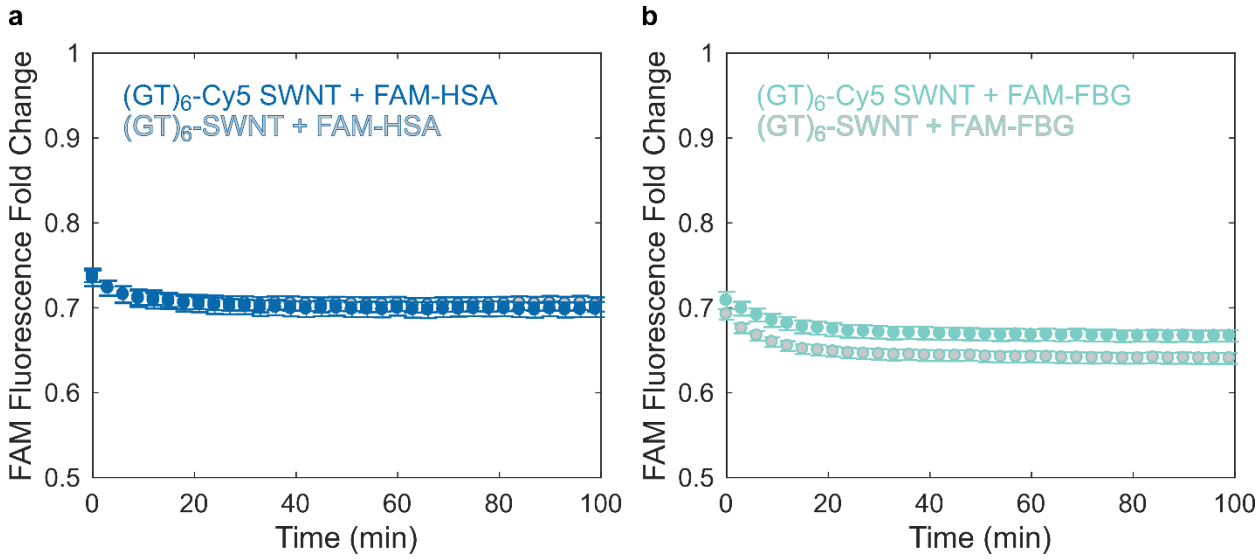

Figure S2.3 Effect of Cy5 ssDNA tag on protein adsorption. Quenching of FAM-protein upon addition of 40 µg/mL **(a)** FAM-HSA or **(b)** FAM-FBG to 5 µg/mL $(GT)_6$-Cy5-SWCNTs or $(GT)_6$-SWCNTs. Error bars represent standard error between experimental replicates (N = 3).

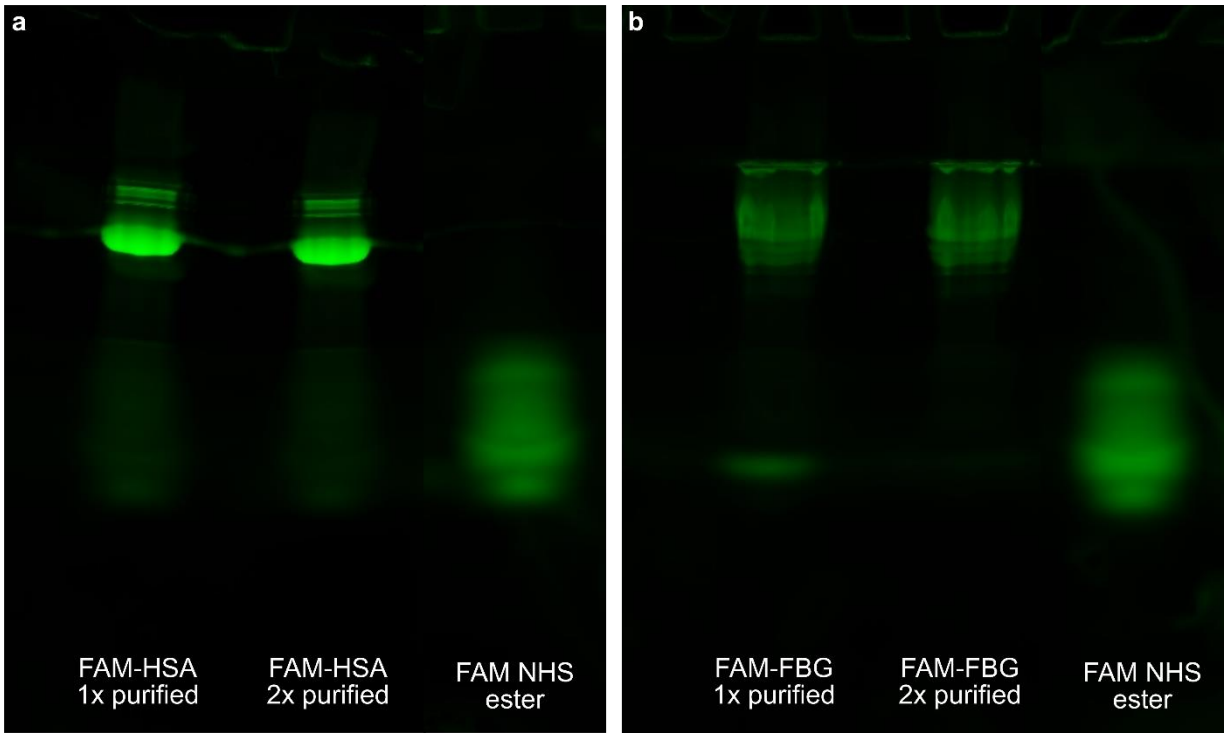

Figure S2.4 Polyacrylamide gel electrophoresis (PAGE) to quantify purification of labeled FAM-protein solutions. 12% acrylamide (total monomer) gel images of FAM-labeled **(a)** albumin (FAM-HSA) and **(b)** fibrinogen (FAM-FBG) post-purification to assess amount of free FAM remaining.

Table S2.1 Quantification of free FAM remaining in labeled FAM-protein solutions. Molar percentages of FAM-protein and free FAM are calculated based on gel band intensity and protein degree of labeling for **(a)** FAM-HSA and **(b)** FAM-FBG.

a

Sample	Band ID	Mole %
FAM-HSA, 1x pure	FAM-Protein	69.7%
	FAM	30.3%
FAM-HSA, 2x pure	FAM-Protein	67.8%
	FAM	32.2%
FAM	FAM	100.0%

b

Sample	Band ID	Mole %
FAM-FBG, 1x pure	FAM-Protein	70.5%
	FAM	29.5%
FAM-FBG, 2x pure	FAM-Protein	86.2%
	FAM	13.8%
FAM	FAM	100.0%

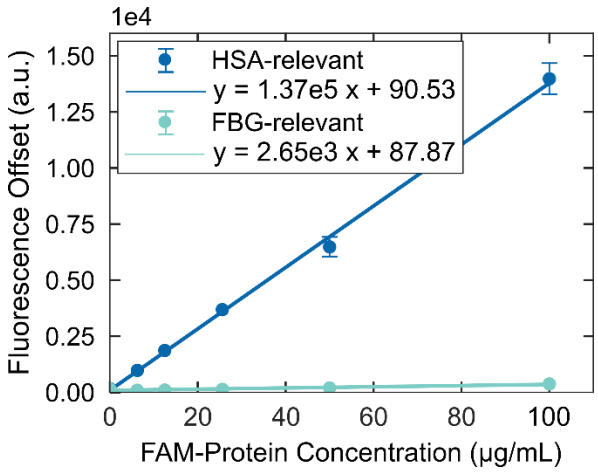

Figure S2.5 Fluorescence offset due to free FAM binding to SWCNT surface. FAM NHS ester was injected into solution with or without SWCNTs to quantify free fluorophore binding to the SWCNT. Free FAM concentrations tested were calculated based on molar percentage of free fluorophore at FAM-HSA or FAM-FBG concentrations between 0 and 100 µg/mL. Fluorescence offset was calculated as the difference between FAM fluorescence in the presence and absence SWCNTs. Offset is incorporated for all data conversion from fluorescence to concentration. Error bars represent standard deviation between technical replicates (N = 3).

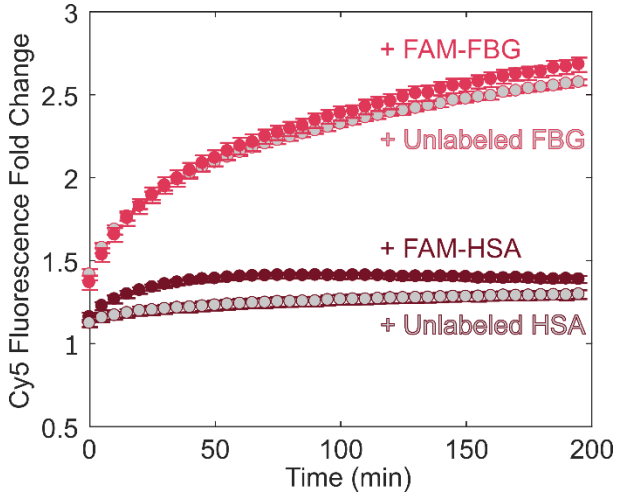

Figure S2.6 Desorption of ssDNA-Cy5 from SWCNT induced by FAM-labeled vs unlabeled protein. Dequenching of $(GT)_6$-Cy5 due to desorption from SWCNT upon addition of 40 µg/mL FAM-protein or unlabeled protein. Error bars represent standard error between experimental replicates (N = 3).

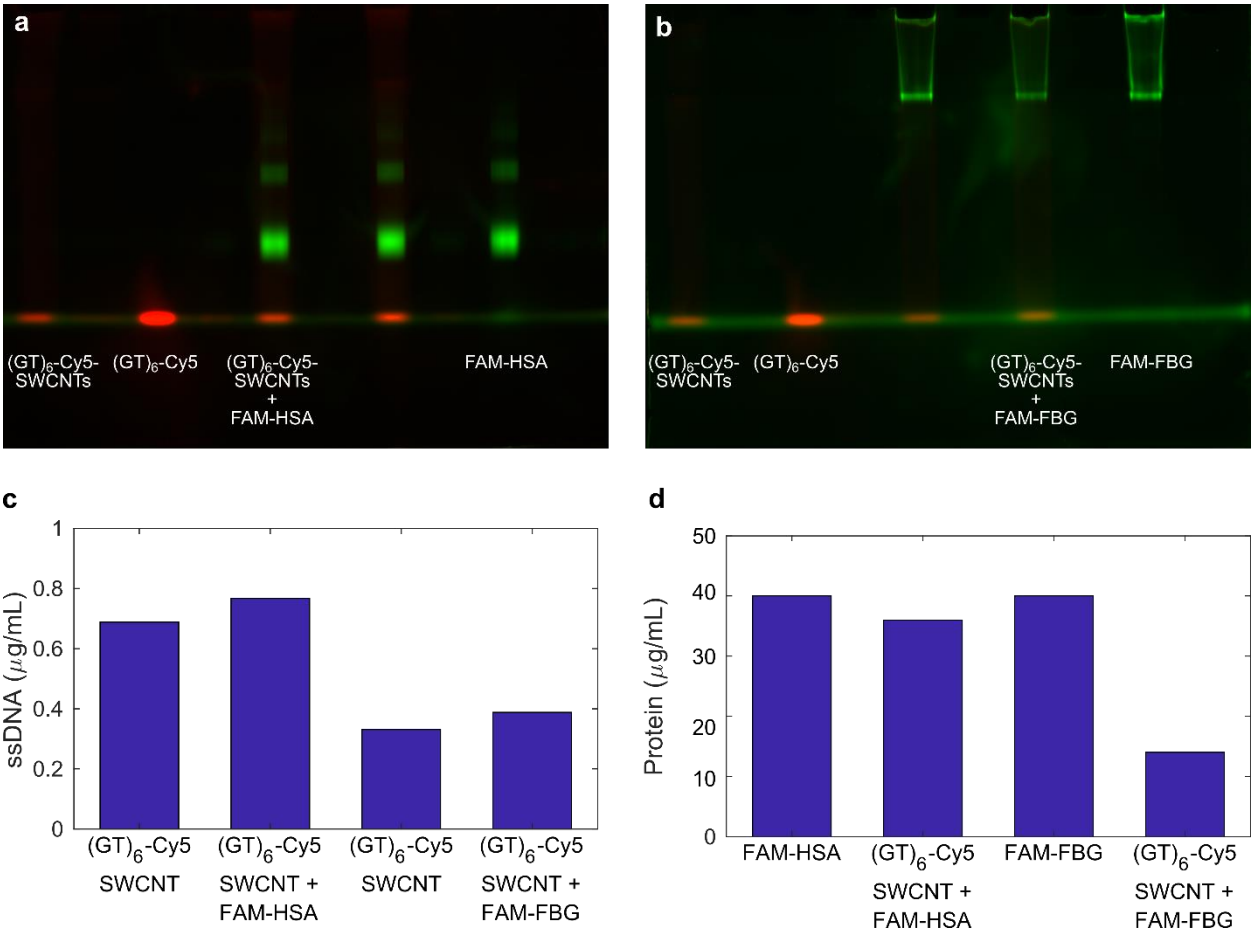

Figure S2.7 Native polyacrylamide gel electrophoresis (PAGE) to quantify ssDNA and protein exchange. Incubation of **(a)** FAM-HSA or **(b)** FAM-FBG proteins with $(GT)_6$-Cy5-SWCNTs for 1 h (final concentrations 5 μg/mL of $(GT)_6$-Cy5-SWCNTs with 40 μg/mL of either FAM-HSA or FAM-FBG). Quantification of concentration via fluorescence for **(c)** Cy5 bands (red) and **(d)** FAM bands (green).

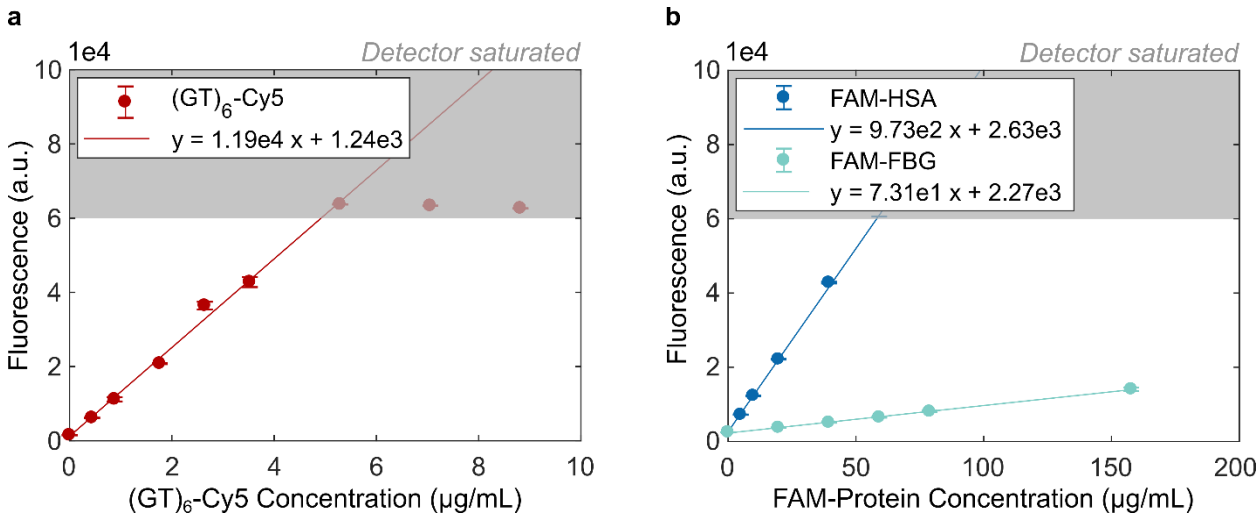

Figure S2.8 Conversion of fluorescence to concentration. Standard curves correlating fluorescence to fluorophore-labeled entity concentration for **(a)** Cy5-labeled $(GT)_6$ and **(b)** FAM-labeled proteins, FAM-HSA and FAM-FBG. Error bars represent standard deviation between technical replicates (N = 3).

Table S2.2 Full kinetic model fit parameters and mean relative errors (MREs).

Protein	Concentration (µg/mL)	k_1 (mL µg^{-1} s^{-1})	k_2 (s^{-1})	k_3 (mL µg^{-1} s^{-1})	k_4 (s^{-1})	$[*]_T$ (µg mL^{-1})	MRE protein	MRE ssDNA
Albumin	5	1.54E-06	8.40E-06	9.44E-06	5.9E-03	364.60	1.21%	0.25%
	10	1.41E-06	1.18E-05	7.86E-06	8.1E-03	525.60	0.83%	0.90%
	40	1.10E-06	1.34E-05	8.87E-06	1.1E-02	514.26	0.35%	3.01%
	60	1.22E-06	2.07E-05	9.34E-06	1.2E-02	483.76	0.41%	2.53%
Fibrinogen	40	1.15E-06	4.27E-05	1.38E-05	2.6E-03	619.82	4.71%	2.96%
	60	2.18E-06	6.64E-05	1.69E-05	3.7E-03	485.72	2.98%	3.47%
	80	2.09E-06	7.65E-05	1.48E-05	5.4E-03	562.90	1.37%	4.14%
	160	2.30E-06	9.09E-05	1.18E-05	9.2E-03	617.74	0.74%	4.74%

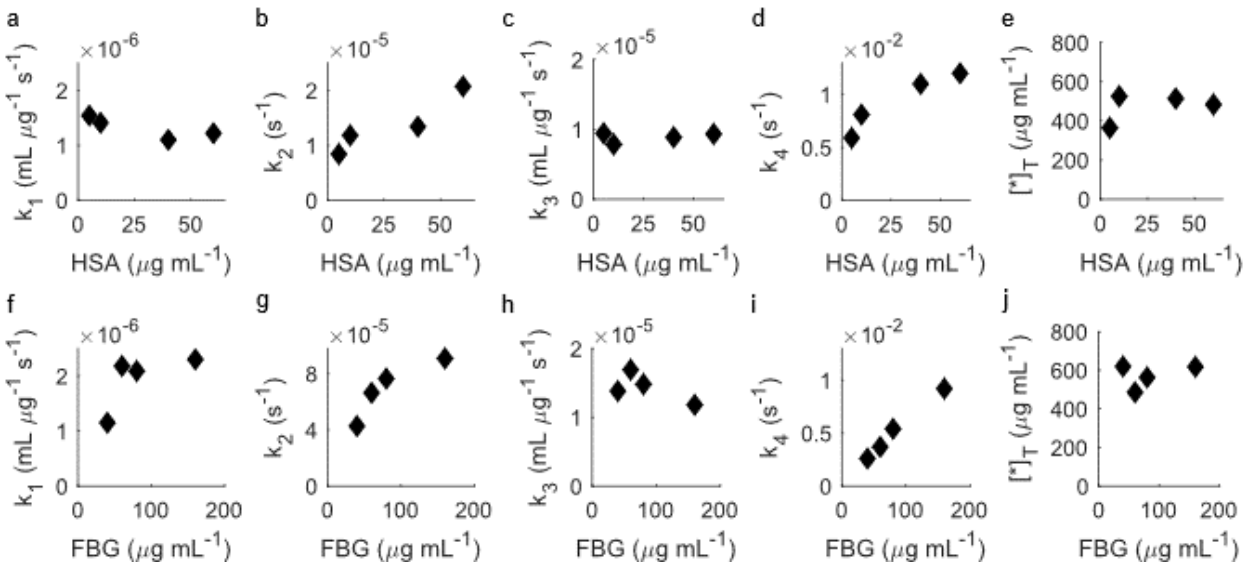

Figure S2.9 Full kinetic model fit parameters as functions of added protein concentrations. Fit parameters of **(a)** k_1 (ssDNA adsorption rate constant), **(b)** k_2 (ssDNA desorption rate constant), **(c)** k_3 (protein adsorption rate constant), **(d)** k_4 (protein desorption rate constant), and **(e)** $[*]_T$ (total SWCNT surface site concentration) for HSA in the top row and **(f–j)** the respective values for FBG in the bottom row.

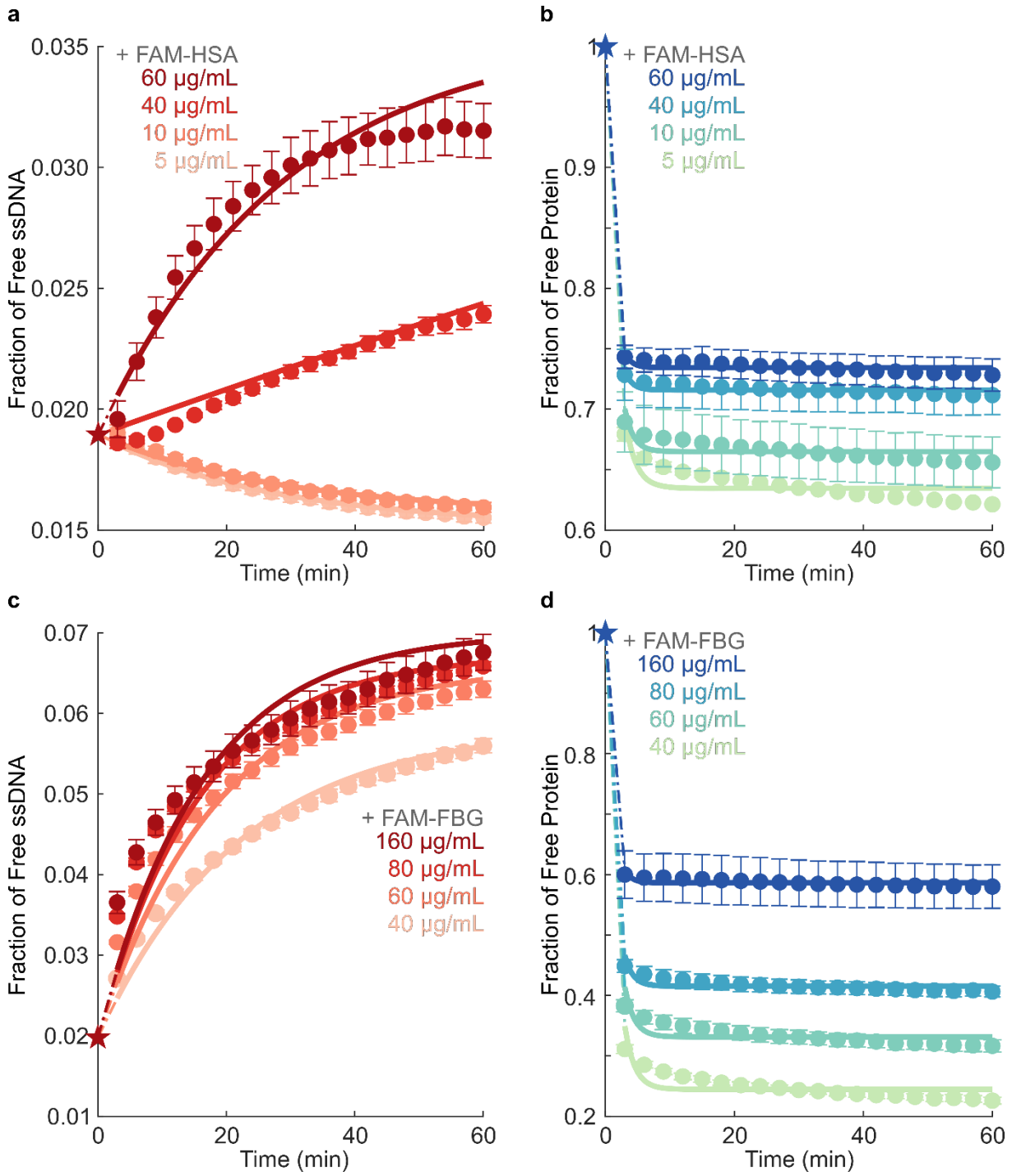

Figure S2.10. Kinetic model of competitive exchange between ssDNA and protein on SWCNTs fit to fluorescence data to extract rate constants, with constrained SWCNT surface site concentration. Fraction of **(a)** $(GT)_6$-Cy5 ssDNA and **(b)** FAM-labeled albumin (FAM-HSA) protein free in solution for varying concentrations of FAM-HSA injected into 5 µg/mL $(GT)_6$-Cy5-SWCNT solution. Fraction of **(c)** $(GT)_6$-Cy5 ssDNA and **(d)** FAM-labeled fibrinogen (FAM-FBG) protein free in solution for varying concentrations of FAM-FBG injected into $(GT)_6$-Cy5-SWCNT solution. Star data points represent initial conditions used for solving model differential equations. Curves were fit with constrained $[*]_T$ per protein. Error bars represent standard error between experimental replicates (N = 3).

Table S2.3 Full kinetic model fit parameters and mean relative errors (MREs) for fitting with constrained SWCNT surface site concentration.

Protein	Concentration (μg/mL)	k_1 (mL μg^{-1} s^{-1})	k_2 (s^{-1})	k_3 (mL μg^{-1} s^{-1})	k_4 (s^{-1})	$[*]_T$ (μg mL^{-1})	MRE protein	MRE ssDNA
Albumin	5	1.47E-06	9.58E-06	8.74E-06	6.41E-03	429.69	1.24%	0.37%
	10	1.38E-06	9.25E-06	9.92E-06	8.29E-03		0.84%	0.63%
	40	6.93E-08	2.18E-06	1.06E-05	1.11E-02		0.35%	1.83%
	60	1.35E-06	2.04E-05	1.06E-05	1.19E-02		0.41%	2.66%
Fibrinogen	40	8.51E-07	4.41E-05	9.73E-06	2.64E-03	871.49	4.76%	2.52%
	60	1.01E-06	5.91E-05	9.14E-06	3.74E-03		3.00%	4.06%
	80	1.19E-06	7.04E-05	9.34E-06	5.43E-03		1.38%	4.46%
	160	1.20E-06	7.22E-05	7.96E-06	9.03E-03		0.74%	5.64%

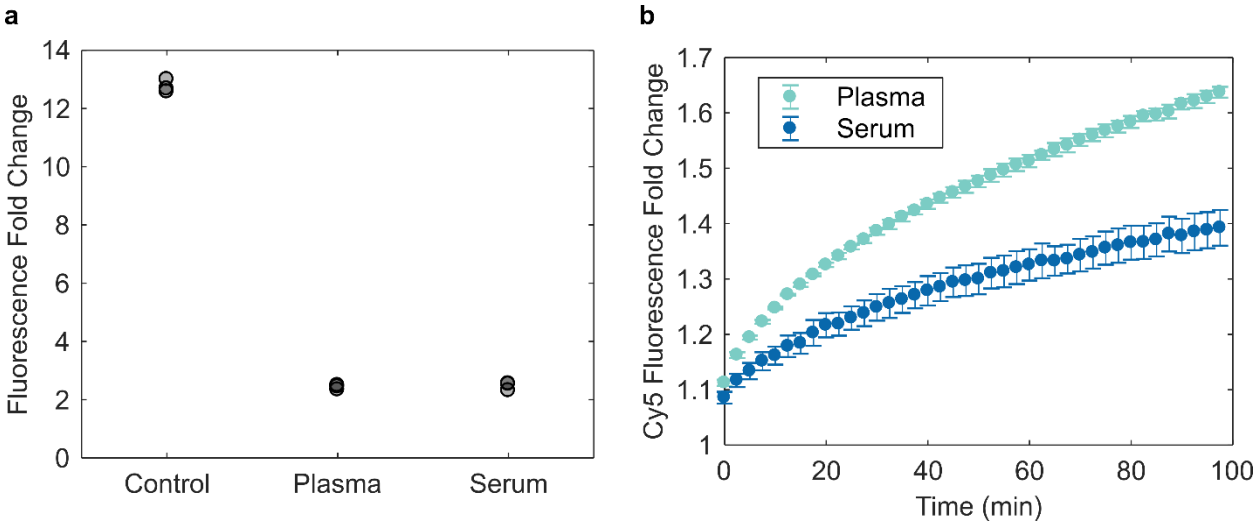

Figure S2.11. Comparison of plasma- vs serum-induced effects on ssDNA-SWCNTs. (a) Change in 1200 nm fluorescence intensity of 5 μg/mL $(GT)_6$-SWCNTs, pre-incubated for 40 min with PBS, plasma, or serum normalized to 40 μg/mL total protein concentration, before and after addition of 200 μM dopamine (N = 3). Nanosensor excitation was with 721 nm laser. **(b)** $(GT)_6$-Cy5 fluorescence fold change upon desorption from 5 μg/mL SWCNTs induced by addition of plasma or serum, 40 μg/mL total protein concentration. Error bars represent standard error between experimental replicates (N = 3).

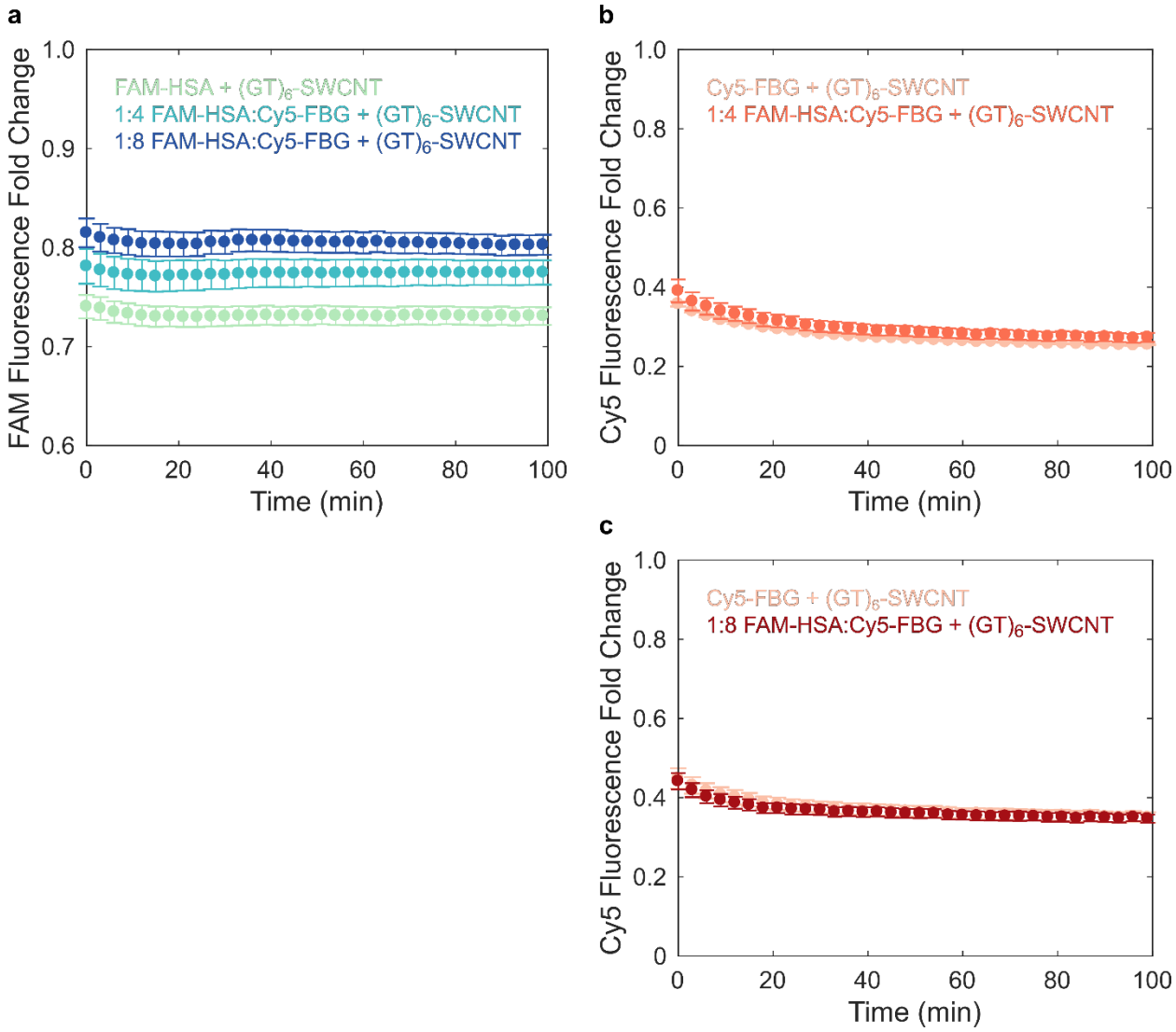

Figure S2.12. Tracking competitive adsorption of two protein species onto SWCNT surface. (a) Adsorption of 20 μg/mL FAM-HSA to 5 μg/mL $(GT)_6$ SWCNTs tracked by FAM quenching in the presence of Cy5-conjugated FBG at 0, 80, and 160 μg/mL. **(b–c)** Comparison of Cy5-FBG adsorption in the presence and absence of 20 μg/mL FAM-HSA, with Cy5-FBG concentrations of **(b)** 80 μg/mL and **(c)** 160 μg/mL. Error bars represent standard error between experimental replicates (N = 3).

Chapter 3:
Interaction of SWCNTs with Microglia

Portions of this chapter are reproduced and adapted with permission from Ref 23. Copyright 2020 American Chemical Society.

3.1 Introduction

Nanoscale neurotechnologies often demonstrate increased biocompatibility and less invasive implementation than their micro- or macro- scale counterparts,[77] and can offer higher signal-to-noise ratios owing to the relatively large surface area of nanoscale materials.[78] For this reason, engineered nanoparticles have recently demonstrated broad-scale utility in neuroscience for neurological recordings,[79] drug delivery across the blood-brain barrier,[80] and for brain imaging.[81] In particular, carbon nanotubes have shown increasing applicability for neuron stimulation, electrochemical recordings of neuron action potentials, mapping brain extracellular space, deep-brain imaging, and imaging neurotransmission.[1,2,6,82–85] Towards the last point, recent developments are enabling imaging of chemical communication between cells, specifically for a class of neurotransmitters known as neuromodulators whose imaging has eluded existing methods of inquiry.[86] Previous work includes development of a nanoscale near-infrared catecholamine probe, nIRCat, that can capture dopamine release and reuptake kinetics in the brain striatum, and measure the influence of drugs on these signaling properties.[1] nIRCat is synthesized by noncovalent conjugation of $(GT)_6$ single stranded DNA (ssDNA) and near-infrared (nIR) fluorescent single-walled carbon nanotubes (SWCNTs).[12] However, as these and numerous other nanoscale neurotechnologies based on SWCNTs are used to probe the brain microenvironment, it becomes important to understand how these nanoparticles affect surrounding brain tissue.

Carbon nanomaterials have previously been implicated in activation of the innate immune system across multiple biological organisms and through numerous mechanisms. For example, nonspecific adsorption of complement proteins in serum causes recognition of carbon nanotubes and activation of the complement system.[53] However, the biological impact of carbon nanomaterials—particularly those with pristine graphene lattices—has not been well characterized in the brain, whereas other classes of nanomaterials, particularly metallic nanoparticles, have been shown to induce an inflammatory response in brain tissue.[87–89] Inflammation in the brain has long been associated with multiple negative health outcomes including neurotoxicity, neurodegeneration, and loss of function.[90,91] These effects are particularly consequential in the context of studying chemical neurotransmission. Therefore, it is imperative to characterize and quantify the extent to which carbon nanotubes induce an inflammatory response in the brain and if such effects can be mitigated.

Microglia are specialized immune cells found in the central nervous system. Recognition of tissue damage or pathogenic material causes microglial activation, characterized by a change in cell morphology and an inflammatory response. This response promotes clearance of the pathogen through phagocytosis, and has been shown to result in neurotoxicity and reduced dopamine concentrations in the striatum.[92,93] Larger multi-walled carbon nanotubes with carboxylic acid functionalization have previously been found to negatively impact microglial phagocytosis processes.[94,95] Therefore, probing the impact of carbon nanotubes on microglia is of critical

importance to assess the biocompatibility of SWCNT-based neuro-technologies. Here, we examine the effect elicited by SWCNT neuro-sensors on SIM-A9 mouse microglial cells. This cell line was spontaneously immortalized and has been used to study the microglial inflammatory phenotype.[96]

3.2 Cell Morphological Response

We first studied the effects of the $(GT)_6$-SWCNT catecholamine nanosensor on SIM-A9 microglial cell morphology, a phenotypic marker of microglial activation that affects cell migration. Specifically, a morphology change from round to ramified is characteristic of microglial activation *in vitro*.[97] Incubation of SIM-A9 microglia with 5 µg/mL $(GT)_6$-SWCNTs resulted in drastic cell morphology change within 4 h post-exposure. Cells progressed from round, amoeboid morphologies to highly branched, ramified structures displaying elongated cellular processes (**Figure 3.1a**), while control cells absent from exposure to $(GT)_6$-SWCNTs retained a round morphology (**Figure 3.1b**). Live-cell imaging time lapse videos show control SIM-A9 populations consisted of round, highly motile cells. Incubation of cells with (GT)-SWCNTs caused immediate ramification of SIM-A9 microglia and loss of cell motility during the first two hours post exposure.

Cell morphology change in the $(GT)_6$-SWCNT-treated cells coincided with actin cytoskeletal growth as measured with F-actin probe phalloidin conjugated with Alexa Fluor 488, forming projections resembling microglial filopodia (**Figure 3.1c–f**). These projections are known to be responsible for increasing microglial cell surface area within the brain microenvironment as a result of microglial activation and are typically found at the tips of microglial processes.[98,99] Conversely, we observe that $(GT)_6$-SWCNT exposure promoted growth of projections along the entire length of the cell branches, not only at the tip of microglial processes (**Figure 3.1e**). Interestingly, positive control experiments of SIM-A9 cells incubated with lipopolysaccharide (LPS), a class of molecule found in gram-negative bacterial cell walls known to activate toll-like receptor 4 (TLR4) and induce a strong inflammatory response, induced a relatively marginal change in cell morphology compared to $(GT)_6$-SWCNT exposure. Hence, the pathway of microglial activation by SWCNTs may be distinct from previously observed TLR4 activation by carbon nanomaterials.[100] Carboxylic acid functionalized SWCNTs (COOH-SWCNTs) were included as an additional positive control, and similarly induced a marginal change in cell morphology compared to $(GT)_6$-SWCNTs. These latter results suggest a strong influence of nanomaterial surface chemistry on nanoparticle biocompatibility.

Cell morphology change in time lapse videos was quantified by assigning each cell with a form factor value computed by the following equation:

$$f = \frac{4\pi A}{P^2} \qquad \text{(Eq. 3.1)}$$

where A is the area occupied by a cell and P is the perimeter of the cell.[101] Form factor values near 1 therefore indicate round cells (**Figure 3.1g**), whereas decreasing values of f correlate with higher degrees of ramification (**Figure 3.1h–i**). Untreated SIM-A9 cells reveal a defined population of cells with form factors near 0.8 (**Figure 3.1j**). Following a 3 h incubation of SIM-A9 cells with 5 ng/mL LPS or 5 µg/mL COOH-SWCNTs, this f = 0.8 peak is diminished, whereas in cells treated with 5 µg/mL $(GT)_6$-SWCNTs, the peak at f = 0.8 is not observed and instead skews to lower form factor values. To determine the time-dependence of this morphology change, we performed live-

cell imaging of the above samples and averaged the form factor values of all cells within a given field of view to track progression of mean cell form factor for 24 h post-treatment. Following addition of $(GT)_6$-SWCNTs, an immediate decrease in mean form factor occurred within 1 h (**Figure 3.1k**). Presence of $(GT)_6$-SWCNTs caused mean form factor to decrease to a minimum of 0.288 ± 0.011 at 4.5 h post-exposure, compared to a minimum value of 0.473 ± 0.010 for untreated control cells. LPS-stimulated cells reached a minimum mean form factor of 0.377 ± 0.004 at 2.5 h post-exposure and returned to near baseline levels after approximately 7.5 h. Conversely, SWCNT-stimulated cells failed to return to morphologies consistent with the control cell population within 24 h. The mean form factor of $(GT)_6$-SWCNT treated SIM-A9 24 h post-exposure was 0.395 ± 0.005 compared to 0.483 ± 0.10 for untreated control cells. Normalizing all samples including LPS by mass concentration to 5 µg/mL did not result in a comparable LPS-mediated morphology change (**Figure S3.1**).

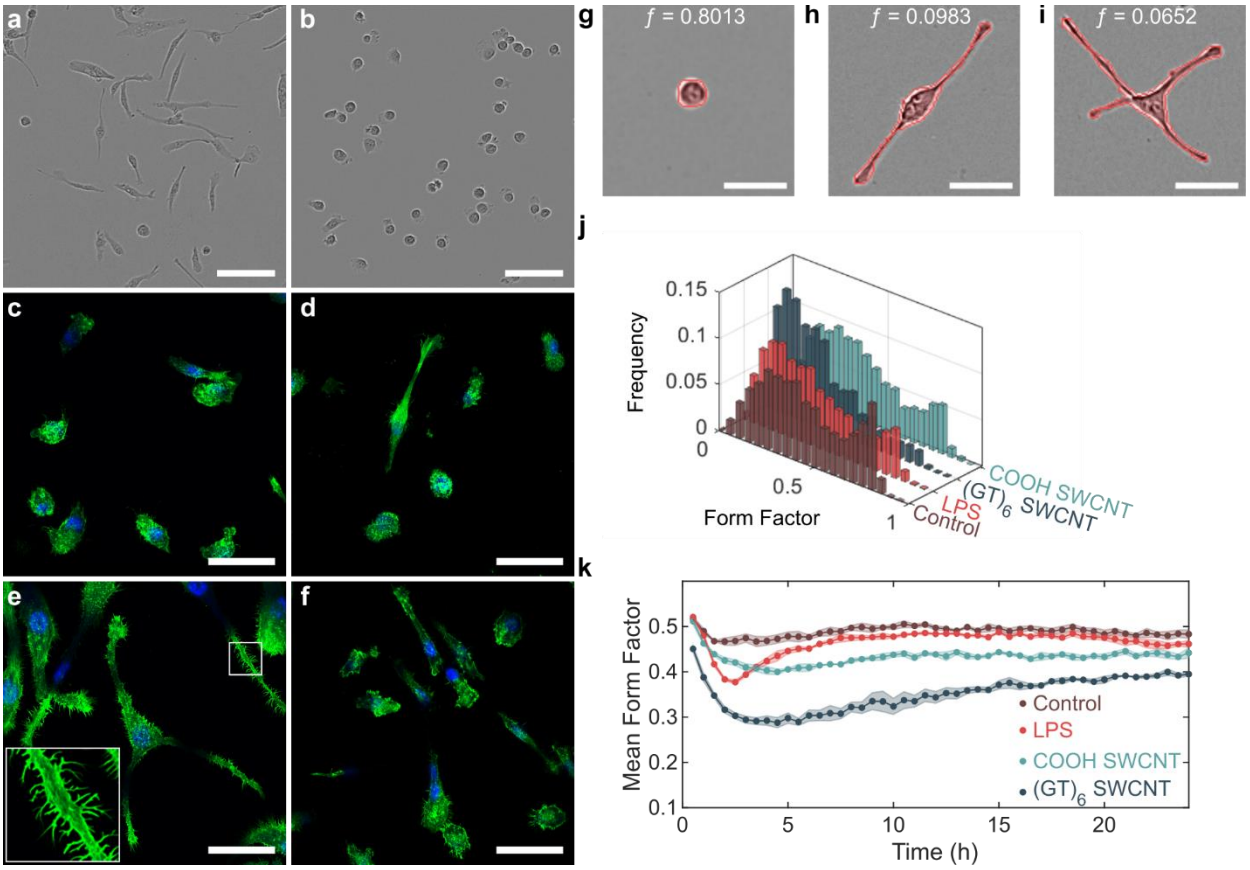

Figure 3.1 SWCNT-induced morphology change in SIM-A9 microglial cells. (a–b) Phase contrast images of SIM-A9 microglia following 4 h incubation with **(a)** 5 µg/mL $(GT)_6$-SWCNT or **(b)** PBS. Scale bars are 100 µm. **(c–f)** Confocal fluorescence microscopy images of FAM-stained F-actin (green) of fixed microglia following 4 h incubation with **(c)** PBS, **(d)** 5 ng/mL LPS, **(e)** 5 µg/mL $(GT)_6$-SWCNT, and **(f)** 5 µg/mL COOH-SWCNT. Nuclei are counterstained with DAPI (blue). Scale bars are 50 µm. **(g–i)** Example SIM-A9 morphologies and corresponding form factor values for **(g)** round, **(h)** bipolar, and **(i)** multipolar cells. Outlines of the identified cells are shown in red. Scale bar is 50 µm. **(j)** Form factor distribution following 3 h incubation with PBS (control), 5 ng/mL LPS, 5 µg/mL $(GT)_6$-SWCNT, and 5 µg/mL COOH-SWCNT. **(k)** Tracking of mean form factor per field of view capture over 24 h. Shaded regions represent standard error of the mean (N = 3).

The extent of cell ramification caused by $(GT)_6$-SWCNTs was concentration-dependent from 0.1 to 5 µg/mL (**Figure 3.2a**), coinciding with a SWCNT concentration range relevant for neuro-applications.[1] To confirm that the observed morphology changes were due to SWCNTs and not the $(GT)_6$ oligonucleotide alone, we imaged SIM-A9 cells exposed to $(GT)_6$-ssDNA. We found that 1.67 µM $(GT)_6$-ssDNA oligonucleotides alone did not cause a significant change in SIM-A9 cell morphology at any time point within a 24 h live-cell imaging experiment (**Figure 3.2b**). This concentration corresponds to the total DNA concentration in a 10 µg/mL $(GT)_6$-SWCNT suspension, further suggesting that the above-discussed effects are induced by the SWCNT carbon lattice.

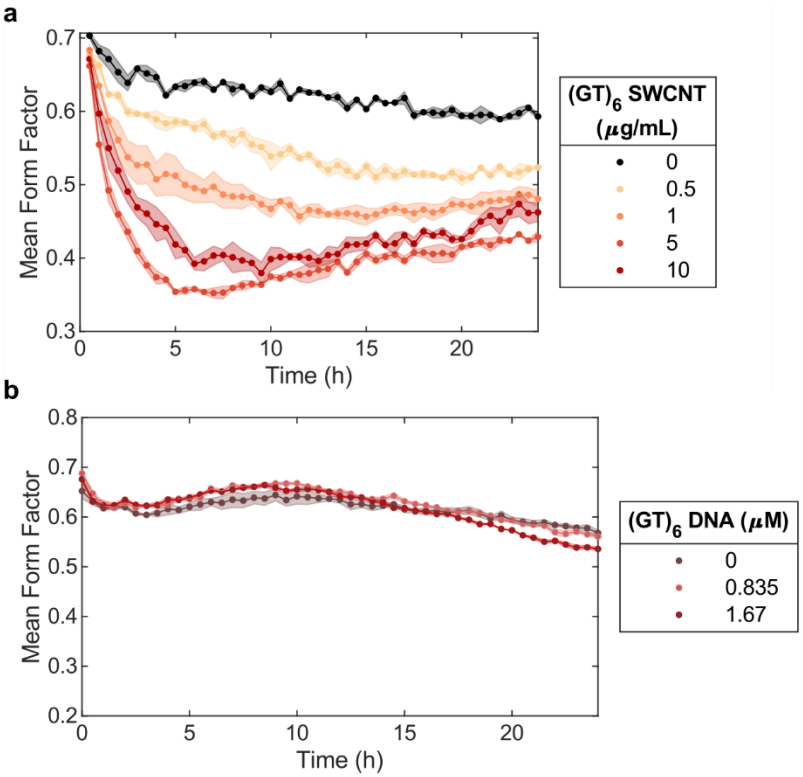

Figure 3.2 Effect of $(GT)_6$-SWCNT on mean cell form factor. (a) Change in mean morphology upon addition of $(GT)_6$-SWCNT ranging in concentration from 0 to 10 µg/mL. SIM-A9 cells were at 37°C and 5% CO_2, in sera free media. **(b)** Change in mean cell form factor upon addition of free $(GT)_6$ ssDNA at concentrations equivalent to total ssDNA concentration in 5 and 10 µg/mL $(GT)_6$-SWCNT suspensions.

3.3 Internalization of SWCNTs

Carbon nanomaterials of many morphologies including SWCNTs, multiwalled carbon nanotubes (MWCNT), and graphene have long been shown to internalize within mammalian cells through a variety of energy dependent mechanisms.[102–104] Tuning the surface chemistry of SWCNTs has been shown to impact the exact mechanism of endocytosis, however most sources

cite clathrin-mediated endocytosis as a primary route of entry.[105] This issue is particularly noteworthy for the use of SWCNT probes in brain tissue as neurotransmitter release and reuptake is an extracellular phenomenon. Previous imaging experiments of SWCNT localization in brain tissue have shown SWCNTs localized to puncta approximately 10–20 μm in diameter, consistent with the size of cells (**Figure 1.4b**). Uptake of SWCNTs into cells sequesters neuro-sensor from the extracellular region, decreasing the concentration available for sensing. Hence, evaluating the degree of SWCNT internalization is vital in designing an effective neurotransmitter probe.

$(GT)_6$-SWCNTs (5 μg/mL) were observed to internalize into SIM-A9 cells within 1 h of incubation at 37°C, 5% CO_2 (**Figure 3.3a**). Internalized SWCNT signal excluded the cell nuclei. This is consistent with work showing SWCNTs lacking nuclear localization signal motifs fail to access the cell nucleus.[106] We find that internalization is energy-dependent, as observed by the absence of SWCNT internalization in SIM-A9 cells at 4°C (**Figure 3.3b**). Previous studies of SWCNT internalization in mammalian cells have determined the internalization mechanism to be predominantly energy-dependent clathrin-mediated endocytosis.[107,108] No correlation was found between degree of internalization and cell morphology at 2 h post exposure to SWCNTs (**Figure 3.3c–d**), suggesting that the cellular morphological change is due to cell signaling rather than a physical interaction between SWCNTs and actin filaments.

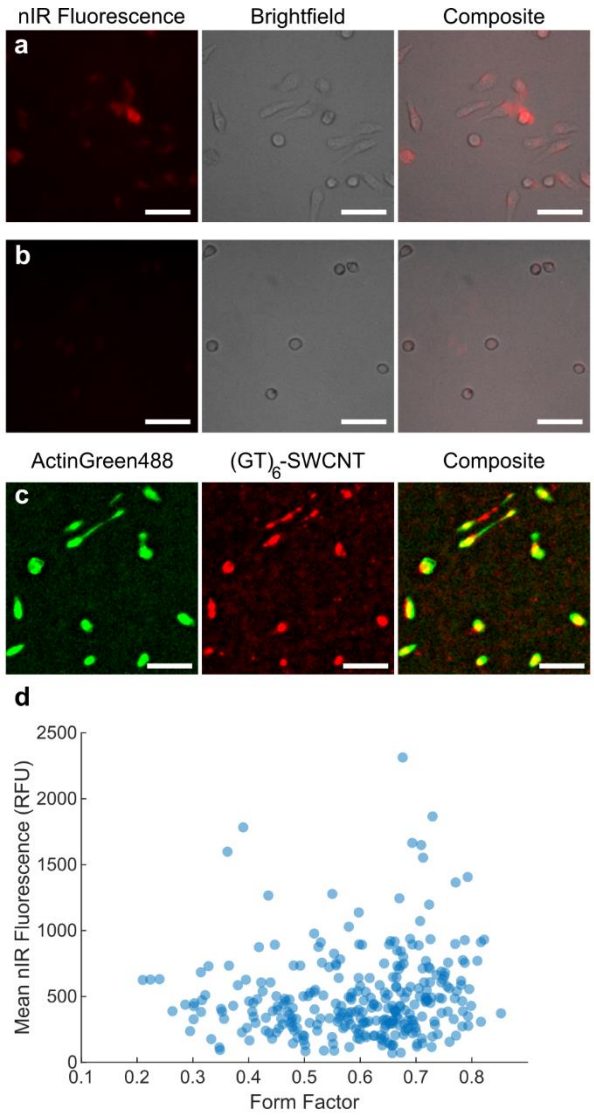

Figure 3.3 Internalization of $(GT)_6$-SWCNTs in SIM-A9 microglia. (a–b) SWCNT fluorescence, brightfield and composite images of fixed SIM-A9 microglia post incubation with 5 μg/mL $(GT)_6$-SWCNT for 1 hr at **(a)** 37°C and **(b)** 5°C. Scale bars are 20 μm. **(c)** Representative fluorescence images of ActinGreen488 stained SIM-A9 cells and internalized $(GT)_6$-SWCNTs following 2 h incubation at 37°C, 5% CO_2. Images are median filtered, background subtracted, and contrast adjusted. Scale bars are 20 μm. **(d)** Scatter plot of cell form factor versus the mean internalized nIR fluorescence signal. Form factor was calculated using the cell perimeter and area calculated from green fluorescence channel images of the stained actin cytoskeleton. A total of 302 cells were identified across 9 field of view captures of paired Alexa 488 and SWCNT fluorescence channels.

SWCNTs also impact the ability of SIM-A9 cells to internalize other material through phagocytosis. We find that phagocytosis of fluorescent Zymosan particles by SIM-A9 cells was diminished following exposure to concentrations greater than or equal to 0.5 μg/mL SWCNTs (**Figure 3.4**), where reduced phagocytosis is characteristic of quiescent, ramified microglia in rats, coinciding with a morphology change.[109]

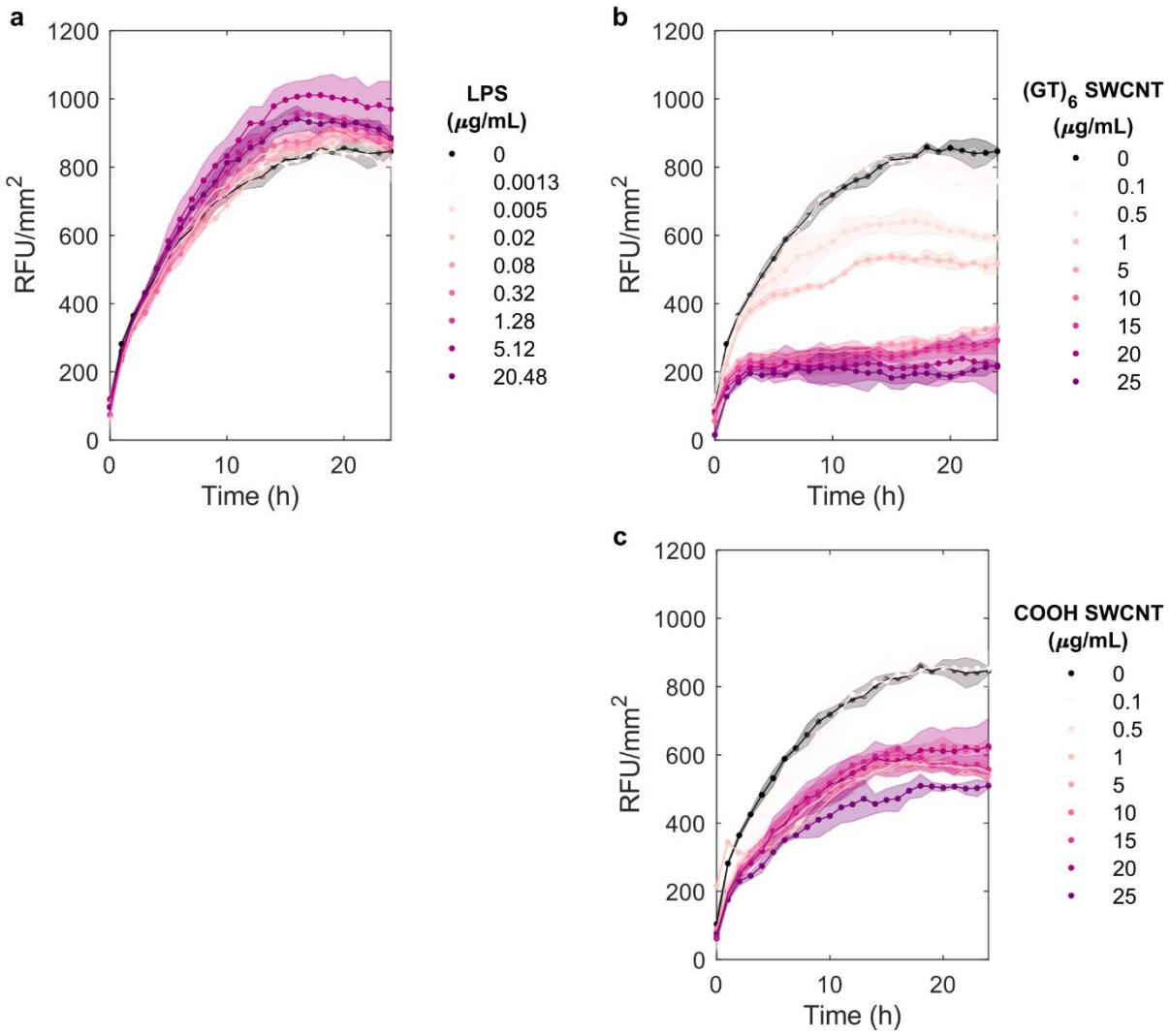

Figure 3.4 SIM-A9 phagocytosis of fluorescent Zymosan bioparticles. (a–c) Fluorescence live-cell imaging of pHrodo Red Zymosan Bioparticles (Sartorius) uptake by phagocytosis in SIM-A9 microglia following 3 h exposure to varying concentrations of **(a)** LPS, **(b)** $(GT)_6$-SWCNT, and **(c)** COOH-SWCNT. Shaded regions represent standard error of the mean (N = 3).

3.4 SWCNT Induced Cytotoxicity

Measuring the effect of SWCNTs on cell viability is a particularly challenging issue in the field of carbon nanotube bionanotechnologies. Carbon nanomaterials have been shown to directly interact with many common vitality assays. The presence of SWCNTs has been shown to cause false positives in toxicity for some common assays such as the MTT assay and false negatives for others (e.g. WST-1 and LDH assays).[110] These are caused by a number of factors including interaction of SWCNTs with tetrazolium dyes such as that used in the MTT assay, adsorption of assay targets to SWCNT surface, and absorbance of light by SWCNTs contributing to plate reader measurement error.[110,111] In the lactate dehydrogenase (LDH) assay which measures activity of LDH in supernatant as a measure for toxicity, the absorbance spectra of the chromophore product

both decreases and redshifts in the presence of carbon nanomaterials.[111] This results in underreporting of the cytotoxicity induced by carbon nanotubes on cell cultures, where a maximum of approximately 25% cell death is reported for concentrations greater than 20 μg/mL (**Figure 3.5a**). However, live cell imaging reveals clear SIM-A9 cell necrosis at these concentrations (**Figure 3.5b–c**). The inability of these assays to accurately predict viability in a cell tissue culture leads to many issues in the assessment of SWCNT toxicity as these bulk assays are readily available tests for novel bionanotechnologies.

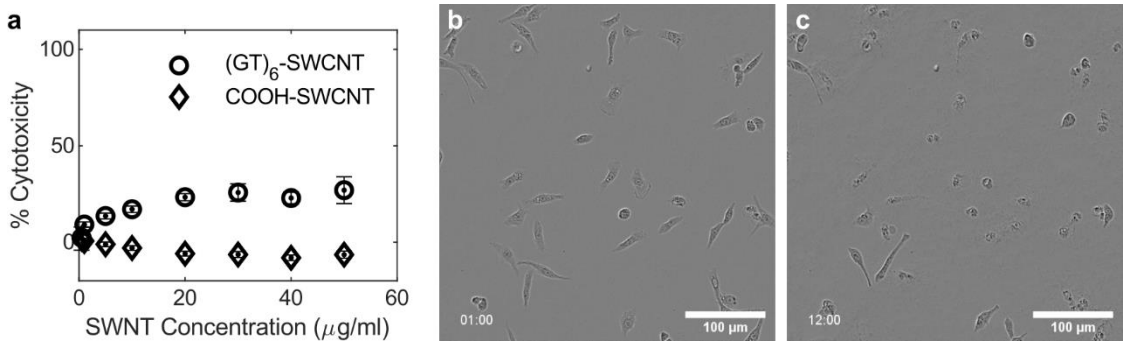

Figure 3.5 Erroneous reporting of SWCNT cytotoxicity using lactate dehydrogenase (LDH) assay. (a) Percent cytotoxicity observed via LDH assay in bulk SIM-A9 cell tissue culture upon addition of $(GT)_6$-SWCNT and COOH-SWCNT at varying concentrations from 1 to 50 μg/mL. Error bars represent standard error of the mean (N = 3). **(b–c)** Images from live-cell imaging of 20 μg/mL $(GT)_6$-SWCNT incubated SIM-A9 microglia after **(b)** 1 h and **(c)** 12 h exposure. Latter time point reveals widespread cell necrosis. Time stamps are hh:mm format. Scale bars are 100 μm.

Flow cytometry assays which utilize dyes permeable to damaged membranes such as propidium iodide (PI) fare better due to the removal of excess SWCNT prior to imaging. Cells were gated using forward and side scatter signal to exclude cell debris and doublets (**Figure S3.3a**). Internalized PI fluorescence revealed dead cells (**Figure S3.3a–b**). Cell death was observed following 2 h incubation with $(GT)_6$-SWCNTs at concentrations greater than or equal to 5 μg/mL (**Figure 3.6a**). LPS did not induce any appreciable cell death while COOH-SWCNT caused less toxicity than $(GT)_6$-SWCNT (**Figure 3.6b**). This may be due to the lower colloidal stability of COOH-SWCNT compared to $(GT)_6$-SWCNT, resulting in faster coalescence of COOH-SWCNT in cell culture media. This is evidenced by zeta potential (ζ) measurements of the suspensions, where ζ = -27.2 mV for COOH-SWCNT and ζ = -69.5 for $(GT)_6$-SWCNT (**Figure S3.2**). The higher in magnitude zeta potential of $(GT)_6$-SWCNT is due to the electrostatic repulsion imparted by adsorbed, negatively-charged ssDNA molecules.[112]

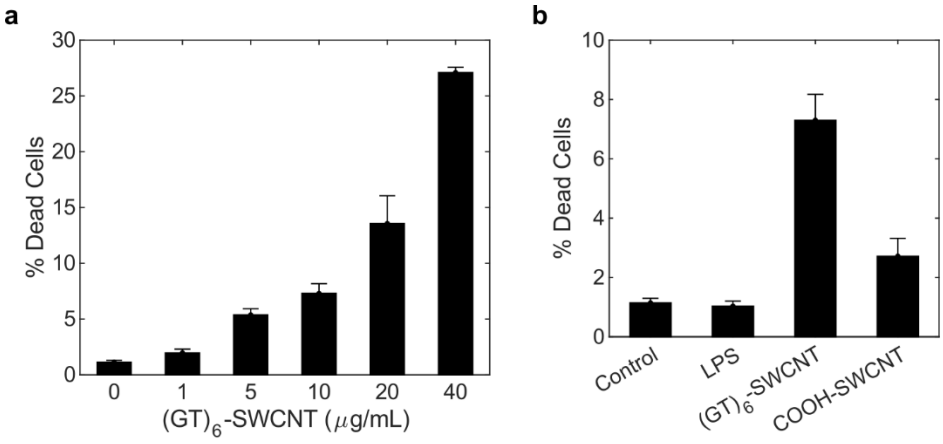

Figure 3.6 Viability assays of SIM-A9 cells treated with neuro-sensor. (a) Flow cytometry of propidium iodide stained SIM-A9 cells pre-treated with varying concentrations of $(GT)_6$-SWCNT. Percent dead cells reflects the fraction of cells positively stained for propidium iodide. Error bars reflect standard error of the mean (N = 3). **(b)** Comparison of dead cell percentage for treatment with 5 ng/mL LPS, 5 μg/mL $(GT)_6$-SWCNT, and 5 μg/mL COOH-SWCNT. Error bars reflect standard error of the mean (N = 3).

A possible indirect method of measuring SWCNT cytotoxicity utilizes previously discussed live-cell imaging data of SIM-A9 microglia with various treatments. Plotting cell growth over time reveals a large decrease in cell proliferation for SWCNT treatments compared to LPS and control (**Figure 3.7**). LPS (10 ng/mL) caused the cell count per imaging area to decrease by 38 ± 3% while 10 μg/mL $(GT)_6$-SWCNT and COOH-SWCNT caused 73 ± 8% and 72 ± 8% reductions in cell density respectively. Concentrations of $(GT)_6$-SWCNT greater than 1 μg/mL caused reductions in cell growth where 5 μg/mL $(GT)_6$-SWCNT significantly reduced the rate of cell proliferation after 14 h incubation (**Figure S3.5**).

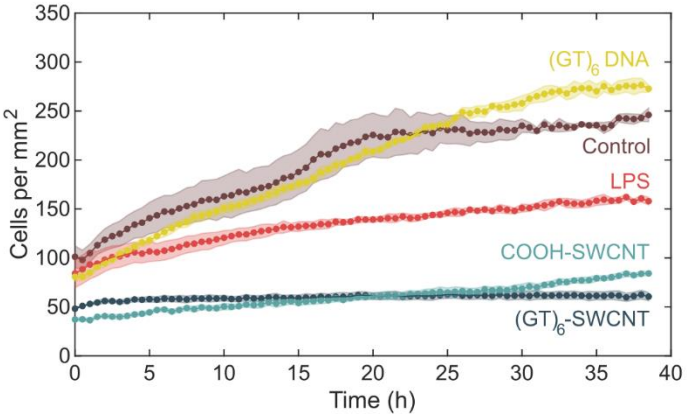

Figure 3.7 Effect of SWCNT on SIM-A9 cell proliferation. Number of cells per mm^2 of cell culture surface for SIM-A9 microglial incubated with PBS, 10 ng/mL LPS, 10 μg/mL $(GT)_6$-SWCNT, 10 μg/mL COOH-SWCNT, and

This method of quantifying toxic effects of SWCNTs on cell population viability appears more sensitive than techniques included bulk viability assays and FACS with Annexin staining,

identifying negative effects to cell proliferation and growth at concentrations of 5 μg/mL. However, this effect may partly be due to changes to the cell transcriptome induced by presence of SWCNTs. In Chapter 4, I explore the impact of carbon nanotubes on various cell signaling cascades which influence cell division and other cellular functions.

3.5 Interaction of SWCNT Neuro-Sensor with Intracellular Proteins

Incubation of SWCNTs in a protein-rich biological milieu results in formation of the protein corona, a complex and dynamic structure on the surface of the nanoparticle.[28] The composition and morphology of the nanoparticle corona can alter the intended function of the corona-free nanoparticle. Furthermore, corona formation is largely dependent on the both the specific nanoparticle and its biological environment.[60] Therefore, it is vital to characterize the dynamics of protein corona formation on $(GT)_6$-SWCNT neuro-sensors in order to improve probe design. Prior work has focused on the thermodynamic driving forces behind this phenomenon. Herein, we study the makeup of proteins which comprise the protein corona to identify cellular components which are more prone to interaction with carbon nanotube-based probes.

In the context of $(GT)_6$-SWCNT incubation with SIM-A9 microglia in sera-free media conditions, protein adsorption will largely occur intracellularly. We probe this using a modified pull-down assay which recovers adsorbed proteins which then undergo trypsin digestion and identification by quantitative, label-free mass spectrometry.[113] Initial validation of this assay was performed using cell lysate (**Appendix B**). This resulted in a protein corona rich in nuclear and mitochondrial proteins, with the former being highly overrepresented within the subset of proteins with high SWCNT affinity. However, since DNA-SWCNTs are not reported to internalize or interact with these organelles,[106,114] the set of adsorbed proteins from this data was not considered biologically relevant in the context of SIM-A9 microglia interaction. The relatively low number of significantly overrepresented cellular component sets suggests that protein adsorption is largely nonspecific with respect to proteins which comprise different structures within the cell. Therefore, statistical analysis using a smaller list of SWCNT-enriched proteins which come into contact with the SWCNTs throughout their passage through the cell may help identify areas within the cell that SWCNTs localize to. To improve sample collection towards this goal, I perform a modified assay which involves pre-incubation of microglia with $(GT)_6$-SWCNTs for 2 h and 4 h, followed by removal of supernatant and cell lysis. The resulting lysate/SWCNT mixture is centrifuged to pellet agglomerated SWCNTs which were previously internalized within cells. Subsequently, adsorbed protein is desorbed using heat and surfactant treatment. The irreversibility of non-specific protein adsorption to SWCNTs suggests that this methodology will retain the pre-lysis protein corona.[22] These recovered proteins were then trypsin digested and identified using tandem LC-MS/MS (see **3.7 Materials and Methods**).

For cells lysed after 2 h, a total of 468 proteins were identified in lysate of which 375 were found in the SWCNT corona phase at an appreciable concentration. No proteins were enriched above the limit of detection by adsorption to the SWCNT surface. The longer 4 h incubation time resulted in a more diverse protein corona, consisting of 437 proteins out of 477 in cell lysate. Proteins found in the $(GT)_6$-SWCNT corona were ranked by molar abundance. The 25 most abundant proteins at each time point are listed below (**Table 3.1**). These 25 proteins comprise 82.6% and 68.9% of the overall molar composition of the protein corona formed after 2 h and 4 h respectively. Interestingly, the intermediate filament protein vimentin was the most abundant

protein at both time points. Other cytoskeletal proteins such as actin were also highly present at both 2 h (rank 4 and 8) and 4 h (rank 12) post incubation.

Table 3.1 Most abundant proteins in $(GT)_6$-SWCNT corona following internalization in SIM-A9 microglia for 2 h and 4 h

	Protein	
Rank	**2 h**	**4 h**
1	Vimentin	Vimentin
2	Enoyl-CoA delta isomerase 3, peroxisomal	Nucleophosmin
3	Polyadenylate-binding protein 1	Heterogeneous nuclear ribonucleoproteins A2/B1
4	Actin, alpha cardiac muscle 1	Gametocyte-specific factor 1-like
5	Histone H2B type 1-F/J/L	Nucleolin
6	Nucleophosmin	Histone H2B type 1-F/J/L
7	Nucleolin	Heterogeneous nuclear ribonucleoprotein A/B
8	Actin, cytoplasmic 1	Serine/arginine-rich splicing factor 7
9	Tropomyosin alpha-3 chain	Heterogeneous nuclear ribonucleoproteins C1/C2
10	Nucleoside diphosphate kinase A	Heterogeneous nuclear ribonucleoprotein H
11	Centrosomal protein of 162 kDa	Heterogeneous nuclear ribonucleoprotein A0
12	Heterogeneous nuclear ribonucleoprotein L	Actin, alpha cardiac muscle 1
13	Heterogeneous nuclear ribonucleoproteins A2/B1	Heterogeneous nuclear ribonucleoprotein A1
14	Heterogeneous nuclear ribonucleoprotein H	Prelamin-A/C
15	MKI67 FHA domain-interacting nucleolar phosphoprotein	Peripherin
16	Lymphocyte-specific protein 1	Enoyl-CoA delta isomerase 3, peroxisomal
17	Lamin-B1	Lymphocyte-specific protein 1
18	Calmodulin-1	Lamin-B1
19	Myosin-9	Nucleoprotein TPR
20	Histone-binding protein RBBP4	Heterogeneous nuclear ribonucleoprotein L
21	Prelamin-A/C	Coronin-1A
22	Beta-actin-like protein 2	RNA-binding protein FUS
23	Heterogeneous nuclear ribonucleoprotein A3	Histone-binding protein RBBP7
24	Histone-binding protein RBBP7	Heterogeneous nuclear ribonucleoprotein H2
25	Serum albumin	Importin subunit alpha-1

Plotting the abundance of each protein in the corona phase vs. abundance in the lysate control reveals a trend towards protein enrichment, i.e. higher concentration in SWCNT corona than lysate alone (**Figure 3.8a–b**). MS protein results were further ranked using the degree of enrichment or depletion, termed the fold change. This value was defined as the ratio between abundance of a protein in the SWCNT corona to abundance in lysate control. Statistical significance of each protein fold change is also calculated (N = 3, **Figure 3.8c–d**).

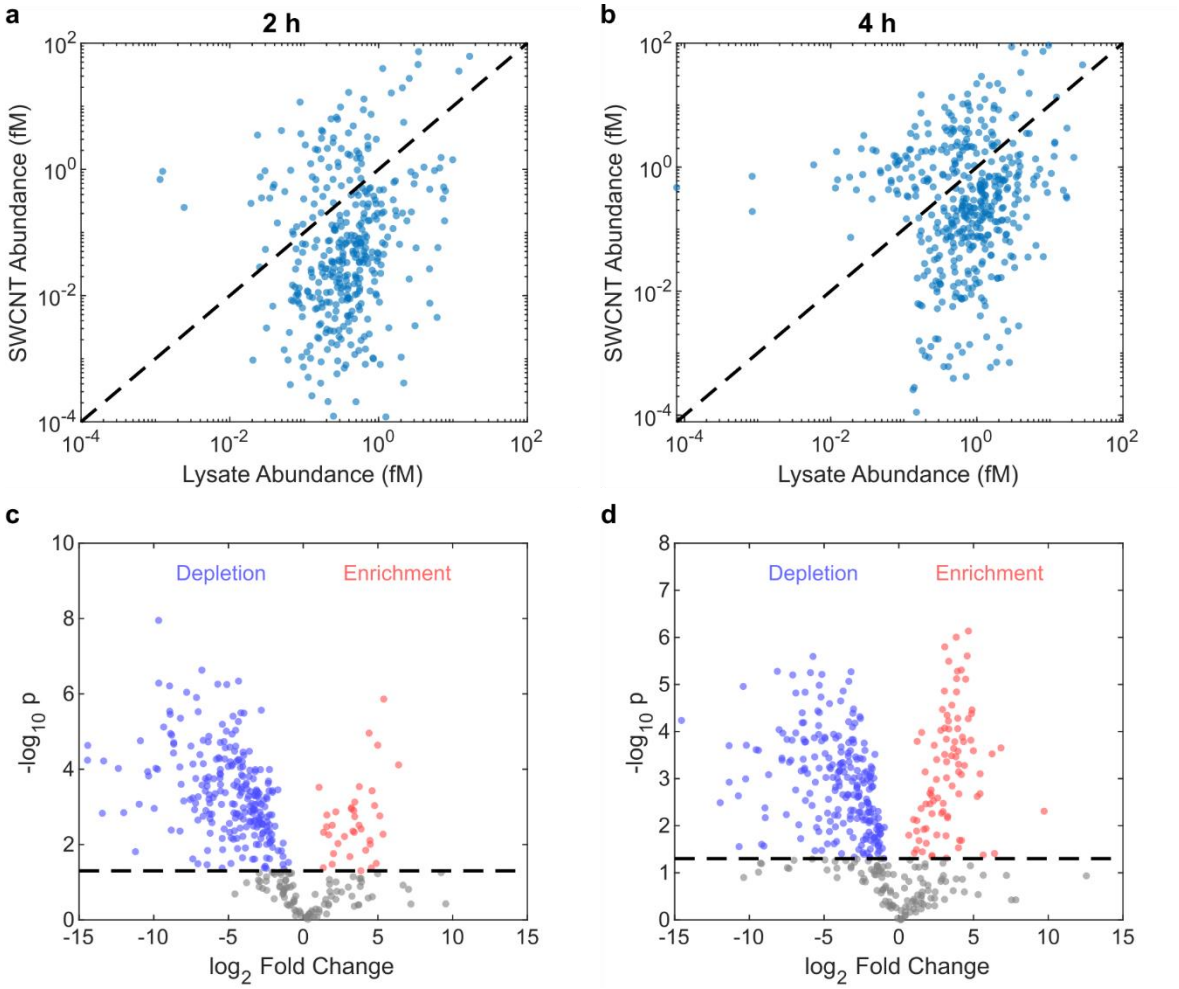

Figure 3.8 Change in protein abundance upon adsorption to SWCNT. (a–b) Relative abundance of protein in $(GT)_6$-SWCNT corona vs. in cell lysate for SWCNT/lysate recovery after **(a)** 2 h and **(b)** 4 h incubation. Each data point represents a unique protein. Protein concentrations in femtomolar are determined from comparison to an internal control with known concentration. Dashed line indicates equal corona and lysate abundance (fold change = 1). **(c–d)** Volcano plots of $\log_2$ fold change in protein concentration from SWCNT corona to lysate only samples with respect to $-\log_{10}$ p value (two-way ANOVA, N = 3). SWCNT corona proteins are collected after **(c)** 2 h and **(d)** 4 h incubation with SIM-A9 cells. Each data point represents a unique protein identified by MS where blue and red markers indicate significantly depleted and enriched proteins respectively. Dashed line equates to p = 0.05.

Generally, enriched proteins (fold change greater than 1) are said to reside in the corona phase.[115] Herein, I consider only proteins with statistically significant enrichment as part of the SWCNT corona (red data points, **Figure 3.8b–c**). To elucidate changes in the protein corona between 2 h and 4 h time points, I apply overrepresentation analysis of Gene Ontology (GO) terms to this subset of proteins. This methodology examines whether certain curated gene sets contain higher than representation from the subset of significantly enriched proteins compared to the list of all proteins identified for a given time point. Fisher's exact algorithm was used to determine overrepresented GO cellular component terms from both 2 h and 4 h data sets. The statistically significant GO terms with greater than 10 annotations are listed below (**Table 3.2**, **Table 3.3**).

Table 3.2 GO Cellular component terms overrepresented by 2 h protein corona

GO ID	Term	Annotated	Significant	Expected	p Value
GO:0016607	Nuclear speck	18	7	1.41	1.7×10^{-4}
GO:0071013	Catalytic step 2 spliceosome	19	6	1.48	0.015
GO:0005654	Nucleoplasm	109	20	8.51	0.039

Table 3.3 GO Cellular component terms overrepresented by 4 h protein corona

GO ID	Term	Annotated	Significant	Expected	p Value
GO:0016363	Nuclear matrix	17	10	3.18	2.0×10^{-4}
GO:0071013	Catalytic step 2 spliceosome	28	14	5.23	5.2×10^{-4}
GO:0005654	Nucleoplasm	144	52	26.9	7.8×10^{-4}
GO:1990904	Ribonucleoprotein complex	146	42	27.28	5.6×10^{-3}
GO:0005694	Chromosome	47	21	8.78	7.9×10^{-3}
GO:0000785	Chromatin	23	12	4.3	0.011
GO:0005903	Brush border	13	6	2.43	0.023
GO:0005681	Spliceosomal complex	41	20	7.66	0.028
GO:0035770	Ribonucleoprotein granule	29	9	5.42	0.033

Similar to results from *in vitro* incubation of $(GT)_6$-SWCNT with SIM-A9 cell lysate (**Appendix B**), the SWCNT corona is highly biased towards proteins present within the cell nucleus at both incubation time points. *Catalytic step 2 spliceosome* and *Nucleoplasm* are consistently among the top three most significantly enriched terms. The 4 h time point shows overrepresentation of more GO terms and a preference for cellular components involved in DNA (*Chromosome*, *Chromatin*) and RNA processing (*Ribonucleoprotein complex*, *Spliceosomal complex*, *Ribonucleoprotein granule*). Since the SWCNT is not thought to interact with the cell nucleus, adsorption of proteins annotated with these terms likely occurred after cell lysis. Therefore, these proteins may exhibit high affinity for the SWCNT soft corona, the outer shell of proteins adsorbed to the inner hard corona proteins.[116] These results in conjunction with protein corona analysis in whole cell lysate indicate that $(GT)_6$-SWCNTs preferentially bind nuclear proteins and structures associated with the cell nucleus. Hence, strong and potentially unfavorable interactions with the cell nucleus may arise between SWCNT neuro-sensors and other cell types or biological systems. Although this sample collection method did not elucidate subcellular localization of $(GT)_6$-SWCNTs, this protocol was capable of discerning distinct differences in protein adsorption at different incubation time points, where 4 h incubation resulted in a more diverse protein corona. Future developments on SWCNT collection method with regards to preservation of the internalized SWCNT protein corona are required in order to better characterize the SWCNT-protein interactions which occur within the cell. Ultimately, this will provide invaluable insights into the pathway SWCNTs follow in their traversal of the intracellular landscape.

3.6 Conclusions

Biological applications using SWCNT neuro-sensor—including incorporation of $(GT)_6$-SWCNT into mouse brain tissue—typically utilize average concentrations of 2 μg/mL.[1] However, interaction of these sensors with the protein-rich brain extracellular space likely results in areas with higher local concentrations. As such, assaying the concentration dependent response of microglial cells to these neuro-sensors is vital in understanding the full range of consequential effects that may arise throughout the brain tissue.

The presence of SWCNTs in a microglial cell culture resulted significant and immediate negative responses including induction of cell ramification, toxicity, and internalization within cells. SIM-A9 cell morphology and phagocytic ability were most sensitive to SWCNT. Concentrations of $(GT)_6$-SWCNT as low as 0.5 μg/mL caused cells to develop elongated processes and significantly decreased cellular uptake of zymosan particles. Reduction of cell proliferation begin to present at SWCNT concentrations approximately equal to 1 μg/mL. Finally, membrane impermeant dye propidium iodide revealed cytoxicity at $(GT)_6$-SWCNT concentrations greater than 5 μg/mL. Although it is unknown how these concentrations established in tissue cultures translate *in vivo,* it is prudent to expect all of these effects to result from SWCNT catecholamine sensor during brain slice imaging. In the next chapter, I use high-throughput mRNA sequencing to explore the full transcriptomic response of SIM-A9 microglial cells to SWCNT neuro-sensors. This broad look at the biological impact of these nanomaterials reveals more subtle effects induced by SWCNT activation of signaling cascades which were not immediately apparent through microscopic techniques.

Cell internalization within tissues negatively impacts signaling ability by sequestering sensor away from the extracellular space where neuromodulators are trafficked via vesicular transport. $(GT)_6$-SWCNT internalization in SIM-A9 cells was tracked using SWCNT nIR fluorescence and was found to be energy-dependent and independent of cell morphology. While the exact mechanisms of SWCNT endocytosis have been thoroughly researched in the literature, more work is needed to discover robust methods by which to minimize this effect.

Finally, we performed proof of concept experiments to explore the relation between these cellular responses and the many SWCNT-protein interactions that may occur within the cell. Although current sample collection and quantification was limited in sensitivity, proteomic analysis revealed a strong inclination for SWCNTs to adsorb nuclear proteins, in particular proteins found in the nucleolus. Although $(GT)_6$-SWCNTs likely do not encounter these proteins during their canonical internalization pathway, these interactions may be consequential for SWCNT constructs designed for targeted nuclear delivery.[106]

3.7 Materials and Methods

Cell culture

Cyropreserved SIM-A9 cells were obtained from the UCB Cell Culture Facility and plated on a 75-cm^2 culture flask in 10 mL of DMEM/F12 growth media supplemented with 10% fetal bovine serum, 5% horse serum, and 1x pen-strep-glutamine (Gibco, Life Technologies). All sera obtained were heat inactivated. Cells were stored in a humidified incubator at 37°C and 5% CO_2. Cells were subcultured every 2-3 days after reaching approximately 90% confluence. Experiments were conducted using cells under passage number 15.

Live-cell imaging

Cells were plated in a 96-well plate at a density of 50,000 cells per well in 100 µL of growth media. Cells were maintained at 37°C and 5% CO_2 until approximately 70% confluent then washed with PBS. Media was replaced with sera free DMEM/F12 for two hours prior to start of experiments. Stock SWCNT or LPS was added to each well at 10x concentration, 0.1x total volume. Three biological replicates were run for each treatment. Phase contrast images were taken at 30-minute intervals using an IncuCyte® Live-Cell Analysis System (Sartorius) in a humidified incubator at 37°C and 5% CO_2. Images were analyzed using MATLAB (MathWorks) to identify and threshold cells for quantitation of cell area and perimeter.

Confocal imaging of F-actin and DAPI stains

Cells were plated on poly-D lysine coated coverslips immersed in growth media in 6-well plates. Cells were treated with samples as previously described. Following treatment, cells were washed with PBS and fixed using 4% paraformaldehyde for 30 min at room temperature. Coverslips with fixed adherent cells were washed three times with PBS and submerged in 1 mL PBS. Two drops of ActinGreen 488 ReadyProbes Reagent (Thermo Fisher) were added and DAPI counterstain was added to a final concentration of 1 µg/mL. Cells were incubated for 1 h covered, at room temperature. The coverslip was rinsed three times and mounted in PBS on a glass microscope slide. Stained cells were imaged with a Zeiss LSM 710 laser scanning confocal microscope using DAPI and FAM fluorescence channels.

SWCNT internalization into SIM-A9

Cells were plated in 35mm dishes at a density of 0.15 x 10^6 cells per well in growth media and incubated overnight. Cells were serum starved for two hours prior to imaging. Concentrated $(GT)_6$-SWCNTs in PBS was added to a final concentration of 5 µg/mL. Following incubation under specified conditions, media was removed and cells were washed with PBS and subsequently fixed with 4% PFA incubation for 20 min at room temperature. Fixed cells were washed with PBS twice then stained with ActinGreen 488 (Invitrogen) for 30 min at room temperature. Cells were washed with PBS before imaging on a Zeiss upright microscope (Axio Observer.D1) with a 10x objective. A 721 nm laser was used for excitation and signal was collected with a Ninox 640 InGaAs camera (Raptor Photonics). Brightfield images were collected using the same camera with LED illumination. Green fluorescence images were collected using LED illumination and a FITC filter set (Chroma). Images were analyzed using MATLAB. FITC fluorescence images were used to identify cells and compute corresponding form factor values. SWCNT fluorescence for each cell was computed using the mean nIR fluorescence from within the cell boundary established from green fluorescence images.

Phagocytosis assay

SIM-A9 microglia were plated on a 96 well plate at a density of 10,000 cells per well. After overnight incubation in a humidified incubator at 37°C and 5% CO_2 media was replaced with 90 μL sera free DMEM/F12 and incubated for an additional 4 hours. A 10 μL aliquot of sample at 10x concentration (LPS, $(GT)_6$-SWCNT, COOH-SWCNT or PBS control) was added to each corresponding well. Following 3 h incubation at 37°C and 5% CO_2, a 5 μL aliquot of 1 mg/mL pHrodo red (Sartorius) was added to each well. The 96 well plate was imaged in an IncuCyte® Live-Cell Analysis System (Sartorius) using the phase contrast and red fluorescence channels at 1 h intervals. Mean fluorescence per cell area was computed using the IncuCyte Base Analysis software.

Flow cytometry viability assays

SIM-A9 cells were cultured in 24-well plates until approximately 70% confluence (~0.2 x 10^6 cells per well). Cells were detached from the well plate surface by removing supernatant, washing cells with PBS, and adding 1 mL of 0.05% trypsin-EDTA (Thermo Fisher) and incubating for 2 min. Tryspin was deactivated by adding 2 mL of growth media (DMEM/F12 containing 10% FBS and 5% horse serum). Cell mixture was centrifuged at 500 rcf for 5 min to pellet cells. Supernatant was discarded and cell pellet was washed with PBS. This washing process was repeated 2 times and cells were resuspended in 0.5 mL ice cold PBS. Cells were stained using the Dead Cell Apoptosis Kit with Annexin V FITC and propidium iodide (Thermo Fisher) following manufacturer protocols. A 200 μL volume of the resulting cell suspension was fed into a 2020 Attune NxT Flow Cytometer (Thermo Fisher) and signal was collected from forward/side scatter channels and blue and yellow fluorescence channels.

Protein mass spectrometry

Protein corona composition was characterized by proteomic mass spectrometry as described previously.[113] Briefly, $(GT)_6$-SWCNT (5 μg/mL final concentration) or PBS was added to SIM-A9 cells cultured in a 6-well plate (approximately 1 x 10^6 cells per well) in sera free media for 2 or 4 hours at 37°C, 5% CO_2. Each condition (SWCNT or PBS) at each time point (2 or 4 h) was run in triplicate. After incubation was complete, supernatant was removed and cells were washed three times with 0.1 M PBS. Adherent cells were lysed using 500 μL of ice-cold Native lysis buffer (Abcam). Biofluid only control (i.e. SIM-A9 cell lysate) was prepared using the same protocol with cells in the absence of SWCNTs. The ratio of protein concentration to nanoparticle surface area was maintained constant based on prior optimization, with 200 g L^{-1} protein per m^2 nanoparticle surface area. Nanoparticles with adsorbed proteins were pelleted by centrifugation (16.1 krcf, 20 min). Supernatant with unbound proteins was removed, the pellet resuspended in 0.1 M PBS to the original volume, and the pellet broken up by pipetting. Washing was repeated three times for complete removal of unbound proteins. Bound proteins were eluted from nanoparticles by heating for 60 min at 37°C in urea/DTT reducing buffer (8 M urea, 5 mM DTT, 50 mM Tris-HCl, pH 8). Eluted protein content was determined with the EZQ Protein Quantitation Kit (Thermo Fisher Scientific). The solution was centrifuged to remove the majority of nanoparticles (16.1 krcf, 20 min) and this supernatant was spin-filtered to concentrate and remove impurities (14 krcf, 30 min; Amicon Ultra-0.5 mL centrifugal filters with 3 kDa MWCO, Millipore Sigma; pre-rinsed). Proteins were alkylated for 30 min in the dark with 15 mM iodoacetamide. The reaction was quenched for 20 min with 500 mM DTT in a volume ratio of 3:1 to

iodoacetamide, then diluted 1:1 with 50 mM Tris-HCl pH 8. In-solution protein digestion was done overnight at 37°C, with a ratio of 1:25 w/w Trypsin/Lys-C (Mass Spectrometry Grade, Promega) to protein. Any residual nanoparticles were removed by spin filtering (14 krcf, 30 min; Amicon Ultra-0.5 mL centrifugal filters with 30 kDa MWCO, Millipore Sigma; pre-rinsed). Peptide content was determined with the Pierce Peptide Quantitation Kit (Thermo Fisher Scientific) and samples were normalized to 0.1 g L-1 in 100 µL volume. Solutions were spiked with 50 fmol of E. coli housekeeping peptide (Hi3 Ecoli Standard, Waters) per 5 µL volume for protein quantification. Digestion was terminated by freezing at -20°C. Biofluid-alone samples underwent identical processing steps, from denaturation to tryspin digestion.

Peptides were analyzed using a Synapt G2-Si mass spectrometer equipped with a nanoelectrospray ionization source and connected in line with an Acquity M-class ultra-performance liquid chromatography system (UPLC; Waters, Milford, MA). This instrumentation available as part of the California Institute for Quantitative Biosciences (QB3)/College of Chemistry Mass Spectrometry Facility at UC Berkeley. Data-independent, ion mobility-enabled mass spectra and tandem mass spectra[117–119] were obtained in the positive ion mode. Data acquisition was done with MassLynx software (version 4.1) and tryptic peptide identification and quantification with a label-free approach[120–122] were performed in Progenesis QI for Proteomics software (version 4.0, Waters). Protein accession numbers were annotated using UniProt and Panther databases.

3.8 Supporting Information

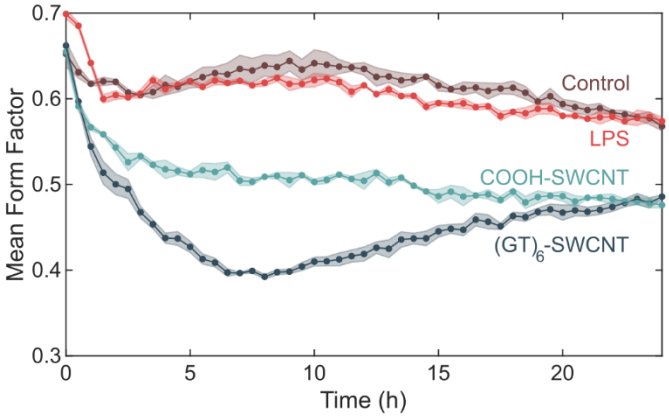

Figure S3.1 Microglial morphology change induced by LPS and SWCNT at the same mass concentration. Mean form factor of SIM-A9 cells incubated with 5 µg/mL LPS, COOH-SWCNT, and $(GT)_6$-SWCNT. SIM-A9 cells were at 37°C and 5% CO_2, in sera free media. Shaded regions represent standard error of the mean (N = 3).

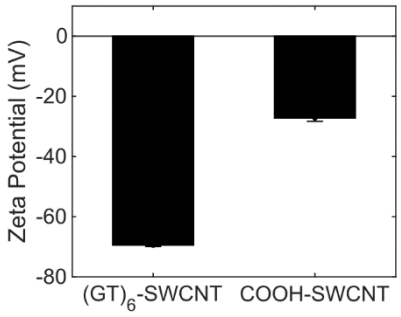

Figure S3.2 Zeta potential measurements of carbon nanotube suspensions. Zeta potentiometer measurements of 5 µg/mL (GT)6-SWCNT and COOH-SWCNT in water collected on a Zetasizer Nano ZS (Malvern).

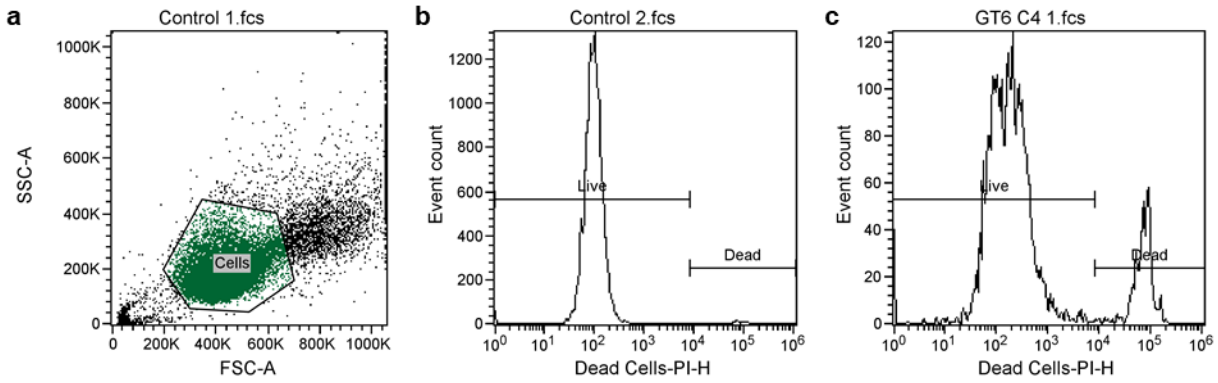

Figure S3.3 Live/dead cell flow cytometry staining. (a) Scatter dot plot of control SIM-A9 cells. Gate was applied to exclude cell debris and doublets. **(b–c)** Log histogram of propidium iodide fluorescence. Gates for live and dead cells are shown.

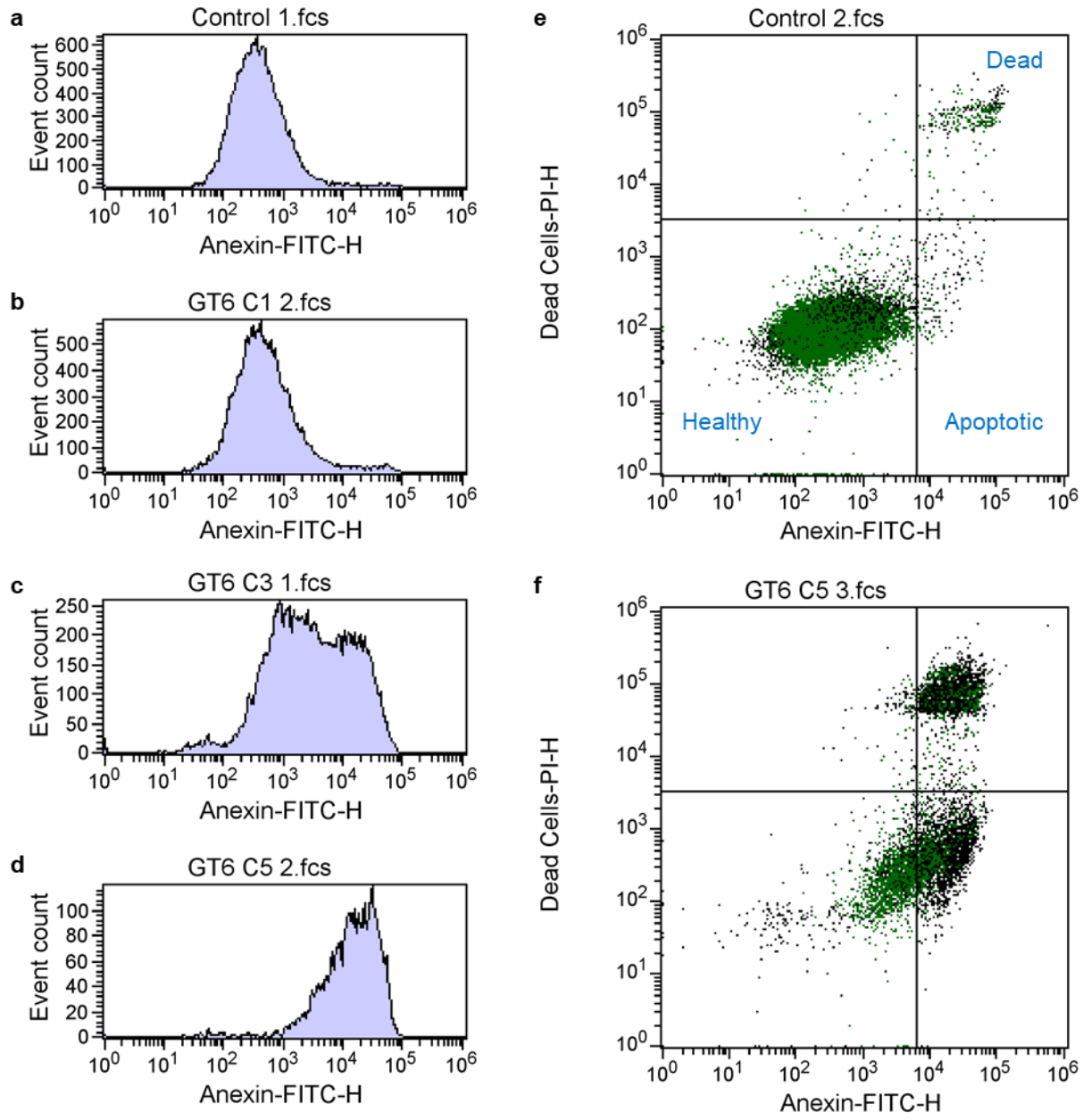

Figure S3.4 Flow cytometry apoptosis staining. (a–d) Histogram of Annexin-FITC stained SIM-A9 cells following incubation with **(a)** 0, **(b)** 1, **(c)** 10, and **(d)** 40 μg/mL $(GT)_6$-SWCNT for 2 h. **(e–f)** Dot plot showing Annexin-FITC vs. propidium iodide stained SIM-A9 with **(e)** 0 and **(f)** 40 μg/mL $(GT)_6$-SWCNT incubation for 2 h prior to detachment by trypsin and staining. Each point refers to a single gated event corresponding to singlet cells. Gates are drawn for live (bottom left), apoptotic (bottom right), and dead cells (top right).

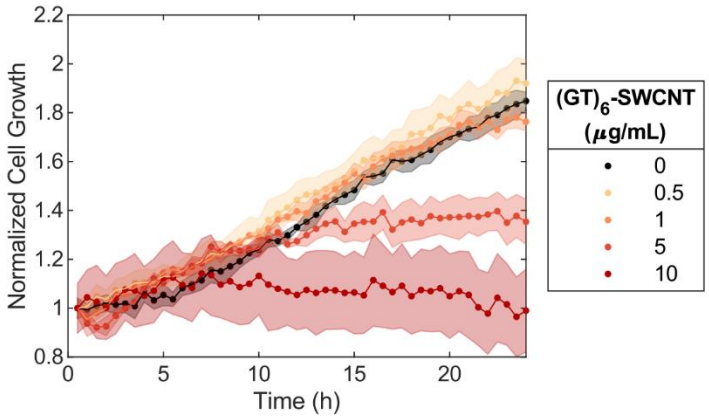

Figure S3.5 SWCNT concentration dependent microglial cell proliferation. Effect of $(GT)_6$-SWCNT of concentration ranging from 0.5 to 10 μg/mL on the replication of SIM-A9 microglial cells. Cell count per field of view acquisition is normalized to initial cell count due to heterogeneity in cell across biological replicates. Shaded region represents standard error of the mean (N = 3).

Chapter 4:
Transcriptomic Response of Microglia to Neuro-Probes

Portions of this chapter are reproduced and adapted with permission from Ref 23. Copyright 2020 American Chemical Society.

4.1 Introduction

The advent of high-throughput sequencing has enabled extensive developments in the study of cell transcriptomics. RNA-sequencing allows for the quantification of gene expression with high accuracy and precision. This method begins with the isolation and sequencing of mRNA extracted from tissues which have undergone different treatments or conditions. Comparing counts of each gene across various treatment conditions determines differential gene expression. Cell-wide effects can be assessed through further statistical analysis of gene expression data using bioinformatics databases such as the Gene Ontology (GO) project which comprise a hierarchy of terms corresponding to different cellular processes which are used to annotate genes. Although transcriptomics analysis does not probe differences in protein expression or posttranslational effects, it can provide important insights into phenotypes which emerge from biotic or abiotic stresses. In this chapter, we utilize these methodologies as an assessment of nanomaterial toxicology. In recent years, RNA-seq has been applied to study the biological impact of novel bionanotechnologies, particularly those with artificial surface chemistries including titanium and silver nanoparticles.[123,124] The latter were found to induce fibrosis and possible carcinogenicity in cultured lung epithelial cells. We use RNA-seq to study the toxicological impact of SWCNTs on microglial cells.

One example of the ways in which carbon nanotubes affect immune cells in general is the direct activation of cell membrane receptor proteins by carboxylic functionalized multiwalled carbon nanotubes (MWCNT). In this case, these MWCNTs interacted with TLR2/4 on the macrophage cell membrane to induce upregulation of the pro-inflammatory NF-κB signaling cascade.[100] While this entails the activation of only a receptor-mediated signaling pathway, the subsequent overexpression and secretion of cytokines such as interleukin 1β (*Il1b*) then propagate the inflammatory response to surrounding tissue. Due to the broad range of interactions between proteins of various functions and the SWCNT surface, it is necessary to perform a broader screen of cellular mechanisms which may be affected by SWCNTs. Hence, we use bulk RNA-seq experiments to measure the transcriptomic response of SIM-A9 microglial to SWCNTs. We quantify these effects at two relatively quick incubation times to capture the immediate, first order signaling pathways activated. Subsequently, we compare the perturbation in gene expression by SWCNTs to control samples including a strong inflammatory stimulant as well as commonly used molecular neuroscience tools.

4.2 Time-Dependent Transcriptomic Response to SWCNTs

Since the time dependence of microglial activation by SWCNTs is not well studied, it was first necessary to probe the microglial transcriptomic response at multiple time points. In order to capture the initial response to SWCNTs rather than downstream signaling cascades, I extracted RNA from cells following treatment for 0.5 and 2 h. Untreated control cell RNA was compared to those treated with (1) LPS, (2) $(GT)_6$-SWCNT, and (3) COOH-SWCNT. Carboxylated SWCNT was included to compare results of this study to prior studies in the literature which were predominantly focused on covalently modified carbon nanotubes.[100,125]

Extracted total RNA was prepared into mRNA sequencing libraries and high-throughput sequencing was performed for all treatments with three biological replicates each. Raw reads were aligned and counted using *STAR* aligner. Gene counts for each sequencing library were normalized using *limma-voom*[126] and multidimensional scaling (MDS) analysis was performed. MDS plots reveal close clustering of LPS treated microglia with untreated samples at 0.5 h but significant deviation at 2 h **(Figure 4.1a**). Contrarily, SWCNT treated samples deviated more significantly at 0.5 h than at 2 h compared to LPS treatment. This may suggest earlier microglial activation by SWCNTs, a surprising result given the high affinity of the LPS-TLR4 interaction.[127] Similar results are observed for differentially expressed genes, which were identified using the *edgeR* package (**Figure 4.1b–d**).[128,129]

LPS caused no appreciable differential gene expression at 0.5 h, but induced differential expression in 2862 genes at the 2 h time point (**Table 4.1**). On the other hand, (GT)6-SWCNT and COOH-SWCNT samples induced differential expression in 1688 and 485 genes respectively after only 0.5 h and 1625 and 3229 genes after 2 h. However, the magnitude of differential gene expression was significantly larger at the latter time point for LPS treatment for which 261 differentially expressed genes exhibited greater than a 2-fold change in expression compared to only 30 for $(GT)_6$-SWCNT treatment and 49 for COOH-SWCNT. The inflammation marker *Cxcl2* exhibited 73.8-fold increase in response to LPS compared to 2.5- and 1.5-fold increases caused by $(GT)_6$-SWCNT and COOH SWCNT. This points to the more prominent activation of inflammatory signaling cascades caused by the specific LPS-TLR4 ligand receptor binding compared to SWCNT receptor activation which is largely mediated by non-specific protein interactions.[100]

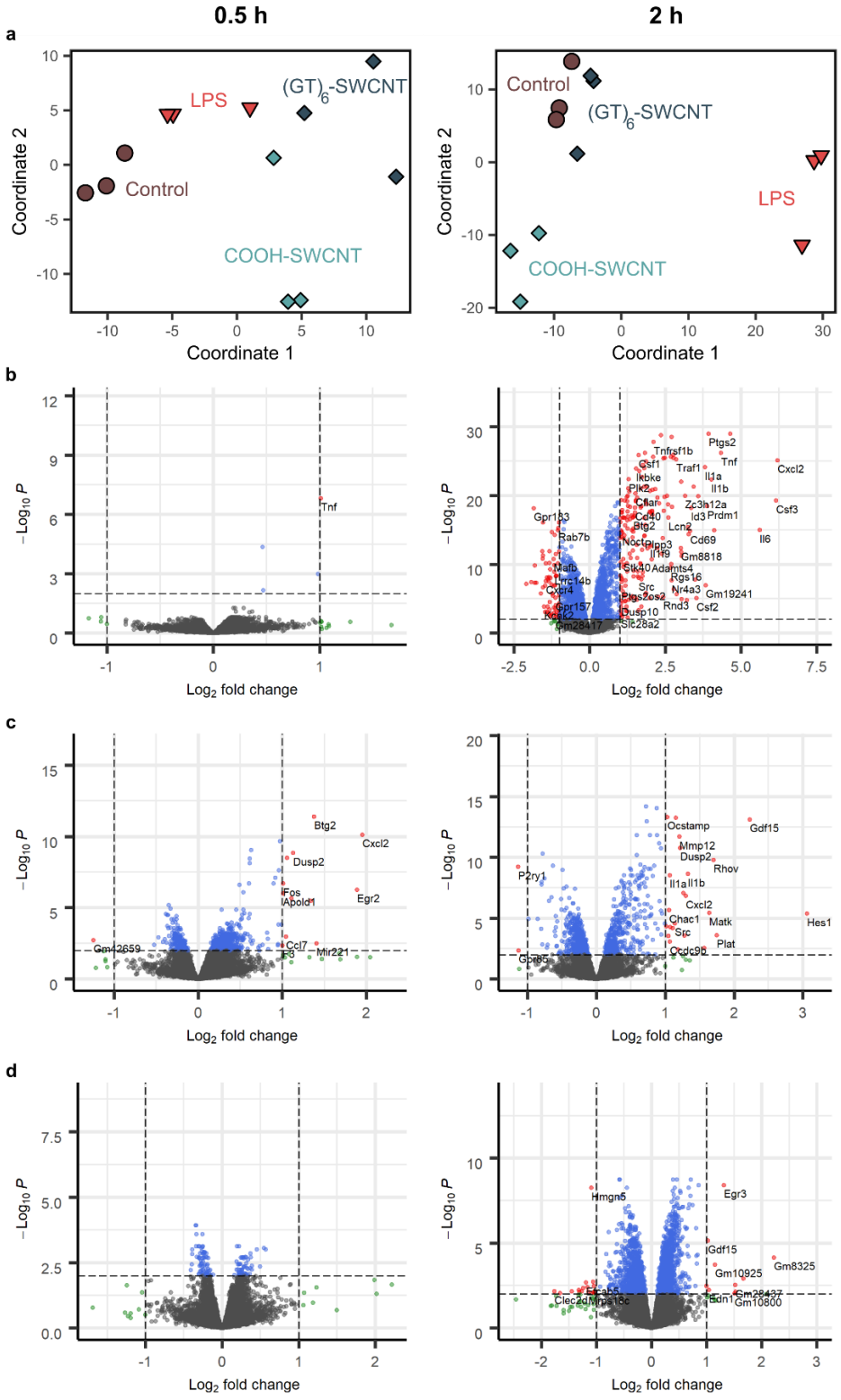

Figure 4.1 Time-dependent transcriptomic response of microglia to SWCNTs and LPS. (a) Multidimensional scaling (MDS) analysis of gene counts tables for LPS, $(GT)_6$-SWCNT, and COOH-SWCNT treated SIM-A9 cells at 0.5 and 2 h time points. **(b–d)** Volcano plots of $\log_2$ expression fold change vs. $\log_{10}$ p_{adj} of 10,402 identified genes for **(b)** LPS, **(c)** $(GT)_6$-SWCNT, and **(d)** COOH-SWCNT treatments. Horizontal and vertical dashed lines delineate $p_{adj} = 0.05$ and $\log_2$ fold change = 1 respectively. Blue and red points identify differentially expressed genes.

Table 4.1 Summary of differentially expressed genes identified in LPS, $(GT)_6$-SWCNT, and COOH-SWCNT stimulated microglia vs. untreated control cells at 0.5 and 2 h time points.

		LPS vs. Control			**$(GT)_6$-SWCNT vs. Control**			**COOH-SWCNT vs. Control**		
		Up	Down	Total	Up	Down	Total	Up	Down	Total
$p_{adj} < 0.05$	0.5 h	4	0	4	1137	551	1688	271	214	485
	2 h	1424	1438	2862	721	904	1625	1622	1607	3229
$\log_2$ Fold Change > 1	0.5 h	1	0	1	21	3	24	5	2	7
	2 h	191	70	261	27	3	30	16	33	49

Next, I examined cellular processes which may be represented within the list of differentially expressed genes for each treatment. The *topGO* R package was used to perform overrepresentation analysis on differentially expressed genes with a cutoff of $p_{adj} < 0.01$.[130,131] Specifically, we examined overrepresentation of Gene Ontology (GO) biological processes terms by differentially expressed genes in SWCNT treated SIM-A9 sequencing libraries. This analysis method identifies GO terms which contain a significantly higher than random fraction of differentially expressed genes for each of our Treatment vs. Untreated Control comparisons. GO terms with 10 or fewer total annotated genes were excluded from analysis. At 0.5 h, the most overrepresented GO term by $(GT)_6$-SWCNT treated SIM-A9 cells was *Positive regulation of endothelial cell proliferation* (**Figure 4.2a**). This may reflect previously observed decrease in cell proliferation upon incubation with SWCNTs (see **3.4 SWCNT Induced Cytotoxicity**). Several receptor-mediate signaling pathways showed possible activation evidenced by presence of terms such as *Cellular response to leukemia inhibitory factor*, *Positive regulation of protein kinase B signaling*, and *cellular response to fibroblast growth factor stimulus* within the top 12 most overrepresented GO terms. Enrichment of the *Regulation of cilium assembly* term may be linked to the actin cytoskeleton growth observed (see **3.2 Cell Morphological Response**). COOH-SWCNT treated SIM-A9 cell sequencing libraries showed overrepresentation of RNA processing terms including several related to the spliceosome among differentially expressed genes at 0.5 h (**Figure 4.2a–b**). GO biological processes linked to these effects include the two most significant terms *Regulation of mRNA processing* and *Regulation of alternative mRNA splicing, via spliceosome*. These results provide hints on which internal cellular processes may be significantly impacted by SWCNTs. Furthermore, these responses are unlikely to be due to TLR4 activation by SWCNTs as LPS which exhibits extremely strong ligand-receptor binding with TLR4 did not induce an appreciable transcriptomic response. However, further work is needed to determine the SWCNT-receptor interactions which initiate these events which manifest after only 0.5 h incubation.

Figure 4.2 Gene ontology enrichment of SWCNT treated microglia at 0.5 hours. (a–b) Top twelve most highly enriched gene ontology terms for RNA-seq libraries generated from **(a)** $(GT)_6$-SWCNT and **(b)** COOH-SWCNT treated microglial cells.

Overrepresentation analysis at the 2 h time point showed more clear activation of immune cell signaling. $(GT)_6$-SWCNT libraries were enriched with terms such as *Cellular response to lipopolysaccharide*, *Positive regulation of NF-κB transcription factor activity*, and *Inflammatory response* (**Figure 4.3a**). As expected, these terms are also statistically significantly enriched by LPS treated SIM-A9 cell libraries which likely points to previously reported TLR2/4 activation by the SWCNTs (**Figure S4.1**). COOH-SWCNT again was associated with significant differential expression of genes annotated with RNA processing terms (**Figure 4.3b**). The second most overrepresented pathway was *Positive regulation of cell proliferation*, which further suggests a cell signaling cause to the decrease in cell replication observed upon exposure of SIM-A9 cells to SWCNTs.

Figure 4.3 Gene ontology enrichment of SWCNT treated microglia at 2 hours. (a–b) Top twelve most highly enriched gene ontology terms for RNA-seq libraries generated from **(a)** $(GT)_6$-SWCNT and **(b)** COOH-SWCNT treated microglial cells.

4.3 RNA-seq Screen of Neuro-Probes and Tools

We further utilized high throughput mRNA sequencing to determine and quantify the full transcriptomic response of SIM-A9 microglia cells to an array of neuro-probes and molecular neuroscience tools. This screen focused on the comparison between exposure to 10 µg/mL $(GT)_6$-SWCNT versus commonly used probes for neuronal signaling including those for calcium imaging (2 µM Fura-2), voltage sensing (2 µM $DiSBAC_2(3)$ and Di-2-ANEPEQ), and AAV viral vector (50,000 virus molecules per SIM-A9 cell). We again compared these responses to those induced by 10 µg/mL COOH-SWCNT and 10 ng/mL LPS positive control. Concentrations of these molecular probes were chosen to be reflective of their working concentrations for brain imaging applications. We assay the SIM-A9 cell transcriptome after 2 h incubation with each probe in sera free media due to the large degree of microglial activation observed in LPS treated samples at this time point. The non-SWCNT neuro-probes screened did not induce a noticeable morphology change in either SIM-A9 microglia (**Figure S4.2**) or cell proliferation rate (**Figure S4.3**) within 24 h of exposure. Furthermore, multidimensional scaling (MDS) analysis of the normalized gene counts for each sequencing library revealed close clustering of biological replicates of Fura-2, $DiSBAC_2(3)$, and Di-2-ANEPEQ with the untreated microglia control (**Figure 4.4a**), suggesting these small molecule neuro-probes have a minor impact on microglial cell function over 2 h. AAV

sequencing libraries also did not show significant divergence from control at the 2 h time point. However, MDS analysis showed deviation of SWCNT and LPS incubated cell samples from the untreated SIM-A9 control. Hierarchical clustering of sequencing libraries further demonstrated that cells incubated with Fura-2, $DiSBAC_2(3)$, Di-ANEPEQ, and AAV did not elicit a significant transcriptomic response, evidenced by the statistical similarity of these sequencing libraries to untreated control libraries (**Figure 4.4b**). Hence, downstream differential gene expression analysis and ontological analysis was only carried out at a dendrogram cut height of 30, comparing SIM-A9 cells treated with $(GT)_6$-SWCNTs, COOH-SWCNTs, and LPS to untreated control groups.

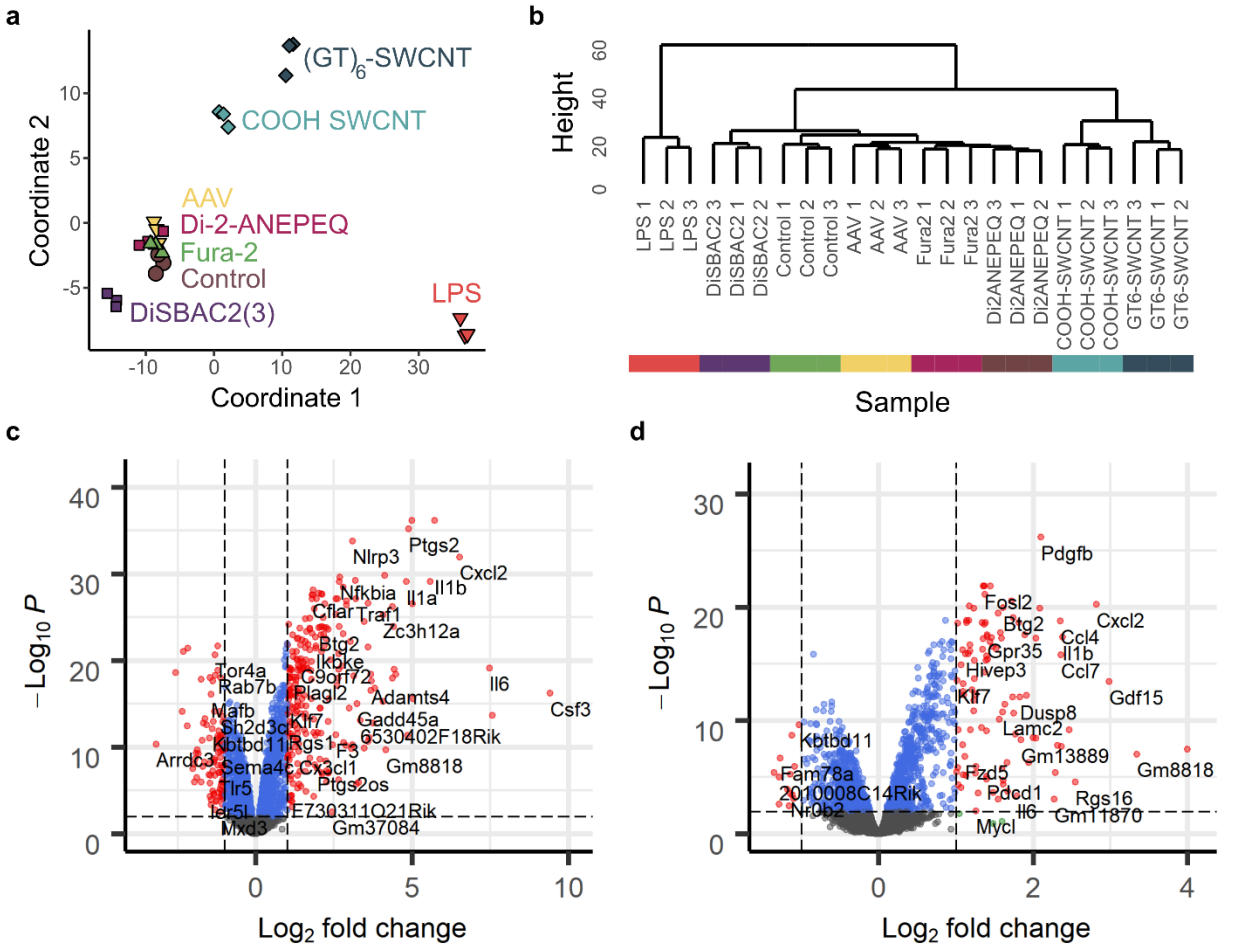

Figure 4.4. Transcriptomic response of SIM-A9 microglia to neuro-probes. **(a)** MDS plots of gene count tables generated for each RNA-seq library, where each marker represents a biological replicate. Axes represent the two principal components of highest variance. Control represents untreated SIM-A9 microglial cells. **(b)** Hierarchical clustering of sequenced libraries based on normalized gene counts. **(c–d)** Volcano plots of **(c)** LPS and **(d)** $(GT)_6$-SWCNT incubated SIM-A9 cells showing $\log_2$ fold change in gene expression vs. $\log_{10}$ adjusted p value for all 9770 identified genes, relative to untreated control cells. Horizontal and vertical dashed lines delineate $p_{adj} = 0.05$ and $\log_2$ fold change = 1 respectively.

We performed differential gene expression analysis using the *edgeR* package.[128] SIM-A9 cell experimental groups were compared pairwise to untreated control groups. For LPS-treated

samples, out of 9770 genes identified across all sequencing libraries, 332 were both differentially expressed ($p_{adj} < 0.05$) and exhibited a greater than 2-fold change in expression vs. the untreated control (**Table 4.2, Figure 4.4c**), where p_{adj} is the false discovery rate corrected p value. Only 119 such genes were identified for $(GT)_6$-SWCNT vs. the untreated control, and 49 genes for COOH-SWCNT vs. untreated control. LPS promoted upregulation of many inflammatory cytokines such as *Csf2*, *Csf3*, *Il1b*, and *Cxcl2* (**Figure 4.4c**), where the latter two cytokines are also among the most highly upregulated genes by $(GT)_6$-SWCNTs (**Figure 4.4d**). However, the SWCNT-induced expression-fold change for these genes was significantly lower than that caused by LPS. Conversely, platelet-derived growth factor subunit B, *Pdgfb*, was more significantly upregulated by $(GT)_6$-SWCNTs than by LPS, and also shows highly statistically significant upregulation by COOH-SWCNTs (**Figure S4.4a**), thus is a potential biomarker for cellular response to SWCNT graphene lattice.

Table 4.2 Summary of differentially expressed genes identified in LPS, $(GT)_6$-SWCNT, and COOH-SWCNT stimulated microglia vs. untreated control cells.

		LPS vs. Control			**$(GT)_6$-SWCNT vs. Control**			**COOH-SWCNT vs. Control**		
		Up	Down	Total	Up	Down	Total	Up	Down	Total
DE Genes	$p_{adj} < 0.05$	1558	1706	3264	1204	1242	2446	1107	1346	2453
	$\log_2$ Fold Change > 1	239	93	332	105	14	119	49	0	49
Gene Type	Protein Coding	1481	1663	3144	1149	1218	2367	1066	1278	2344
	Long noncoding RNA	50	34	84	37	16	53	24	37	61
	Pseudogene	15	4	19	14	5	19	9	26	35

Again, the *topGO* R package was used to perform overrepresentation analysis on GO biological processes terms using differentially expressed genes with a cutoff of $p_{adj} < 0.01$ (see **4.2 Time-Dependent Transcriptomic Response to SWCNTs**).[130,131] As expected, differentially expressed genes in LPS vs. untreated control groups showed high overrepresentation of processes associated with toll-like receptor signaling and inflammation, including *Cellular response to lipopolysaccharide* (**Figure 4.5a**). Exposure of SIM-A9 cells to $(GT)_6$-SWCNTs caused enrichment of similar inflammatory GO terms, including the most statistically significantly enriched GO term, *Inflammatory response* (**Figure 4.5b**). Both LPS and $(GT)_6$-SWCNT treatments caused enrichment of *Positive regulation of ERK1 and ERK2 cascade* GO term. Of 97 annotated genes within this GO term, 52 were differentially expressed by LPS treatment out of an expected 24.4, giving a gene set enrichment p value of 3.7×10^{-9}. $(GT)_6$-SWCNT treatment caused differential expression of 41 annotated genes of an expected 16.2, with a corresponding p value of 5.4×10^{-9}. Enrichment of ERK signaling by both LPS and $(GT)_6$-SWCNTs may indicate similar inflammatory signal transduction induced by the two molecules.

Other biological processes overrepresented by exposure of microglia to $(GT)_6$-SWCNT samples include GO terms related to tissue development such as *Branching morphogenesis of an epithelial tube* and *Angiogenesis*, where the nonspecific nature of these processes in relation to microglial cells may suggest noncanonical activation of cellular mechanisms. Lastly, similar to $(GT)_6$-SWCNTs, COOH-SWCNTs promoted enrichment of ERK signaling terms (**Figure S4.4b**),

pointing to the significance of this signaling cascade in SWCNT-induced immune responses. Interestingly, COOH-SWCNTs caused differential expression of a larger number of pseudogenes in SIM-A9 microglia than either LPS or $(GT)_6$-SWCNTs (**Table 4.2**), despite eliciting only a minor morphological change (**Figure 3.1j–k**). This may be due to overrepresentation of GO terms in the set of COOH-SWCNT induced differentially expressed genes, including *Regulation of transcription* (**Figure S4.4b**).

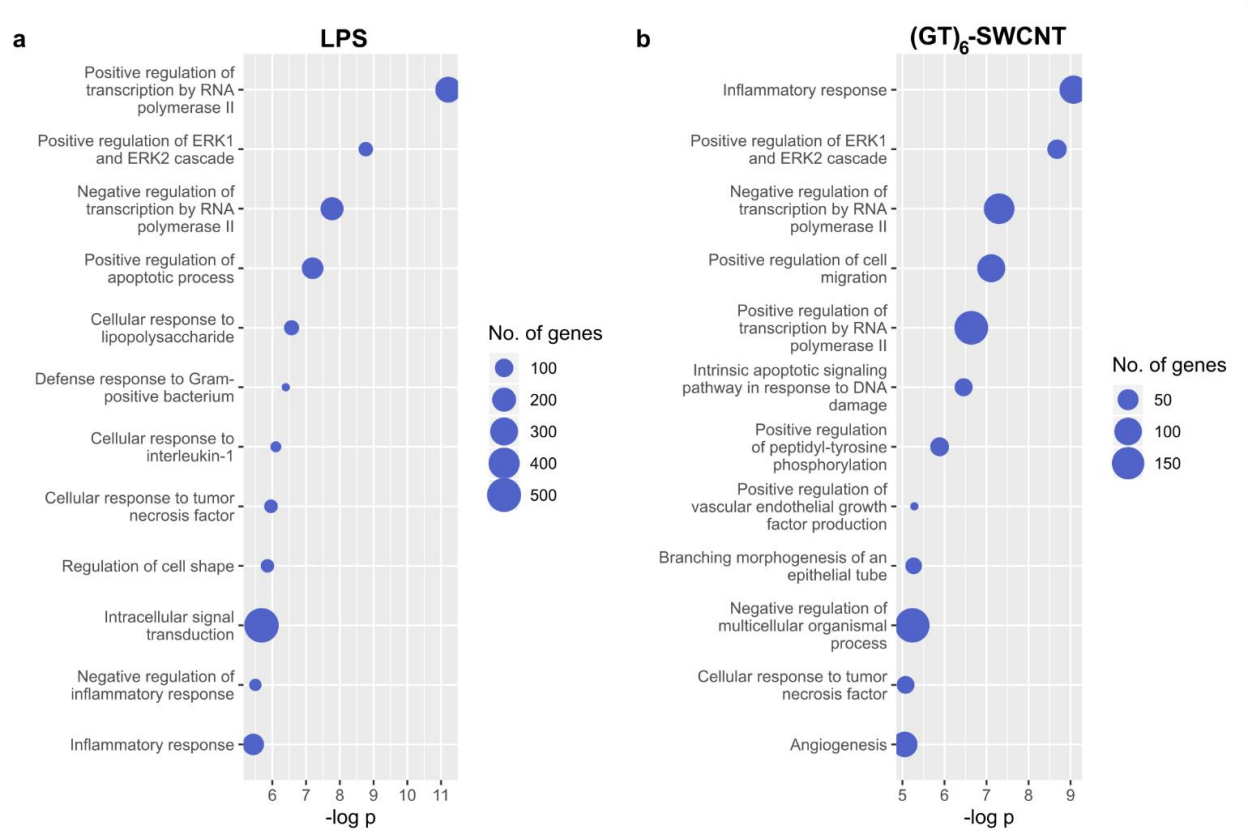

Figure 4.5. Gene Ontology enrichment analysis of LPS and $(GT)_6$-SWCNT treated SIM-A9 microglia. (a–b) Overrepresentation analysis of differentially expressed genes identified in RNA sequencing libraries for SIM-A9 microglia stimulated with **(a)** LPS and **(b)** $(GT)_6$-SWCNT. Top twelve most highly enriched ontologies are displayed.

Finally, gene set enrichment analysis (GSEA) was applied in order to determine the degree to which certain gene sets are up- or downregulated. This analysis method quantifies the degree to which genes involved in certain biological processes are differentially expressed in concert and utilizes expression fold change values to calculate an enrichment score for each gene set.[132] Hallmark gene sets from the Molecular Signatures Database (MSigDB) are curated groups of genes closely tied to specific biological processes and which exhibit low redundancy.[133] All genes from RNA-seq screens were ranked in order of decreasing expression fold change (**Figure S4.5a**). Next, GSEA was applied using Hallmark pathways such as *Apoptosis* and *Interferon Alpha Response* (**Figure S4.5b–c**) where the enrichment score is calculated based on the distribution of annotated genes from a given pathway at the up- and downregulation extremes of the gene expression ranking. Normalized enrichment score accounts for the number of annotated genes

within each Hallmark pathway. The p value for each enrichment score is calculated using Kolmogorov-Smirnov-like statistics.[132] The Hallmark pathway GSEA revealed statistically significant enrichment of 22 pathways by $(GT)_6$-SWCNT treated samples and 16 for LPS treatment out of the 50 total Hallmark gene sets (**Figure 4.6**). The only Hallmark pathway enriched by LPS samples but not $(GT)_6$-SWCNT was *Interferon Gamma Response*.

Conversely, $(GT)_6$-SWCNT treatment caused enrichment of seven pathways not enriched by LPS treatment. These include *Wnt/β-Catenin Signaling*, *Apical Junction*, *Unfolded Protein Response*, and *Coagulation*. The Wnt/β-catenin signaling pathway is a receptor protein mediated signaling cascade which mediates proinflammatory responses in microglia.[134] Activation of the canonical and non-canonical Wnt signaling pathways are also responsible for mediating the polarization of neurons during cortical development.[135] Hence, the SWCNT induced morphology change in SIM-A9 microglia may also be due to SWCNT selective activation of the Wnt/β-catenin signaling pathway. Wnt/β-catenin signaling is mediated by the Frizzled family of membrane proteins. From RNA-seq data, SIM-A9 microglia expressed both *Fzd5* and *Fzd7* genes which encode Frizzled-5 and Frizzled-7 proteins, respectively. Interactions between carbon nanotubes and Frizzled receptors has not previously been reported in the literature. However, knockouts of either of these genes in SIM-A9 cell cultures may reveal whether these interactions do occur or if Wnt signaling is responsible to some degree for the phenotypic changes induced by SWCNT exposure. *Wnt/β-Catenin Signaling* pathway activation may be related to activation of the *Apical Junction* Hallmark pathway. Apical junctions are structures associated with the actin cytoskeleton found at the epithelial cell-cell interface. The protein β-catenin, an important mediator in canonical Wnt signaling, acts as a linker between the apical junction complex and the cell actin cytoskeleton.[136] Hence, the polarization and actin cytoskeleton growth of SIM-A9 cells is likely a contributing factor to or a result of these Hallmark pathways.

Unfolded protein response is a highly conserved mammalian cell pathway commonly caused by damage to the endoplasmic reticulum of the cell. Carbon nanoparticles have previously been shown to induce endoplasmic reticulum stress resulting in accumulation of misfolded proteins in certain tissues including the brain.[137] Again, further work is needed to determine the origin and magnitude of this response. Finally, activation of the Hallmark coagulation pathway may arise from adsorption of complement proteins to the SWCNT surface which has been extensively studied in the literature.[53,113,138] In addition, $(GT)_6$-SWCNT induced differentially expressed genes were negatively enriched for *Interferon Alpha Response*. This may point to downregulation of interferon alpha signaling pathways. Further investigation is required to determine the SWCNT-mediated interaction behind this response.

Carboxylated SWCNT treatment caused enrichment of 29 out of the 50 Hallmark pathways **(Table S4.1**). A few commonalities with $(GT)_6$-SWCNT include positive enrichment scores greater than 2.0 for *TNFα Signaling via NFKB*, *Inflammatory Response*, *Wnt/β-Catenin Signaling*, *Complement*, *Coagulation*, and *Apical Junction*. These indicate a similar pattern recognition receptor mediated inflammatory response to both covalently and noncovalently functionalized SWCNTs suggesting a generic cellular response to the SWCNT graphene lattice. Furthermore, COOH-SWCNT treatment caused negative enrichment of 4 Hallmark pathways: *DNA Repair*, *E2F Targets*, *MYC Targets V1*, and *Oxidative Phosphorylation*. *Interferon Alpha Response* Hallmark pathway was not statistically significantly enriched for these samples. These negatively enriched Hallmark pathways recapitulate the negative regulatory effect of COOH-SWCNT on transcription, translation, and cell metabolism as observed from overrepresentation analysis.

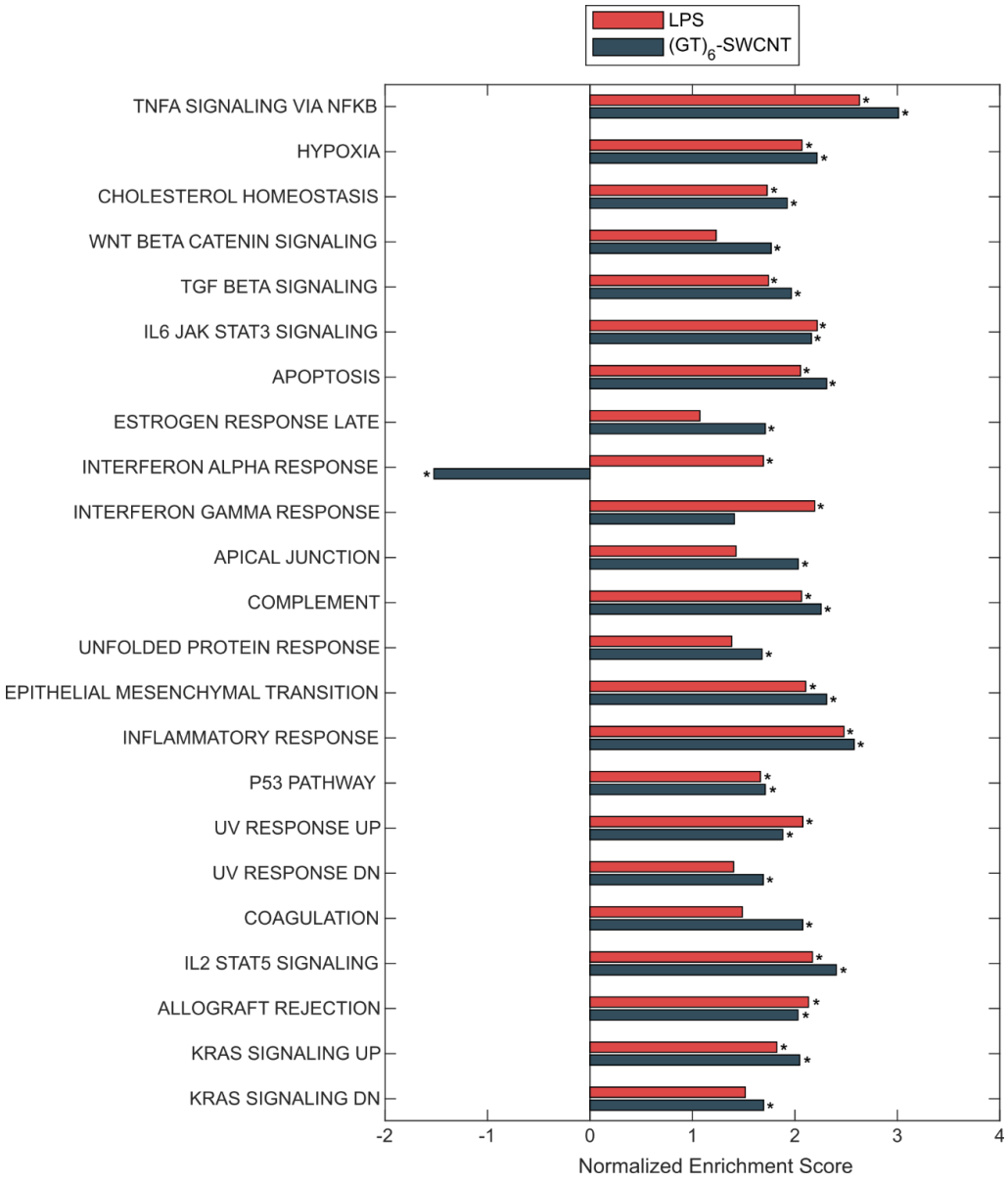

Figure 4.6 Enrichment analysis of Hallmark gene sets. Normalized expression scores calculated from GSEA of SIM-A9 sequencing libraries with LPS and $(GT)_6$-SWCNT treatment. * $p < 0.01$.

4.5 Conclusions

Carbon nanotubes are an artificial nanomaterial with rapidly emerging biological use. As such, the study of biological effect on different cell and tissue types is becoming an urgent matter. The previous chapter examined the phenotypic and cytotoxic effects of single-walled carbon nanotube neuro-sensors on mouse microglial cells in sera free conditions. These experiments probed the potential range of cellular responses to SWCNT presence in cell culture supernatant. Differential gene expression analysis of RNA-seq libraries revealed activation of transcription

induced by SWCNTs after only 0.5 h incubation resulting in differential expression of 1688 genes. LPS failed to stimulate cells at this time point, inducing differential expression in only 4 genes. However, microglial activation by LPS at 2 h was orders of magnitude greater than that by SWCNTs. Other neuro-probes including calcium and voltage sensitive probes and AAV failed to elicit a significant response. Of the DE genes upregulated by SWCNTs, several were identified as potential biomarkers for SWCNT presence in brain tissue. These include genes encoding cytokines (*Cxcl2*, *Il1b*, *Il6*, *Ccl4*, and *Ccl7*) as well as growth factors (*Pdgfb*, *Csf2*, and *Csf3*).

Finally, statistical analysis was leveraged to analyze lists of differentially expressed genes from each treatment sample compared to untreated control. Overrepresentation analysis revealed considerable overlap between Gene Ontology terms associated with $(GT)_6$-SWCNT exposure compared to LPS. This suggests interaction between $(GT)_6$-SWCNT neuro-sensor and TLR2/4, causing activation of NF-κB signal transduction pathway. Gene set enrichment analysis recapitulated activation of inflammatory signaling through positive enrichment of *TNFa Signaling via NFKB* and *Inflammatory Response* Hallmark pathways by both LPS and $(GT)_6$-SWCNT treatments. Additional biological processes impacted by SWCNT presence included activation of the Wnt/β-catenin signaling pathway which may be responsible for the polarization of cell morphology. Future work will investigate whether direct interaction of SWCNT with Frizzled protein receptors is responsible for this effect.

Distinct from $(GT)_6$-SWCNT, COOH-SWCNT caused overrepresentation of GO terms for RNA transcription and processing. These may cause the high differential expression of pseudogenes observed for this treatment, where COOH-SWCNT incubation induced differential expression of 35 pseudogenes compared to only 19 for LPS and $(GT)_6$-SWCNT treated cells. GSEA recapitulated these trends through enrichment of transcription regulation pathways including *DNA Repair*, *E2F Targets*, and *Myc Targets V1* which all showed negative enrichment scores for COOH-SWCNT treatment. Further work is needed to determine whether this deviation from $(GT)_6$-SWCNT arises from mechanistic differences between covalent and noncovalent SWCNT suspension-receptor interactions, differences in aggregation state, or some other root cause. Nevertheless, these experiments provide a fundamental understanding of how various types SWCNT constructs may affect cells within the brain and will inspire further research into the nature of SWCNT-immune cell interactions.

4.6 Materials and Methods

Preparation of neuro-sensors

Single-walled carbon nanotubes (SWCNTs) were dispersed in aqueous solution using $(GT)_6$ single stranded DNA by combining 0.2 mg of small diameter HiPco™ SWCNTs (NanoIntegris) and 50 μM of ssDNA (Integrated DNA Technologies, Inc.) in 1 mL of 0.01 M phosphate-buffered saline (PBS). Solutions were probe-tip sonicated for 10 minutes using a 3 mm probe tip at 50% amplitude (5-6 W, Cole-Parmer Ultrasonic Processor). Following sonication, samples were centrifuged at 16,100 cfg for 30 minutes to pellet unsuspended SWCNT bundles, amorphous carbon, and metallic contaminants. Supernatant containing dispersed $(GT)_6$-SWCNTs was collected. Excess DNA was removed via centrifugal filtration using an Amicon Ultra-0.5 mL centrifugal filter with a 100 kDa molecular weight cutoff (Millipore Sigma). Samples were placed in the filter and centrifuged at 8,000 cfg then washed with Milli-Q water. This process was repeated five times. Sample was recovered by reversing the spin filer and centrifuging into a collection tube at 1,000 cfg. Concentration of $(GT)_6$-SWCNT suspensions was determined using sample absorbance at 632 nm and the corresponding extinction coefficient ε_{632nm} = 0.036 mL cm μg^{-1}. $(GT)_6$-SWCNTs were diluted to a 10x stock concentration of 100 μg/mL in 0.1 M PBS and stored at 4°C.

PEG-PE passivated $(GT)_6$-SWCNTs were produced by mixing equal volumes of 200 μg/mL PEG-PE (Avanti Polar Lipids) and 200 μg/mL $(GT)_6$-SWCNT in 0.1 M PBS. The mixture was bath sonicated for 15 min. Samples were used as prepared or stored at 4°C.

Carboxylic acid functionalized SWCNTs (Sigma Aldrich) were suspended in water by mixing approximately 1 mg solid COOH-SWCNT with 1 mL water and sonicating using the same settings detailed above. Centrifugation at 16,100 cfg for 30 minutes was again used to pellet and remove amorphous carbon, metallic catalysts, and unsuspended COOH-SWCNTs.

Prior to use in cell culture experiments, SWCNT suspensions were screened for endotoxin contamination using the Limulus amebocyte lysate (LAL) assay. Both $(GT)_6$-SWCNT and COOH-SWCNT were confirmed to be below the limit of detection for endotoxin content.

Fura-2 AM, $DiSBAC_2(3)$, and Di-2-ANEPEQ (Thermo Fisher) were reconstituted in DMSO and diluted to a working concentration of 20 μM in PBS. rAAV1/Syn-GCaMP3 virus (UNC Vector Core, titer: 5×10^{12} virus molecules/mL) was diluted to a concentration of 2.5×10^{11} virus molecules/mL in PBS.

RNA-seq library preparation and gene expression analysis

SIM-A9 cells were cultured as previous described (see **3.7 Materials and Methods**). Cells were plated in a 24-well plate at a density of 0.1×10^6 cells per well in 500 μL of growth media. Cells were maintained at 37°C and 5% CO_2 until approximately 70% confluent then washed with PBS. Media was replaced with sera free DMEM/F12 for two hours prior to start of experiments. Stock neuro-sensor was added to wells at 10x concentration, 0.1x total volume. Final concentrations were: 10 ng/mL LPS, 10 μg/mL $(GT)_6$-SWCNT, 10 μg/mL COOH-SWCNT, 2 μM Fura-2, 2 μM $DiSBAC_2(3)$, 2 μM Di-2ANEPEQ, and 50,000 AAV molecules per SIM-A9 cell. Three biological replicates were run for each group.

Two hours post exposure, total RNA was collected from adherent cells using the Quick RNA Miniprep Kit (Zymo Research) following manufacturer instructions. Cells were lysed directly on the plate and DNase treatment was used to remove genomic DNA. Total RNA concentration was measured using the Qubit™ RNA BR Assay Kit (Thermo Fisher). RNA quality

was checked using the 2100 Bioanalyzer with RNA 6000 Nano Kit (Agilent). RIN scores were confirmed to be >7 prior to library preparation.

Libraries were prepared using Kapa Biosystems library preparation kit with mRNA selection with poly-A magnetic beads. Libraries were pooled and sequenced on an Illumina NovaSeq S4 flow cell with 150 paired end reads. Targeted data return was 25M read pairs per sample. Raw reads were pre-processed using *HTStream* (version 1.0.0) for filtering out adapter sequences, quality scores < 30, and mouse ribosomal RNA (https://github.com/ibest/HTStream). Pre-processed reads were mapped to the Gencode M20 *Mus musculus* genome (GRCm38.p6) and quantified using *STAR* aligner (version 2.5.4b).[139] The *edgeR* package was used to determine differentially expressed genes.[128] Adjusted p values were calculated using the Benjamini-Hockberg procedure using the *edgeR* default false discovery rate (FDR < 0.05). Gene ontology enrichment analysis was performed using the *topGO* R package.[130] Enrichment of GO terms and p values were computed using Fisher's exact test and the *weight01* algorithm with a $p_{adj} < 0.01$ cutoff for genes.[131] Gene set enrichment analysis was performed using the *fgsea* package for R.[140]

4.7 Supporting Information

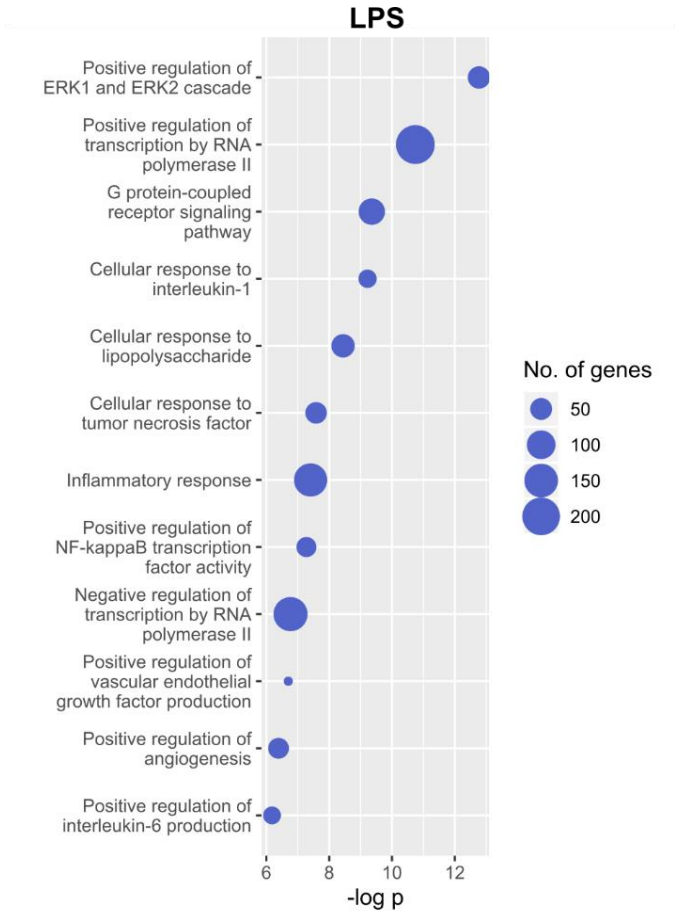

Figure S4.1 Gene ontology enrichment of LPS treated microglia at 2 hours. Top twelve most highly enriched gene ontology terms for RNA-seq libraries generated from LPS treated microglial cells.

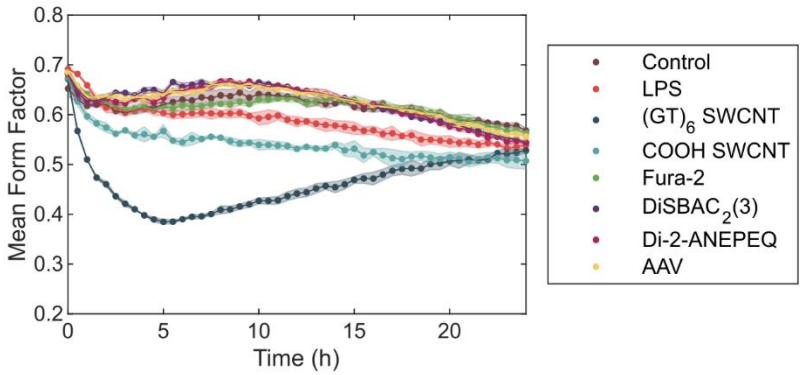

Figure S4.2 Microglial morphology change induced by neuro-probes. Cell morphology change upon addition of neuro-sensors at concentrations used for RNA-seq studies. SIM-A9 cells were at 37°C and 5% CO_2, in sera free media. Shaded regions represent standard error of the mean (N = 3).

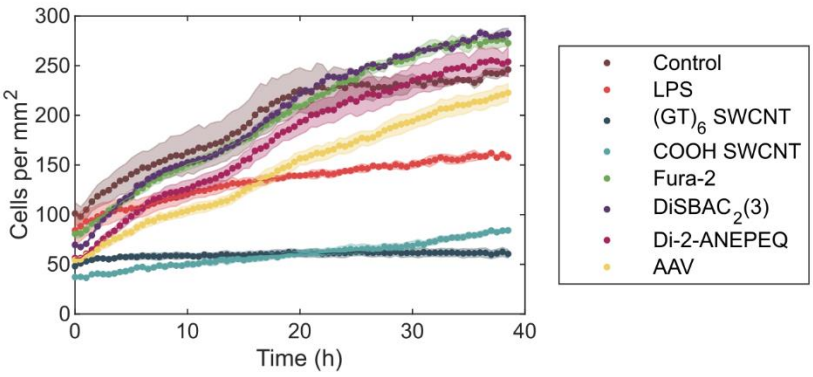

Figure S4.3 Effect of neuro-probes on microglial cell proliferation. Cell count per mm^2 of tissue culture surface area upon addition of neuro-sensors at concentrations used for RNA-seq studies. SIM-A9 cells were at 37°C and 5% CO_2, in sera free media. Shaded regions represent standard error of the mean (N = 3).

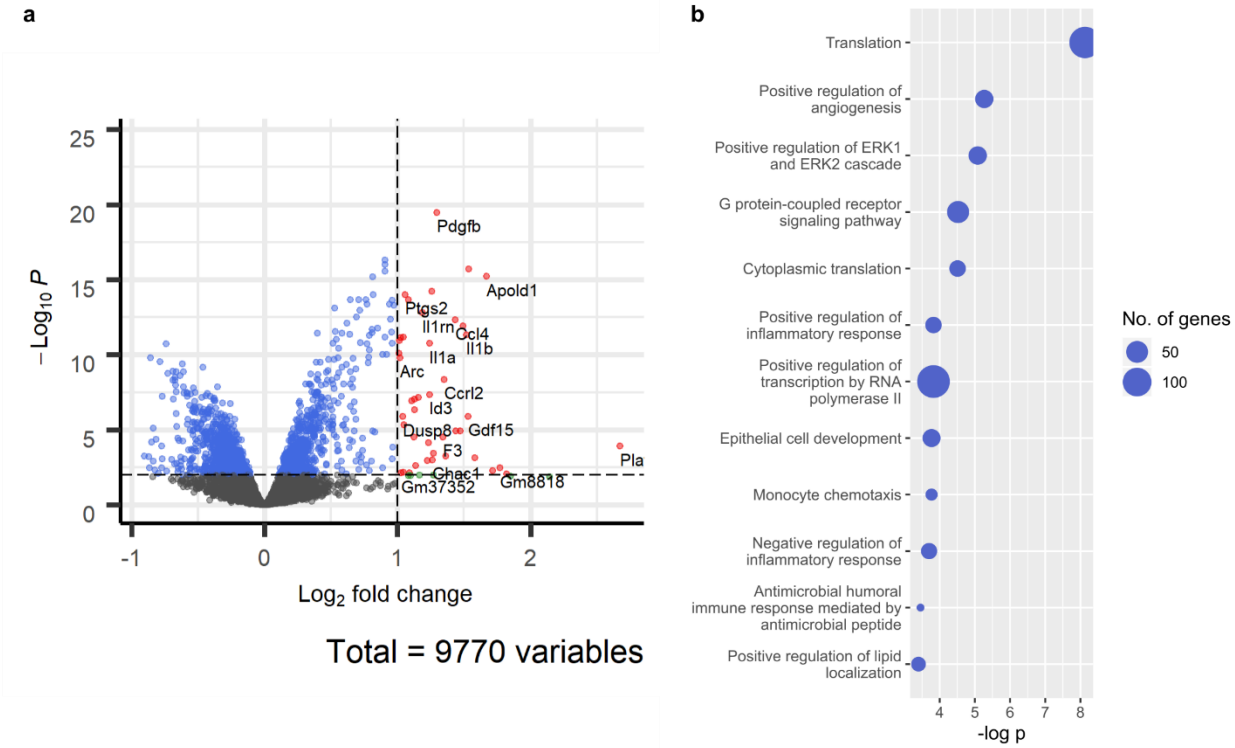

Figure S4.4 COOH-SWCNT treated SIM-A9 differential gene expression. (a) Volcano plot highlighting differentially expressed genes identified between COOH-SWCNT and untreated cell control libraries. **(b)** Top 12 gene ontologies overrepresented by DE genes in COOH-SWCNT incubated microglia.

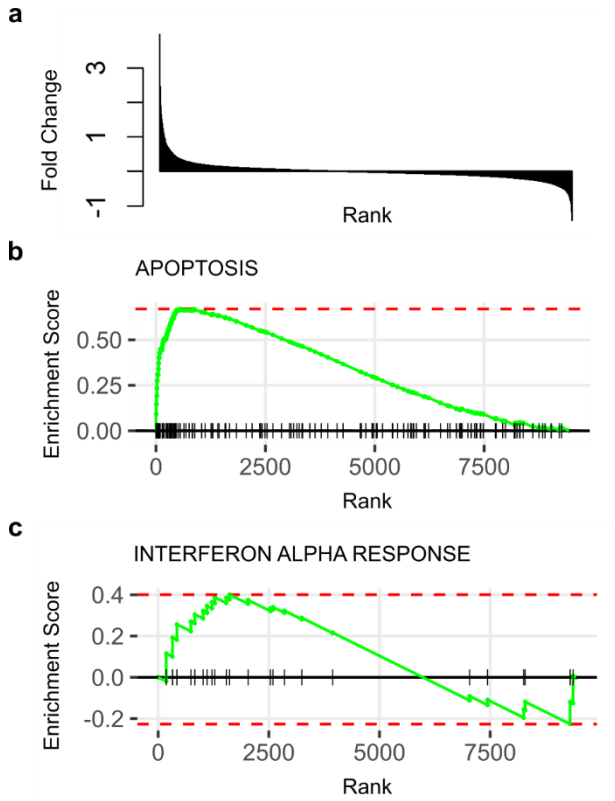

Figure S4.5 Hallmark gene set enrichment. (a) Bar plot of genes ranked in terms of decreasing expression fold change for $(GT)_6$-SWCNT treated SIM-A9 vs. untreated control sequencing libraries. **(b–c)** Enrichment plots for **(b)** Apoptosis and **(c)** Interferon alpha response hallmark pathways showing enrichment score calculated from annotated genes with respect to position in the ranked list. Dashed line indicates the reported maximum enrichment score.

Table S4.1 Gene set enrichment analysis of COOH-SWCNT treated SIM-A9 sequencing libraries

Pathway	p value	Normalized Enrichment Score
TNFA SIGNALING VIA NFKB	1.80E-03	3.33
HYPOXIA	1.84E-03	2.64
CHOLESTEROL HOMEOSTASIS	1.91E-03	1.80
MITOTIC SPINDLE	1.79E-03	1.53
WNT BETA CATENIN SIGNALING	6.07E-03	1.83
TGF BETA SIGNALING	1.92E-03	2.25
IL6 JAK STAT3 SIGNALING	1.95E-03	2.23
DNA REPAIR	2.18E-03	-1.77
APOPTOSIS	1.86E-03	2.38
ESTROGEN RESPONSE EARLY	1.83E-03	2.05
ESTROGEN RESPONSE LATE	1.81E-03	1.76
MYOGENESIS	1.82E-03	1.70
APICAL JUNCTION	1.83E-03	2.23
APICAL SURFACE	4.12E-03	1.84
COMPLEMENT	1.81E-03	2.31
E2F TARGETS	2.25E-03	-1.59
MYC TARGETS V1	2.23E-03	-2.06
EPITHELIAL MESENCHYMAL TRANSITION	1.94E-03	2.26
INFLAMMATORY RESPONSE	1.82E-03	2.85
OXIDATIVE PHOSPHORYLATION	2.24E-03	-2.42
P53 PATHWAY	1.79E-03	1.66
UV RESPONSE UP	1.82E-03	1.62
UV RESPONSE DN	1.85E-03	2.19
HEME METABOLISM	1.81E-03	1.68
COAGULATION	1.88E-03	2.06
IL2 STAT5 SIGNALING	1.80E-03	2.56
ALLOGRAFT REJECTION	1.82E-03	1.98
KRAS SIGNALING UP	1.81E-03	2.20
KRAS SIGNALING DN	1.86E-03	1.97

Chapter 5:
Passivation of SWCNT Neuro-Sensors

Portions of this chapter are reproduced and adapted with permission from Ref 23. Copyright 2020 American Chemical Society.

5.1 Introduction

One of the foremost concerns over the use of artificial nanoparticles in biomedical applications is that of biocompatibility. Biocompatibility studies are focused on ensuring that the material in question performs only its desired function in the target tissue, with minimal or negligible off-target effects, such as the microglial activation observed in Chapter 3. A common approach to imparting biocompatibility to nanotechnologies involves nanoparticle surface functionalization with polyethylene glycol (PEG) polymers to promote steric exclusion of proteins, increase nanoparticle hydrophilicity, and thereby prevent subsequent immune activation.

Various methods exist for modifying a surface with PEG, ranging from covalent to adsorptive approaches. Covalent linkage of PEG to surfaces using chemical syntheses such as thiol-maleimide reactions has been shown to produce long-lasting PEG brush layers.[141] In one case, conjugation of PEG to carboxylic acid groups of the SWCNT carbon lattice resulted in reduced inflammation in mouse lungs compared to non-PEGylated SWCNT after intravenous injection.[142] However, performing these reactions on the carbon nanotube graphene lattice can ablate nIR photoluminescence, as defect sites on the pristine carbon lattice can act as exciton quenchers.[143,144] Physisorption of PEG or PEG containing molecules is another avenue of imbuing surfaces with anti-fouling properties. These electrostatic or hydrophobic interactions are less stable than the previous category of PEGylation and are prone to PEG desorption through changes in pH and other environmental factors.[141] Nevertheless, this class of modification preserves SWCNT photoluminescence and consequently, sensing ability.

Dispersants such as PEGylated phospholipid are commonly used to mitigate protein adsorption and increase the stability of SWCNT suspensions in biological environments. SWCNTs have previously been dispersed using PEGylated phospholipids to form highly disperse suspensions.[11,66] These PEG-phospholipid SWCNTs have enabled imaging of brain blood vessels through the skull,[7] and tracking of particle diffusion throughout the brain extracellular space.[82] However, the creation of a hybrid ssDNA and PEG-phospholipid SWCNT surface coating for dual sensing and biocompatibility purposes remains unexplored.

This chapter focuses on evaluating the biocompatibility of SWCNT constructs for brain imaging by quantifying their impact on microglial cells, utilizing methodologies and metrics established in previous sections including FAM-fibrinogen adsorption, cell form factor, and cytokine expression to evaluate and compare novel neuro-sensor constructs. In parallel, the efficacy of novel, engineered nanosensors is tested using *in vitro* experiments to ensure that the SWCNT modifications cause no loss in catecholamine sensing ability. Finally, modified nanosensors are implanted in excised mouse brain tissue for catecholamine imaging and compared to existing, unmodified nanosensor to prove unequivocal improvement to the nIRCat platform.

5.2 Noncovalent Adsorption of Phospholipids to SWCNT Surface

To mitigate tissue response to ssDNA-SWCNTs, we developed a noncovalent modification strategy for passivation of $(GT)_6$-SWCNT nanosensors using PEGylated phospholipids which display a high affinity for the SWCNT surface. We used saturated 16:0 PEG-phosphatidylethanolamines (PEG-PE) with varying PEG molecular weights ranging from 750 Da to 5000 Da to form co-suspensions with $(GT)_6$-SWCNTs, then assessed their effect on nanosensor biocompatibility and efficacy. Sonication of $(GT)_6$-SWCNTs with PEG_{2000}-PE at a 1:1 SWCNT to phospholipid mass ratio caused a decrease in SWCNT nIR fluorescence intensity and a red shifting of the fluorescence emission (**Figure 5.1a–b**), indicating an increase in the polarity of the SWCNT dielectric environment, consistent with biomolecular adsorption phenomena.[22,35,36] This result is recapitulated in the absorbance spectra of $(GT)_6$-SWCNTs, where nIR absorbance peaks corresponding to SWCNT E_{11} transitions are red-shifted upon passivation with PEG-PE with variable PEG molecular weights (**Figure 5.1c**). The 750 Da PEG phospholipid caused the highest magnitude wavelength shift, whereas larger 2000 Da and 5000 Da PEG phospholipids induced intermediate red-shifting. This larger solvatochromic shift may indicate higher surface density of PEG_{750}-PE on the SWCNT surface compared to larger PEG chains.

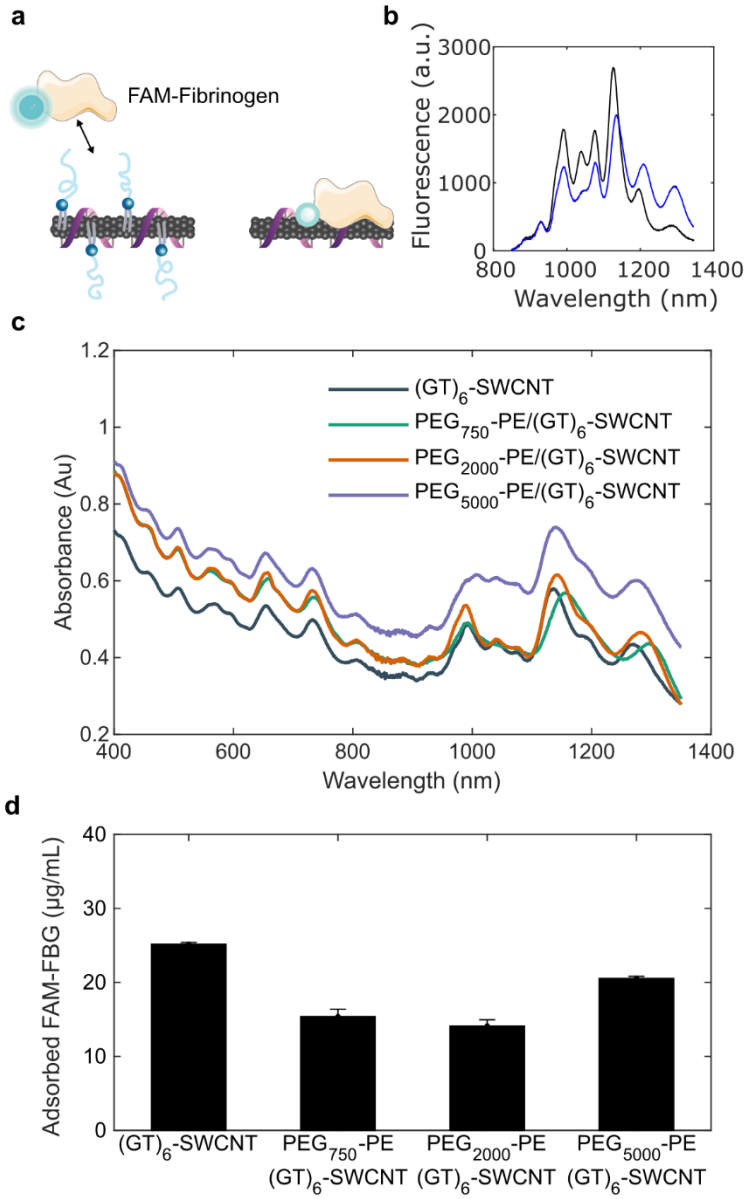

Figure 5.1 Passivation of $(GT)_6$-SWCNTs with PEG-PE phospholipid. (a) Schematic of PEG-PE adsorption to $(GT)_6$-SWCNTs and subsequently deterring FAM-fibrinogen adsorption. **(b)** Comparison of nIR fluorescence spectra of 5 µg/mL $(GT)_6$ -SWCNT (black) vs. PEG_{2000}-PE/$(GT)_6$-SWCNT (blue). **(c)** UV-vis-nIR absorbance of 20 µg/mL $(GT)_6$-SWCNT, PEG_{750}-PE/$(GT)_6$-SWCNT, PEG_{2000}-PE/$(GT)_6$-SWCNT, and PEG_{5000}-PE/$(GT)_6$-SWCNT. Spectra collected on a UV-3600i Plus UV-Vis-NIR Spectrophotometer using dual beam measurement with stair correction. **(d)** Concentration of adsorbed FAM-FBG on 5 µg/mL $(GT)_6$-SWCNT. Initial concentration of FAM-FBG added to solution was 40 µg/mL. Error bars represent standard error of the mean (N = 3).

Nonspecific protein adsorption was quantified on PEG-PE/$(GT)_6$-SWCNT passivated nanosensor constructs using a previously developed method for tracking biomolecular adsorption on nanoparticle surfaces in real-time [22]. Blood coagulation protein fibrinogen (FBG) was selected as a representative binding protein owing to its high affinity for the SWCNT surface.[22] SWCNT-induced quenching of the fluorophore fluorescein conjugated to fibrinogen (FAM-FBG) was used to determine the degree of adsorption of 40 µg/mL FAM-FBG to 5 µg/mL $(GT)_6$-SWCNTs with

and without PEG-PE passivation (**Figure 5.1d**, **S5.1**). All molecular weight PEG-PEs caused a reduction in total concentration of adsorbed FAM-FBG after 1 h incubation. Phospholipids with a PEG molecular weight of 2000 Da best mitigated against protein adsorption, showing a 28 ± 2% reduction in adsorption of FAM-FBG after 1 h compared to unmodified $(GT)_6$-SWCNT nanosensors. The degree of FAM-FBG adsorption on PEG_{2000}-PE/$(GT)_6$-SWCNTs was comparable to SWCNTs suspended with solely PEG_{2000}-PE (**Figure 5.2**). Furthermore, this methodology was also effective in mitigating nonspecific protein adsorption on COOH-SWCNT (**Figure S5.2**). These covalently modified carbon nanotubes adsorbed ___-fold more FAM-FBG than ssDNA wrapped pristine SWCNTs. PEG-PE passivation reduced adsorption by 6.8 ± 0.3%, 6. ± 0.3%, and 4.4 ± 0.6% for 750, 2000, and 5000 Da PEG molecular weights respectively. Further analysis of the interactions between carboxylated SWCNTs and phospholipids is needed to further optimize the protocol for COOH-SWCNT passivation. Nevertheless, this points to the generalizability of this noncovalent modification strategy to other nanomaterial platforms.

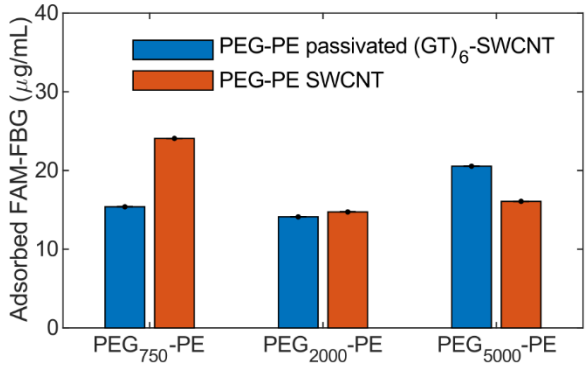

Figure 5.2 Protein adsorption on PEG-PE suspended SWCNTs. Adsorption of 40 μg/mL FAM-FBG determined by quenching of conjugated FAM fluorophore to 5 μg/mL $(GT)_6$-SWCNTs passivated with PEG-PE of varying PEG molecular weights vs. SWCNTs suspended with PEG-PE.

Unlike covalent modification of the pristine carbon lattice surface, this passivation method preserved both the intrinsic SWCNT nIR fluorescence and the $(GT)_6$-SWCNT molecular recognition for dopamine (**Figure 5.3a–b**). Interestingly, the *in vitro* nanosensor response ($\Delta F/F_0$) upon addition of 200 μM dopamine increased upon $(GT)_6$-SWCNT nanosensor passivation with PEG_{2000}-PE at a 1:1 mass ratio, relative to the unpassivated $(GT)_6$-SWCNT nanosensor, with $\Delta F/F_0$ = 2.01 and $\Delta F/F_0$ = 1.44, respectively. This effect was driven primarily by phospholipid-induced quenching of SWCNT baseline fluorescence. Furthermore, we tested whether PEG-passivated nanosensors would better withstand biofouling and nanosensor attenuation by blood plasma proteins. We found that the attenuation of $(GT)_6$-SWCNT dopamine nanosensor response by plasma proteins was mitigated by PEG_{2000}-PE passivation, where nanosensor incubation in 2% plasma caused nanosensor $\Delta F/F_0$ fluorescent response to decrease by 73% for unpassivated $(GT)_6$-SWCNTs, compared to a 50% fluorescent response decrease for PEG_{2000}-PE/$(GT)_6$-SWCNTs (**Figure 5.3c**).

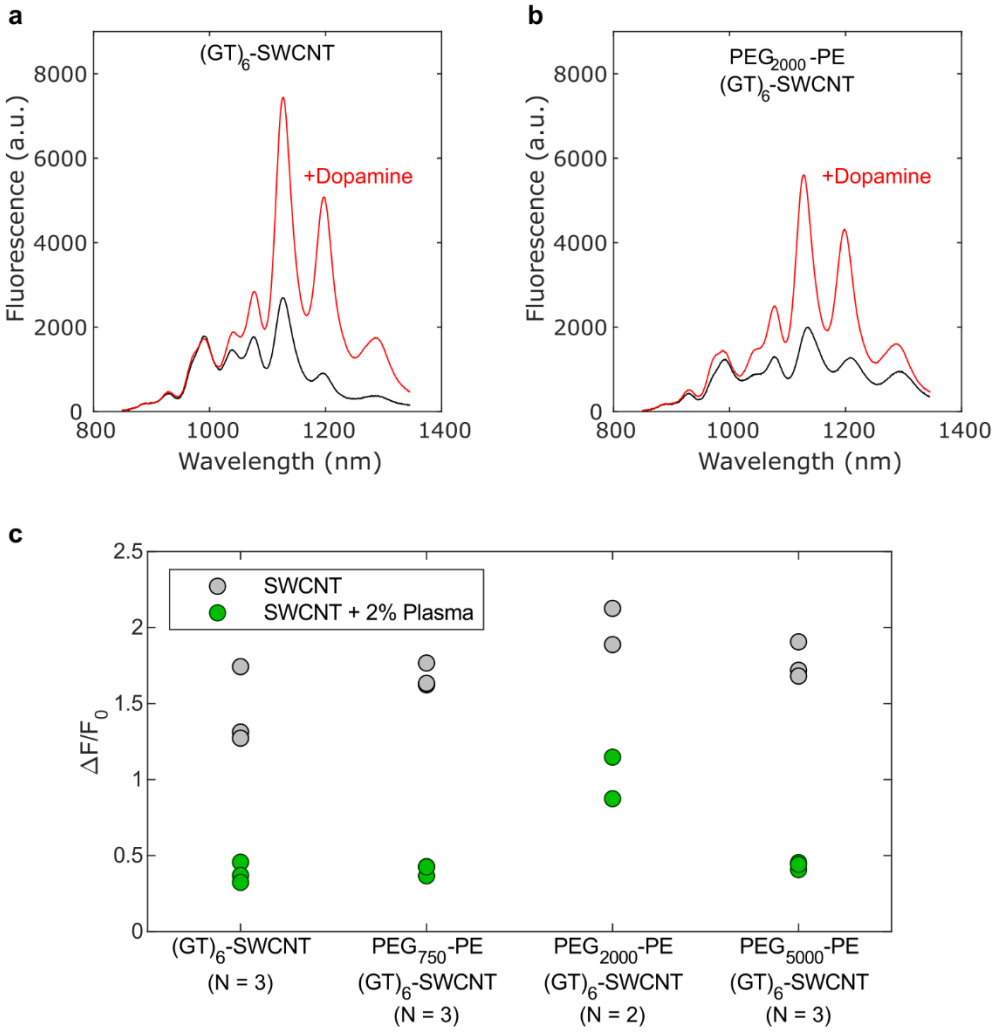

Figure 5.3 Dopamine response of PEG-PE passivated SWCNTs. (a–b) Near infrared fluorescence spectra of **(a)** $(GT)_6$-SWCNT and **(b)** PEG_{2000}-PE passivated $(GT)_6$-SWCNT before and after addition of 200 µM dopamine. **(c)** Fluorescence response to 200 µM dopamine of 5 µg/mL $(GT)_6$-SWCNT and PEG-PE/$(GT)_6$-SWCNT with PEG molecular weights of 750, 2000, and 5000 Da (grey). Dopamine response in biological milieu was simulated by pre-incubating SWCNT suspensions with 2% human blood plasma for 15 min (green). Each data point represents an distinct SWCNT preparation and response assay. N values are listed in the x axis label.

The change in sensor behavior imparted by PEG-PE passivation did not cause any negative effects to sensor selectivity to chemical neurotransmitters. For all ten molecules screened, PEG_{2000}-PE/$(GT)_6$-SWCNT showed similar magnitude of response as unpassivated $(GT)_6$-SWCNT neuro-sensor (**Figure 5.4**). The largest turn-on responses were observed for catecholamines (ephinephrine, norepinephrine, and dopamine) as has previously been reported in the literature.[9,12] Serotonin showed a moderate fluorescence response, 55.3 ± 4.5% and 75.6 ± 2.2% that of the response to dopamine by $(GT)_6$-SWCNT and PEG_{2000}-PE/$(GT)_6$-SWCNT respectively. This is consistent with prior studies which show that serotonin interacts with ssDNA functionalized SWCNTs with high ssDNA sequence dependence.[2] Furthermore, the fluorescence response to each analyte was improved by passivation with PEGylated phospholipid. In particular,

catecholamine $\Delta F/F_0$ increased by 25.2 ± 7.8% for epinephrine, 25.6 ± 4.3% for norepinephrine, and 42.8 ± 9.4% for dopamine. Hence, this noncovalent modification maintains sensor selectivity while improving response to all potential analytes. The higher increase in response to serotonin relative to catecholamines may potentially be leveraged for further improving the sensitivity of ssDNA-wrapped SWCNT-based serotonin sensors.

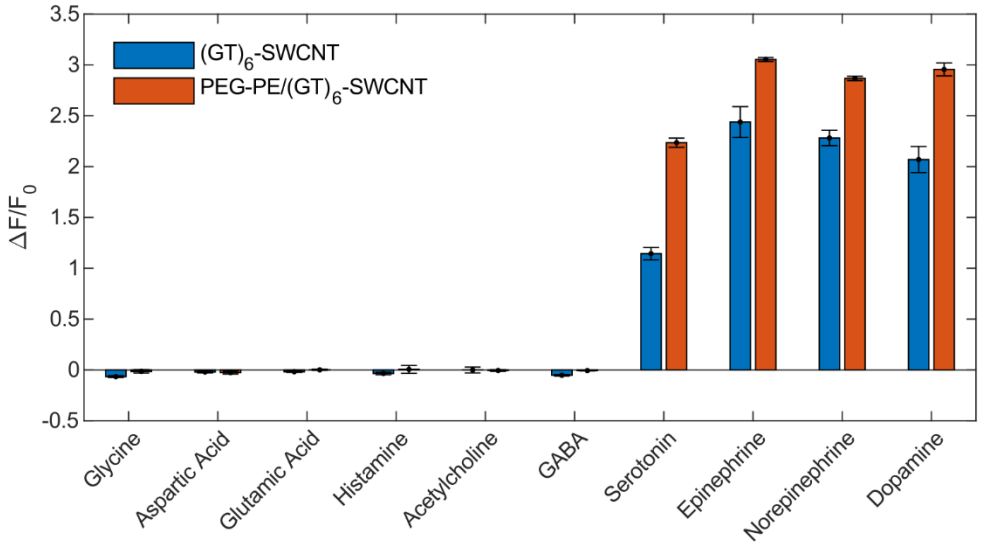

Figure 5.4 Selectivity of phospholipid passivated neuro-sensor. Near-infrared fluorescence response of 5 μg/mL $(GT)_6$-SWCNT and PEG_{2000}-PE/$(GT)_6$-SWCNT to neurotransmitters (100 μM). Fluorescence response, $\Delta F/F_0$, is measured using integrated fluorescence from 850 – 1350 nm. Error bars represent standard error of the mean (N = 3).

5.3 Mitigation of Microglial Response with Passivated Sensor

We next examined the interaction of PEG-PE/$(GT)_6$-SWCNTs nanosensors with SIM-A9 microglia, first testing the extent to which these probes affect cell morphology. Analogous to our protein adsorption mitigation results, the 2000 Da PEG length showed the greatest mitigation in SIM-A9 morphology change (**Figure 5.5a–c**). Unmodified $(GT)_6$-SWCNTs caused mean form factor to decrease to a minimum of 0.490 ± 0.013, whereas the PEG_{2000}-PE/$(GT)_6$-SWCNTs merely led to a minimum of 0.618 ± 0.005. PEG-PE modified samples also exhibited a return to baseline morphology returning to untreated control levels after 9, 6 and 15 h respectively for 750, 2000, and 5000 Da PEG molecular weights. Conversely, unmodified $(GT)_6$-SWCNT nanosensors did not show a return to baseline morphology within the 24 h experiment.

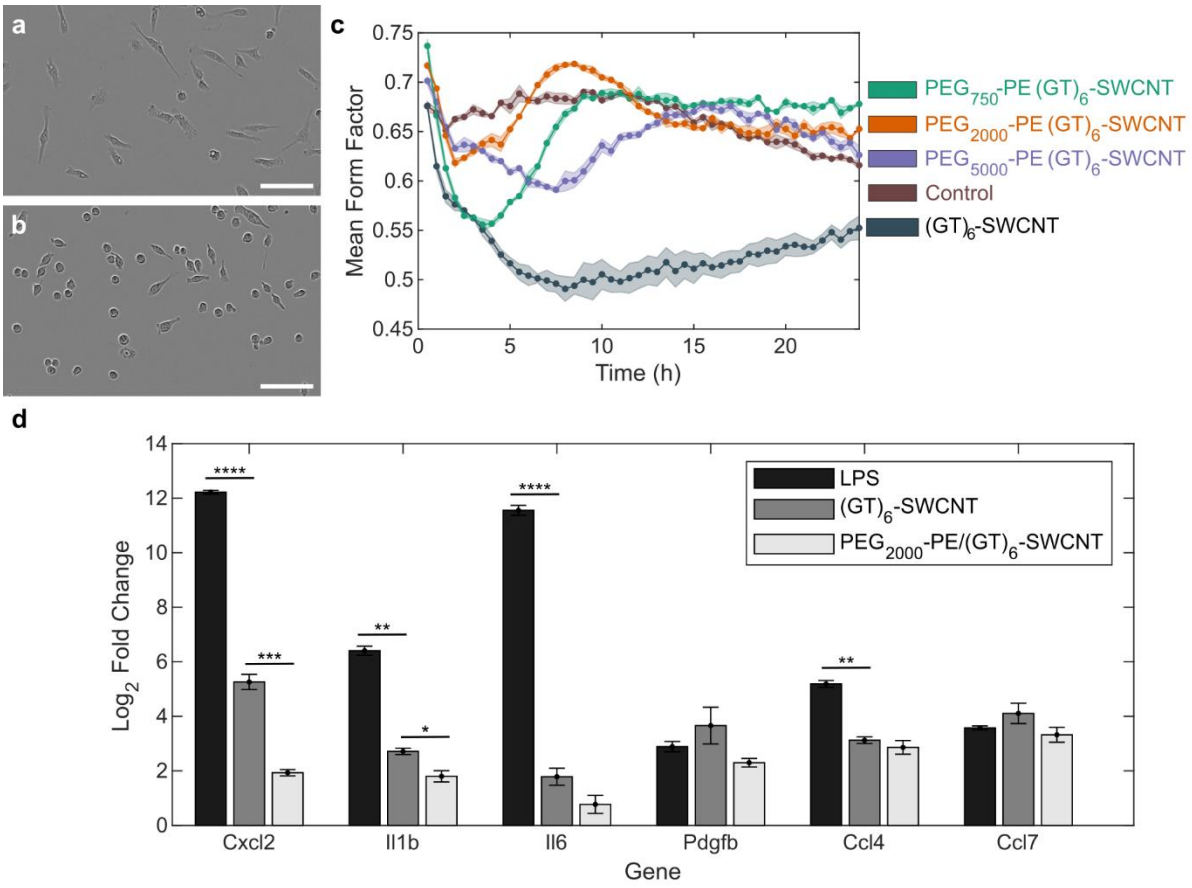

Figure 5.5 Effect of PEG-PE phospholipid passivation on microglial activation. (a–b) Phase contrast images of SIM-A9 microglial cells incubated with **(a)** $(GT)_6$-SWCNTs and **(b)** PEG_{2000}-PE passivated $(GT)_6$-SWCNTs at 5 µg/mL for 6 h. Scale bars are 100 µm. **(c)** Mean form factor time traces of SIM-A9 microglia incubated with PEG-PE passivated vs. unpassivated $(GT)_6$-SWCNTs compared to no treatment control. Shaded regions represent standard error of the mean (N = 3). **(d)** Quantitative reverse transcriptase PCR expression-fold change of SWCNT inflammatory cytokine markers upon stimulation with 5 ng/mL lipopolysaccharide, 5 µg/mL $(GT)_6$-SWCNT, and 5 µg/mL PEG_{2000}-PE/$(GT)_6$-SWCNT. Incubation time was 2 h. Error bars represent standard error of the mean (N = 3). Statistical analyses compare LPS and PEG_{2000}-PE/$(GT)_6$-SWCNT relative expression changes to that of $(GT)_6$-SWCNT: * $p < 0.05$, ** $p < 0.005$, *** $p < 5 \times 10^{-4}$, **** $p < 5 \times 10^{-5}$.

Using quantitative reverse transcriptase PCR (RT-qPCR), we quantified the inflammatory response of SIM-9 microglia exposed to PEG_{2000}-PE/$(GT)_6$-SWCNT nanosensors. Noncovalent passivation of ssDNA-wrapped SWCNTs with PEG-PE phospholipid caused a reduction in SIM-A9 inflammatory response, exemplified by a decrease in the expression of inflammatory cytokines previously identified as upregulated in our transcriptomic studies. Specifically, genes *Cxcl2*, *Il1b*, *Il6*, *Pdgfb*, *Ccl4*, and *Ccl7* were selected as SWCNT-specific upregulated biomarkers from the $(GT)_6$-SWCNT and COOH-SWCNT libraries of the RNA-seq screen. As measured by qPCR, PEG_{2000}-PE/$(GT)_6$-SWCNT suspensions induced either marginally or significantly lower upregulation of all 6 genes in SIM-A9 microglia compared to $(GT)_6$-SWCNTs **(Figure 5.5d)**. In particular, *Cxcl2* expression change decreased significantly by 90 ± 2% when nanosensors were treated with PEG_{2000}-PE. Upregulation of *Il1b* decreased by 47 ± 8%. Overall, SWCNT-induced expression changes of *Cxcl2*, *Il1b*, *Il6*, and *CCL4* were significantly lower than those induced by LPS.

5.4 Imaging Dopamine Release

We imaged striatal dopamine release in acute mouse brain slices to evaluate the utility of PEG-phospholipid passivated SWCNT nanosensors as dopamine probes. PEG_{2000}-PE/$(GT)_6$-SWCNTs and $(GT)_6$-SWCNTs were introduced into acute coronal brain slices, as previously described, by incubating fresh, 300 μm thick coronal brain slices in artificial cerebral spinal fluid (ACSF) containing 2 mg/L of dopamine nanosensor (**Figure 5.6a**).[1] The nanosensor-labeled slices were then washed with ACSF and imaged in a continuously perfused ACSF bath. We electrically stimulated dopamine release from dopamine-containing axons within the dorsal lateral striatum and simultaneously imaged SWCNT nIR fluorescence response to changes in extracellular dopamine concentration. As expected, slices labeled with $(GT)_6$-SWCNTs showed low nIR fluorescence signal prior to stimulation, followed by an increase in fluorescence response immediately after 0.3 mA electrical stimulation, and an eventual return to the low intensity - baseline ~5 s after stimulation (**Figure 5.6b**). Brain slices labeled with PEG_{2000}-PE/$(GT)_6$-SWCNTs showed a similar nIR fluorescence response to 0.3 mA electrical stimulation (**Figure 5.6c**), suggesting both the native dopamine probe and the PEG_{2000}-PE-passivated probe enable imaging of dopamine release and reuptake kinetics in brain tissue.

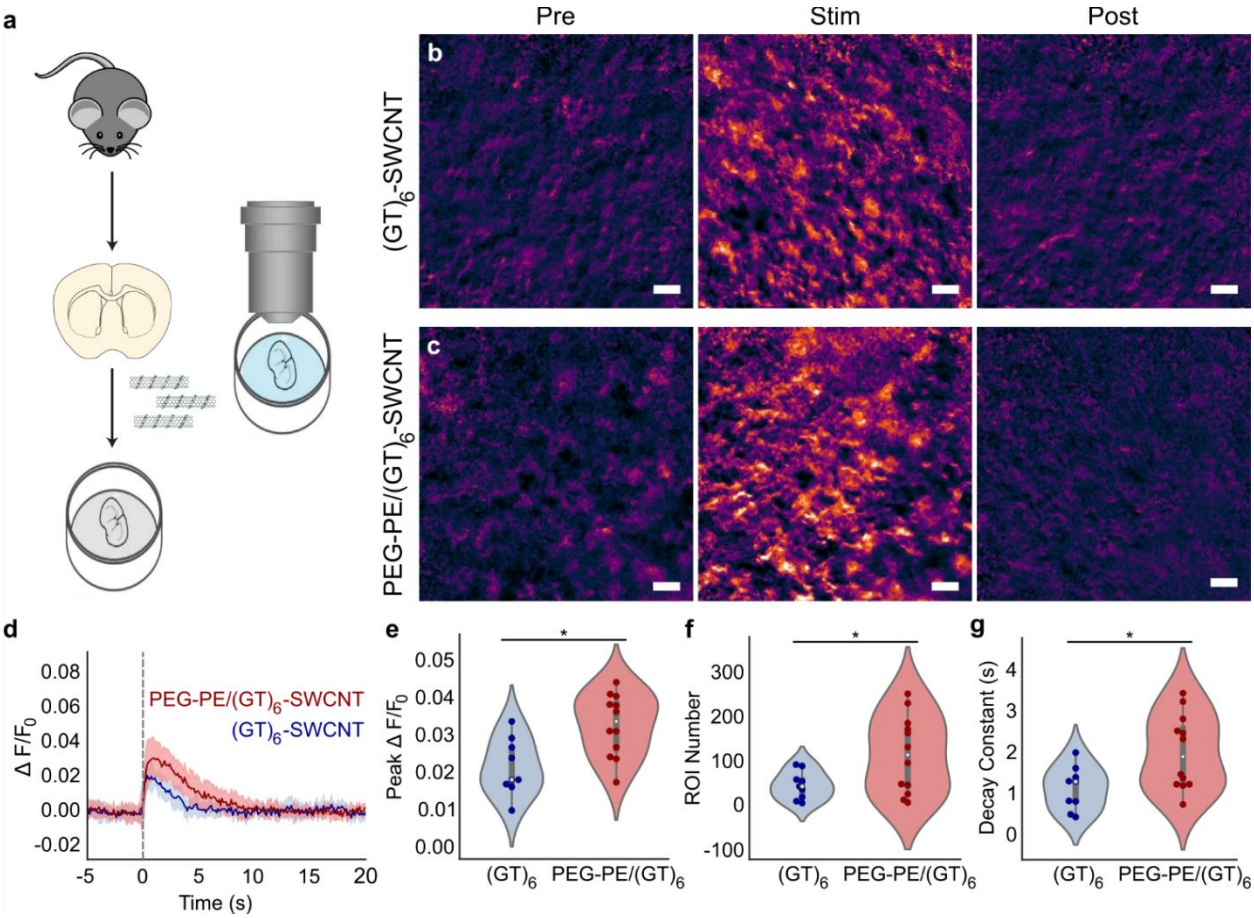

Figure 5.6 Imaging of dopamine release and reuptake dynamics in acute mouse striatal brain slices. (a) Schematic of acute mouse brain slice preparation and incubation with SWCNT nanosensors before dopamine release and reuptake imaging. **(b–c)** Representative images showing normalized nIR fluorescence signal ($\Delta F/F_0$) of **(b)** $(GT)_6$-SWCNT and **(c)** PEG_{2000}-PE/$(GT)_6$-SWCNT in striatum of mouse brain before stimulation, at peak $\Delta F/F_0$ shortly after 0.3 mA single-pulse stimulation, and after SWCNT nanosensor signal returned to baseline. Scale bars are 10 µm. **(d)** Fluorescence response time trace of identified regions of interest (ROI) in brain slices labeled with $(GT)_6$-SWCNT (blue) and PEG_{2000}-PE/$(GT)_6$-SWCNT during electrically evoked dopamine release. Dashed line indicates time of 0.3 mA single-pulse electrical stimulation. Solid lines represent mean traces and shaded regions represent one standard deviation around the mean for 3-4 mice, 1 brain slice per mouse, and 3 recordings per slice ($(GT)_6$: N = 9, PEG-PE/$(GT)_6$: N = 12). **(e–g)** Violin plots showing the distribution of metrics from each mean nanosensor fluorescence trace for **(e)** peak $\Delta F/F_0$ signal, **(f)** number of identified regions of interest (ROIs), and **(g)** decay constant from fitting mean nanosensor $\Delta F/F_0$ time trace a first-order decay function. Dark points represent measurements calculated from a single stimulation recording. White dots represent the mean. The gray bar spans the spread of the data while the bold portion of the bar spans from the first to third quartiles. The shaded regions represent the probability density of the data across the range of the metric measured. * $p < 0.05$.

We next characterized the spatial extent of nanosensor response to evoked dopamine release from striatal tissue. As described previously by Beyene *et al.*,[1] we programmatically identified spatial regions of interest within the imaged brain tissue in which statistically significant increases in SWCNT fluorescence were recorded upon electrical stimulation (0.3 mA) of dopamine release. These regions of interest (ROI) represent spatial sub-regions where dopamine release and re-uptake modulation occurs during electrical stimulation. Fluorescence time traces from ROIs were normalized to baseline fluorescence ($\Delta F/F_0$) and averaged across four brain slices

per SWCNT treatment and three stimulation recordings per slice. Average $\Delta F/F_0$ of time traces from both $(GT)_6$-SWCNT and PEG_{2000}-PE/$(GT)_6$-SWCNT labeled slices show that both nanosensors demonstrate a robust fluorescence response to dopamine released in living brain slices followed by a rapid return to baseline as dopamine is cleared from the extracellular space (**Figure 5.6d**). For the same 0.3 mA stimulation intensity, PEG_{2000}-PE/$(GT)_6$-SWCNTs exhibited a peak $\Delta F/F_0$ of 0.032 ± 0.002 compared to 0.021 ± 0.003 for unmodified $(GT)_6$-SWCNTs (**Figure 5.6e**). This increased peak $\Delta F/F_0$ indicates improved dopamine responsivity by PEG_{2000}-PE/$(GT)_6$-SWCNTs compared to the unpassivated counterpart. PEG-phospholipid modified SWCNTs also improved ROI identification. In acute brain slices labeled with PEG_{2000}-PE/$(GT)_6$-SWCNTs, 158 ± 37 ROI were identified vs. 81 ± 15 ROI in $(GT)_6$-SWCNT labeled slices (**Figure 5.6f**). The higher ROI number may indicate improved extracellular access to dopaminergic terminals within the brain tissue. Conversely, PEG_{2000}-PE/$(GT)_6$-SWCNTs show 1.8 ± 0.4-fold higher decay constant, indicating a slower return to baseline fluorescence (**Figure 5.6g**). As an additional control, stimulation at higher intensity (0.5 mA) revealed similar trends for the above metrics (**Figure S5.3**). However, the increase in peak $\Delta F/F_0$ and ROI number from PEG_{2000}-PE passivation was diminished and no statistically significant difference was observed between modified and unmodified sensors (**Figure S5.3a–c**). This may indicate saturation of sensor response from increased dopamine release at the higher electrical stimulation intensity. Nevertheless, the $\Delta F/F_0$ time trace decay constant was again significantly higher for PEG_{2000}-PE/$(GT)_6$-SWCNTs, showing a 1.7 ± 0.4-fold increase for the passivated neuro-sensor (**Figure S5.3d**). To determine if this effect arises from altered sensor kinetics, we analyze the concentration-dependent fluorescence response.

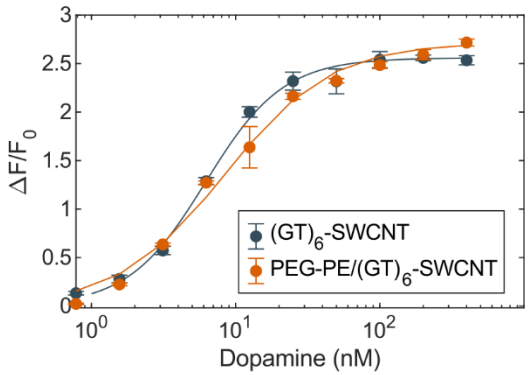

Figure 5.7 Neuro-sensor equilibrium kinetics. Dopamine response curve for 1 µg/mL $(GT)_6$-SWCNT and PEG_{2000}-PE/$(GT)_6$-SWCNT. Lines are Hill equation fits. Error bars represent standard error of the mean (N = 3).

Sensor equilibrium kinetics were evaluated by measuring fluorescence response with respect to dopamine concentration (**Figure 5.7**). Both $(GT)_6$-SWCNT and PEG_{2000}-PE/$(GT)_6$-SWCNT exhibit a concentration dependent response between 1 and 100 nM dopamine. The fluorescence response data was fit to the Hill equation (Equation 5.1).

$$\theta = \frac{[L]^n}{K_D + [L]^n} \qquad \text{(Eq. 5.1)}$$

The dissociation constant (K_D) and sensor cooperativity (n) were calculated using a least squares curve fit (**Table 5.1**). This reveals extremely similar values for K_D for both sensors ranging from 12.3 – 19.0 nM, consistent with results from prior studies.[9,12] However, phospholipid-passivated sensor showed lower Hill coefficient with n = 1.18 compared to n = 1.62 for unmodified sensor. This indicates positive cooperativity in dopamine binding ability of $(GT)_6$-SWCNT or an increase in dopamine affinity at higher adsorbed concentrations. PEG_{2000}-PEG/$(GT)_6$-SWCNT may display a lower cooperativity constant due to decreased contact between adjacent adsorbed dopamine molecules as a result of separation of ssDNA molecules by PEG-PE within the SWCNT corona. Subsequently, this suggests that at low dopamine concentrations, near the limit of detection, the unmodified SWCNT probe displays a higher $\Delta F/F_0$. This may account for the lower decay constant assuming extracellular dopamine concentrations are less than the dissociation constants of the sensors, roughly 12.3 nM. However, due to the proximity of the dopamine response curves of both sensors, this effect is more likely manifests due to the improved diffusive abilities and higher response in protein-rich environments.

Table 5.1 Hill equation fitting parameters

Sensor	K_D (nM)	n
$(GT)_6$-SWCNT	19.0	1.62
PEG-PE/GT_6-SWCNT	12.3	1.18

Regardless, the PEG_{2000}-PE/$(GT)_6$-SWCNT sensor displays higher dopamine sensitivity in mouse brain tissue over $(GT)_6$-SWCNT, particularly at lower stimulation intensities, suggesting dopamine nanosensors and other SWCNT-based neurotechnologies may benefit from this passivation approach.

5.5 Conclusions

Passivation of exposed graphene lattice of $(GT)_6$-SWCNT nanosensor by physisorbed PEGylated phospholipid is a simple, inexpensive process which greatly improves sensor function. Sonication of PEG_{2000}-PE phospholipid with $(GT)_6$-SWCNT imparted anti-fouling capability, causing a 28% reduction in adsorption of FAM-fibrinogen. This coincides with a 23% lower reduction of *in vitro* $\Delta F/F_0$ after incubation in blood plasma. Upon exposure to these modified SWCNTs, SIM-A9 microglial cells exhibited mitigation of morphology change and upregulation of pro-inflammatory genes. Furthermore, the limited morphology change by PEG_{2000}-PE/$(GT)_6$-SWCNTs showed a return to mean form factor baseline within 6 hours of incubation, a similar timeframe as the small degree of ramification induced by LPS. It is unknown if this change in time-dependence of response is also reflected in transient cytokine gene expression.

Labeling of *ex vivo* mouse brain tissue with these modified sensors also resulted in immediate improvements. Compared to unmodified $(GT)_6$-SWCNTs, PEG_{2000}-PE/$(GT)_6$-SWCNTs showed an increase in both fluorescence signal and responsivity in acute mouse brain slices, increasing the max $\Delta F/F_0$ following 0.3 mA electrical stimulation by 52 ± 8%. Furthermore, PEG_{2000}-PE/$(GT)_6$-SWCNTs increased the number of identified ROI by 160 ± 50% potentially

indicating improved dispersion of nanosensors or higher nanosensor sensitivity to dopamine release in tissue. However, PEG-PE passivated sensor labeled brain slices exhibited delayed return to fluorescence baseline post electrical stimulation. *In vitro* experiments showed this may arise from a change in cooperativity of sensor-analyte kinetics due to separation of SWCNT-adsorbed ssDNA molecules by PEG-PE. As such, a correction accounting for sensor-analyte kinetics is necessary in order to yield the true dopamine release and reuptake kinetics. However, this is a requirement of any sensor used in dynamic molecular imaging.

Taken together, our data suggest that phospholipid PEG passivation of carbon nanotubes provides an avenue for improving both the biocompatibility and *in vivo* functionality of numerous SWCNT-based technologies already in proliferous use for neurobiological studies. Further research using methodologies presented herein may reveal molecules analogous to PEG-PE which perform even better at preventing negative molecular interactions and promoting selective molecular recognition.

5.6 Materials and Methods

Fluorescence tracking of protein adsorption

FAM fluorophore was conjugated to fibrinogen (FBG) using N-Hydroxysuccinimide (NHS) ester chemistry according to the protocol described in Pinals *et al* [22]. SWCNT and FAM-FBG were mixed in a 1:1 volume ratio, 50 µL total in a 96 well PCR plate (Bio-Rad) and placed in a CFX96 Real-Time PCR System (Bio-Rad). Final concentrations were 5 µg/mL SWCNT and 40 µg/mL FAM-FBG. Scans were collected across all fluorescence channels (FAM, HEX, Texas Red, Cy5, Quasar 705) at 30 s intervals with temperature set to 22.5°C, lid heating off. A FAM-FBG fluorescence standard curve was used to convert fluorescence readings to unbound FAM-FBG concentrations.

Near infrared fluorescence measurements

SWCNTs were diluted to a concentration of 5 µg/mL in PBS. A 40 µL aliquot was added to a 384 well plate with optical bottom (Corning). The plate was placed on a motorized stage of an inverted Zeiss microscope (Axio Observer.D1) coupled to an InGaAs array detector (Princeton Instruments). SWCNT nIR fluorescence spectra were measured using a 10x objective with 721 nm laser excitation. Fluorescence response to dopamine was measured by collecting spectra before and after addition of 10 µL, 100 µM dopamine hydrochloride.

RT-qPCR

Total RNA was collected from adherent SIM-A9 cells with varying treatment conditions as previously described using the Quick RNA Miniprep Kit (Zymo Research) following manufacturer instructions. RNA was reverse transcribed to cDNA libraries using the iScript cDNA Synthesis Kit (Bio-Rad) with a 1 µg RNA input. Next, 2 µL of cDNA was used with the PowerUp SYBR Green Master Mix (Thermo Fisher) and 500 nM of forward and reverse primers (**Table S5.1**). The housekeeping genes, *Gadph* and *Pgk1* were used. Samples were cycled in a CFX96 Real-Time System (Bio-Rad) for 40 cycles (denature at 95°C for 15 s, anneal at 55° for 15 s, and extend at 72°C for 1 min). Data was analyzed using CFX Maestro software (Bio-Rad). Relative gene expression was calculated using the $\Delta\Delta C_q$ method. P values were calculated using an unpaired t-test (N = 3). RNA-seq experiments revealed that Pgk1 housekeeping gene did not undergo differential expression upon any treatment conditions. Melt curve analysis of RT-qPCR products was performed to ensure specific amplification.

Mouse brain slice preparation and imaging

Acute brain slices were prepared from Male C57BL/6 Mice (JAX Strain 000664: https://www.jax.org/strain/000664) between the ages of 43-46 days. All mice were group-housed after weaning at postnatal day 21 (P21) and kept with nesting material on a 12:12 light cycle. All animal procedures were approved by the University of California Berkeley Animal Care and Use Committee. Preparation of acute brain slices followed previously established protocol [1]. Mice were deeply anesthetized via intraperitoneal injection of ketamine/xylazine and perfused transcardially using ice-cold cutting buffer (119 mM NaCl, 26.2 mM NaHCO3, 2.5 mM KCl, 1 mM NaH2PO4, 3.5 mM MgCl2, 10 mM glucose, and 0 mM CaCl2). The perfused brain was extracted and the cerebellum removed. The brain was then mounted on to a vibratome (Leica VT1200 S) cutting stage using super glue and cut into 300 µm thick coronal slices containing the dorsal striatum. Slices were then transferred to 37˚C oxygen-saturated ACSF (119 mM NaCl, 26.2 mM NaHCO3,

2.5 mM KCl, 1 mM NaH2PO4, 1.3 mM MgCl2, 10 mM glucose, and 2 mM CaCl2) for 30 minutes and then transferred to room temperature ACSF for 30 min. At this point, slices were ready for incubation and imaging and maintained at room temperature.

Prepared coronal slices were transferred into a small-volume incubation chamber (AutoMate Scientific) containing 5 mL oxygen-saturated ACSF. Two hundred microliters of 50 mg/L GT_6-SWCNT or PEG_{2000}-PE/$(GT)_6$-SWCNT was added to the incubation chamber and the slice was allowed to incubate for 15 min. The slice was subsequently rinsed three times in baths of oxygen-saturated ACSF to wash off excess nanosensor. The labeled slice was transferred to an imaging chamber continually perfused with ACSF at 32˚C. A bipolar stimulation electrode (125 µm Tungsten, 0.1 mΩ, WE3ST30.1A5 Micro Probes Inc.) was positioned in the dorsomedial striatum using a 4x objective (Olympus XLFluor 4x/340). The stimulation electrode was then brought into contact with the top surface of the brain slice 200 µm away from the imaging field of view using a 60x objective. All stimulation experiments were recorded at video frame rates of 9 frames per second for 600 frames and single, mono-phasic pulse (1 ms) electrical stimulations were applied after 200 frames of baseline were acquired. Each slice received pseudo-randomized stimulation at 0.3 mA and 0.5 mA, which were repeated three times each. Slices were allowed to recover for 5 min between each stimulation, with the excitation laser path shuttered. The excitation laser path was un-shuttered 1 min before beginning video acquisition.

Timeseries image stacks were processed using a suite of custom written MATLAB scripts (2019b MathWorks, https://github.com/jtdbod/Nanosensor-Brain-Imaging). A grid was superimposed over each frame to generate ~7 µm x 7 µm regions of interest (ROIs). For each ROI, the mean pixel intensity F(t) was calculated for each frame to generate an average intensity time trace. $\Delta F/F_0(t) = (F(t) - F_0)/F_0$ traces were generated with F_0 calculated by averaging the mean ROI intensity of 10 frames prior to electrical stimulation followed by subtracting a linear offset to correct for drift. We estimated baseline noise (σ_0) of $\Delta F/F_0(t)$ by fitting a Gaussian to negative fluctuations from a moving averaged baseline. ROI's were discarded from further analysis if no transient greater than $3\sigma_0$ was observed following stimulation. Remaining ROIs were then averaged to generate field of view (FOV) averaged $\Delta F/F_0$ traces for each recording.

From each mouse brain, two brain slices were selected at random and incubated with either $(GT)_6$-SWCNTs or PEG_{2000}-PE/$(GT)_6$-SWCNTs. For each brain slice, three nIR fluorescence movies were collected at each stimulation intensity. A total of four mice brains were used. One sample was excluded for $(GT)_6$-SWCNT incubation due to poor slice quality for a total of N = 9 and N = 12 recordings per stimulation intensity for $(GT)_6$-SWCNT and PEG-PE/$(GT)_6$-SWCNT neuro-sensors respectively. Statistical analysis of metrics calculated from $\Delta F/F_0$ time traces was performed using an unpaired t-test to determine p values comparing $(GT)_6$-SWCNT to PEG_{2000}-PE/$(GT)_6$-SWCNT incubated brain slices.

5.7 Supporting Information

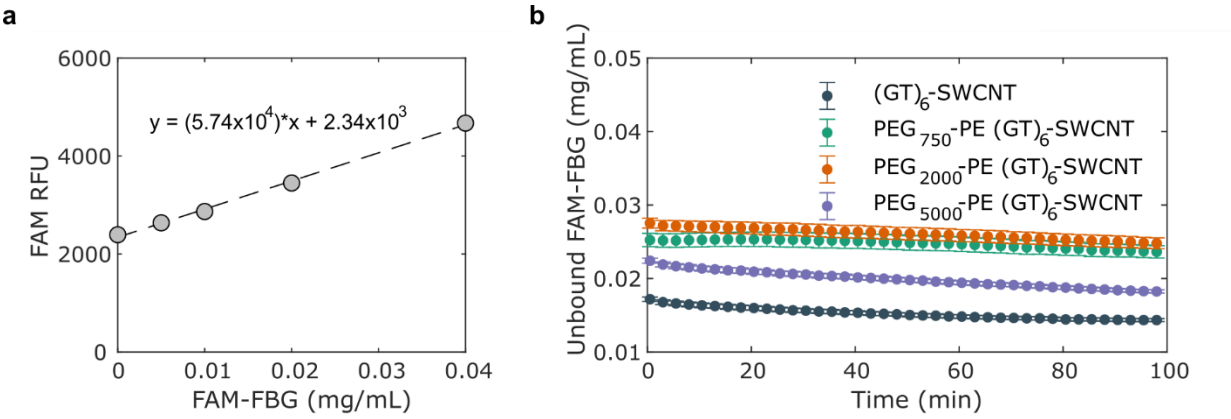

Figure S5.1 Quantification of real-time FAM-fibrinogen adsorption to SWCNTs. (a) FAM-FBG fluorescence calibration curve. **(b)** Concentration time series of unbound FAM-FBG. Protein added at total concentration of 40 µg/mL FAM-FBG to 5 µg/mL SWCNT.

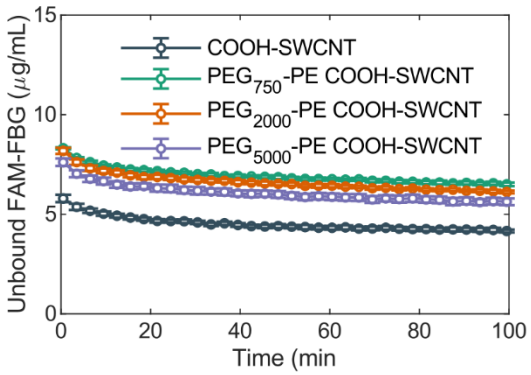

Figure S5.2 PEG-phospholipid passivation of COOH-SWCNT. Adsorption of 40 µg/mL FAM-FBG to 5 µg/mL COOH-SWCNT passivated with PEG-PE phospholipid at a 1:1 mass ratio. Protein adsorption is tracked *via* the unbound protein concentration quantitated using the FAM fluorescence. Errorbars represent standard error of the mean (N = 3).

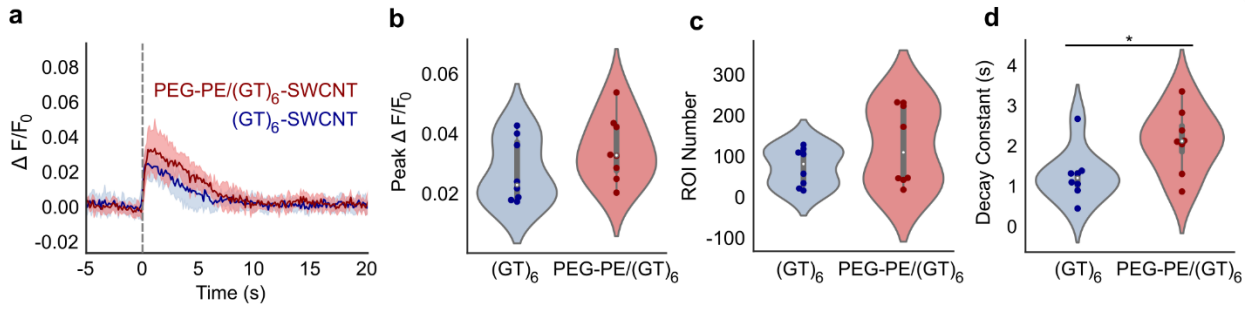

Figure S5.3 Striatal dopamine release in acute mouse brain slice with 0.5 mA electrical stimulation. (a) Near-infrared fluorescence time traces of regions of interest (ROI) identified in acute mouse brain slice labeled with $(GT)_6$-SWCNTs (blue) and PEG_{2000}-PE/$(GT)_6$-SWCNTs (red). Dashed line indicates 0.5 mA single-pulse electrical stimulation. Solid lines represent mean traces and shaded regions represent one standard deviation around the mean for 4 mice, 1 brain slice per mouse, and 3 recordings per slice (N = 12). **(b–d)** Violin plots showing the distribution of metrics from each mean nanosensor fluorescence trace for **(b)** peak $\Delta F/F_0$, **(c)** number of identified regions of interest (ROIs), and **(d)** decay constant from fitting mean nanosensor $\Delta F/F_0$ time trace a first-order decay function. Dark points represent mean values calculated from each fluorescence video containing a single stimulation event. White dots represent the mean and the gray bar spans from the first to third quartiles. * $p < 0.05$.

Table S5.1 Primers for RT-qPCR

Gene	Forward Strand (5' -> 3')	Reverse Strand (5' -> 3')
GADPH	ACCACAGTCCATGCCATCAC	CTGGTTCCTGAAGCGACAAC
Pgk1	CTGACTTTGGACAAGCTGGAC	GCAGCCTTGATCCTTTGGTTG
Cxcl2	CTCTCAAGGGCGGTCAAAAAGTT	TCAGACAGCGAGGCACATC
IL-1b	GCACTACAGGCTCCGAGATGA	TTGTCGTTGCTTGGTTCTCCTTG
IL6	CCTCTGGTCTTCTGGAGTACC	ACTCCTTCTGTGACTCCAGC
PDGFb	GTTGCAACGAGAAAGCCGGAG	GTCTGTCTATCTACCCACTCGC
CCL4	CCCAGCTCTGTGCAAACCTA	CCATTGGTGCTGAGAACCCT
IL-1b	TGCCACCTTTTGACAGTGATG	AAGGTCCACGGGAAAGACAC

Chapter 6: Summary

Portions of this chapter are reproduced and adapted with permission from Ref 23. Copyright 2020 American Chemical Society.

The popularity of single-walled carbon nanotubes as fluorescent molecular probes has continued to rise, owing to their unique material properties. However, these same properties lead to unintended consequences once applied to complex biological systems. In this work, I show that the hydrophobic graphene lattice structure of the SWCNT serves as an ideal platform to adsorb polymers such as single-stranded DNA which confer molecular recognition to catecholamine neuromodulators with high specificity. However, this same surface is highly prone to protein adsorption and subsequent sensor biofouling. Biofluids cause significant decrease in near-infrared fluorescence response of SWCNT nanosensors to dopamine. In particular, a 5% blood plasma dilution caused an 81.0 ± 0.9% decrease in response in $(GT)_6$-SWCNT. This effect was showed to be largely due to adsorption of high affinity proteins including fibrinogen, a blood clotting factor. Fibrinogen was found to adsorb 168% more than albumin and caused 26% more signal attenuation upon addition of dopamine. A fluorescence quenching tracking assay was developed to monitor the kinetics of protein adsorption and ssDNA desorption from the SWCNT surface. This assay allowed for simultaneous tracking of adsorption of multiple biomolecule species and enabled identification of protein corona composition on the SWCNT surface. Fitting of adsorption time traces to a competitive adsorption model produced kinetic rate constants for biomolecular ad- and desorption consistent with above trends. Furthermore, adsorption modeling revealed a large SWCNT loading capacity and an initial ssDNA surface coverage of approximately 1%, a value lower than others cited in the literature. This lends to the possibility of passivation of unoccupied SWCNT surface to prevent subsequent protein adsorption and unfavorable interactions with cell surface receptors. Studying the dynamics of SWCNT-protein interactions provided invaluable data for understanding the fundamentals of ssDNA-SWCNT interaction with biological environments. These findings are then applied to advance the development of ssDNA-SWCNT sensors with neuroscience applications where major concerns have arisen over the potential for the carbon lattice to cause immune cell activation, an effect which may significantly perturb homeostasis in the very tissue under study by these nanomaterial probes.

Herein, we assess the impact of SWCNTs on SIM-A9 microglial cells. Microglial activation manifests in multiple cellular mechanisms, including a rapid change in cell morphology and upregulation of genes and pathways specific to the microglial immune response. We find that $(GT)_6$-SWCNT nanosensors caused a large and persistent change in SIM-A9 morphology, transitioning from round, motile cells to multipolar, ramified cells with higher adhesion. This morphological effect which manifested at SWCNT concentrations where cytotoxicity was not observed, was greater in magnitude than that induced by common immunogen lipopolysaccharide, and was associated with extensive growth of actin cytoskeletal protrusions. The greater persistence and magnitude of morphology change induced by carbon nanotubes over LPS may be due to the relative persistence of SWCNTs within cellular environments, with degradation times on the order of days to weeks in tissue.[145,146] The full transcriptomic response induced by $(GT)_6$-SWCNT nanosensors was evaluated at 0.5 and 2 h time points using RNA-seq. This response was then compared to that elicited by 2 h exposure to other commonly used neuro-imaging and neuro-delivery probes.

Using high-throughput sequencing, we showed that both noncovalent $(GT)_6$-SWCNTs and covalent carboxylated SWCNTs cause significant perturbations to the SIM-A9 transcriptome at shorter incubation times than LPS. This indicates that while LPS causes a stronger inflammatory response through toll-like receptor binding, as observed by higher fold changes in cytokine gene expression, SWCNTs may interact with cell signaling pathways through faster mechanisms. Differential gene expression analysis was used to identify genes expressed by SIM-A9 microglia that are highly upregulated in the presence of $(GT)_6$-SWCNT nanosensors. These include *Cxcl2*, *Il1b*, *Il6*, *Pdgfb*, *Ccl4*, and *Ccl7*. Statistical analysis of DE genes revealed that the predominant transcriptomic response to SWCNTs is an inflammatory response, whereby similarities in gene ontologies over-represented by differentially expressed genes from both $(GT)_6$-SWCNT and LPS libraries suggest this effect is due to activation of TLR2/4 and the NF-κB signaling pathway. Gene set enrichment analysis using Hallmark gene sets identified Wnt/β-catenin signaling pathway as a pathway activated by $(GT)_6$-SWCNT but not by LPS. This cytoskeleton associated cell process may be a contributing factor to the morphological change induced by carbon nanotube samples. Comparison of $(GT)_6$-SWCNT treatment to that of calcium dye Fura-2, voltage sensitive probes $DiSBAC_2(3)$ and Di-ANEPEQ, and adeno-associated virus vector revealed that SWCNT catecholamine sensor impacts the SIM-A9 cell transcriptome far more significantly than these other common neuroscience probes, which also failed to elicit a cellular morphological response. We note that the inflammatory response caused by 5 μg/mL $(GT)_6$-SWCNTs is significantly lower in magnitude than that induced by a 1000-fold lower mass concentration of LPS. As such, the degree of neuroinflammation caused by SWCNTs is expected to be lower than that of a targeted pathogenic response. Nevertheless, mitigation of these effects is vital in developing a non-biologically impactful sensor for use in healthy brain tissue.

To mitigate the immunological effects prompted by DNA-SWCNTs in microglia, we developed a noncovalent modification strategy to passivate the exposed SWCNT surface with physisorbed PEGylated phospholipids. This methodology reduced nonspecific protein adsorption by 28 ± 2%, and when applied to SIM-A9 microglia, resulted in a reduction of both inflammatory cytokine upregulation and a decrease in mean form factor change. This modification retains the selective SWCNT-based nanosensor nIR fluorescence response to dopamine and reduces attenuation of nanosensor signal by protein adsorption. Lastly, we apply the passivated PEG_{2000}-PE/$(GT)_6$-SWCNT nanosensor to image electrically stimulated dopamine release and reuptake in acute mouse brain slices where immediate benefits were observed in fluorescence signal as well as dispersion of viable, extracellular nanosensor.

The work presented herein represents a research arc bridging carbon nanotube surface science to the biological, system-wide effects this class of artificial nanoparticle can inflict on brain tissue if left unchecked. I show that degree of nonspecific protein adsorption to different SWCNT constructs—as measured using a novel fluorophore quenching assay—can be used to distinguish these SWCNTs in terms of biocompatibility. Next, I present quantification of mechanisms identified in SIM-A9 microglial cells which were particularly affected by carbon nanotubes. These metrics then enable design of novel catecholamine sensors with improved sensing ability and reduced biological impact. This dissertation advances the field of carbon nanotube sensors towards *in vivo* molecular imaging. These experiments and methodologies provide the groundwork on which to develop carbon nanotube catecholamine sensors into a viable neuroscience tool for shining light on the complex chemical signaling occurring within our brains.

Appendix A:
Endotoxin Contamination of Carbon Nanotubes

Endotoxin is another term for lipopolysaccharides, or molecules found in the cell wall of Gram-negative bacteria such as E. Coli. These molecules are in a class of compounds known as pyrogens, substances which induce fever in a host organism when introduced into the bloodstream at sufficiently high concentrations. Testing for pyrogen and endotoxin contamination in intravenous drugs is a strict requirement of the United States Food and Drug Administration (FDA). Most commonly, endotoxins are detected using the Limulus amoebocyte lysate (LAL) assay which utilizes immune cell lysate from the eponymous horseshoe crab species. Four forms of the LAL assay are approved for use by the FDA, including the traditional gel-clot method and the more sensitive chromogenic assay. Since 1984, the FDA has imposed a limit of 0.25 EU/mL for injectable sterile water, where EU refers to endotoxin units (roughly 1 EU equates to 0.1-0.2 ng LPS).[147] However, this limit is meant to prevent pyrogenic effects which occur at dosages of approximately 5 EU/kg in humans.[148] Endotoxin limits for research applications are not as well-defined. Studies have shown significant activation of human immune cells with LPS concentrations as low as 0.02 ng/mL.[149] In the context of the brain, endotoxin induced activation of glia cells in the brain has been linked to incidence of neurodegenerative diseases such as Parkinson's disease.[150] Therefore, identifying and quantifying the presence of endotoxin in injectable neuro-technologies is of utmost importance.

Endotoxin contamination is an emerging issue in the field of bionanotechology. Many novel, synthetic nanomaterials have been found to have high affinities for lipopolysaccharides. Furthermore, the nonsterile environments in which these nanomaterials are produced leads to frequent bacterial contamination.[151] Moreover, in researching the biological impact of nanomaterials, endotoxin contamination can cloak the nanomaterial specific response by inducing a secondary inflammatory response causing significant activation of pro-inflammatory signaling cascades. Hence, I first tested pristine and carboxylated SWCNT stocks for endotoxin contamination using the Pierce Chromogenic Endotoxin Quant kit (Thermo Fisher).

High concentrations of carbon nanotubes have been shown to cause coagulation of LAL proteins resulting in false positive results.[152] For the chromogenic LAL assay, MWCNT concentrations greater than 0.3 μg/mL caused initiation of this effect. Consequently, all LAL assays were run using this value as an upper limit to SWCNT concentration. Both $(GT)_6$-SWCNT and COOH-SWCNT stocks showed endotoxin concentrations below the LAL assay limit of detection (**Figure A.1**). Extrapolated to a 10 μg/mL, this lower bound equates to 3.33 EU/mL, a value above the max allowable concentration for intravenous injection. Higher sensitivity assays can achieve a theoretical lower bound of 0.33 EU/mL however SWCNT concentration dependent assay inhibition/activation is not characterized for these protocols. As a result, I next explored options of endotoxin decontamination as a potential approach for ensuring endotoxin free conditions.

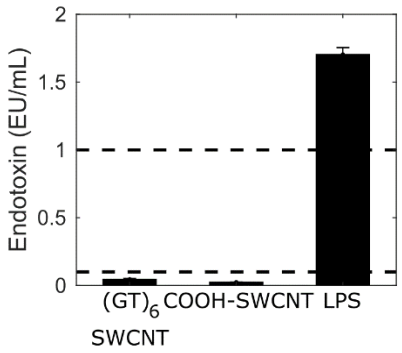

Figure A.1 LAL assay endotoxin concentration in SWCNTs used in SIM-A9 microglia RNA-seq experiments. Black dashed lines denote upper and lower limit of detection, 1 and 0.1 EU/mL respectively.

The ability to eliminate or decrease existing endotoxin contamination in nanomaterial samples is notoriously difficult, with many sources stressing the importance of avoiding contamination during synthesis.[151,153] Nevertheless, recent results in the literature suggest protocols of decontaminating multi-walled carbon nanotubes (MWCNTs) by autoclaving or heating solid nanomaterial stocks to 180°C in an oven, whereby MWCNTs following these protocols elicit different responses in macrophages.[154,155] These methods are aimed at selectively degrading organic molecules such as lipopolysaccharides due to their lower heat stability relative to carbon nanotubes.[156] To test the efficacy of these methods, I spiked pristine and carboxylated SWCNT stocks with small quantities of LPS. SWCNTs were mixed with water and small quantities were added to 4 mL glass scintillation vials. Next, I heat treated the solid SWCNTs either in an autoclave on the gravity cycle (40 min, 121°C) or in a heating element covered in sand for varying lengths and temperatures. Heating under atmospheric conditions above 200°C for over 1 h caused clear oxidation of the SWCNT, noted by a change in color from black to orange (**Figure A.2a**). This effect was mitigated by heating under N_2; however, longer heating times caused a noticeable decrease in solid SWCNT volume (**Figure A.2b**).

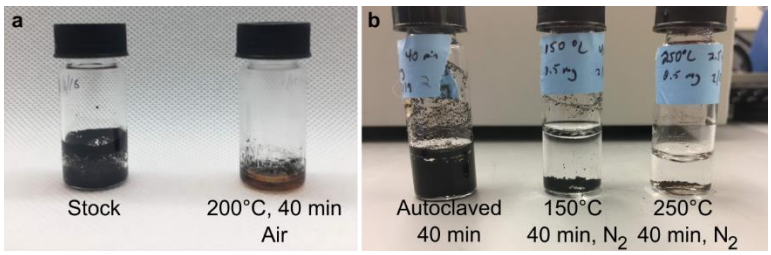

Figure A.2 Images of raw HiPCO SWCNTs before and after heating. (a) Heating in a sand bath under atmospheric conditions results in oxidation noted by a change in color to red-orange. **(b)** Heating under nitrogen mitigates visible oxidation but results in a decrease in solid SWCNT volume.

After heating, SWCNTs were suspended using Pluronic F-68, a non-ionic surfactant used to minimize potential interference with LAL proteins. Suspensions were diluted to 0.3 μg/mL before tested using the chromogenic LAL assay. Heating pristine SWCNTs for up to 3 h at 250°C only reduced endotoxin concentration by 8% (**Figure A.3a**). Heating for 24 h at 300°C in an argon

purged oven resulted in a 9% reduction for pristine SWCNTs (**Figure A.3b**). This treatment method was more effective for carboxylated SWCNTs, showing a 25% decrease in initial endotoxin concentration. However, the change in physical appearance of the solid SWCNT powder potentially indicates an undesirable change to the SWCNT chemistry which warrants further investigation.

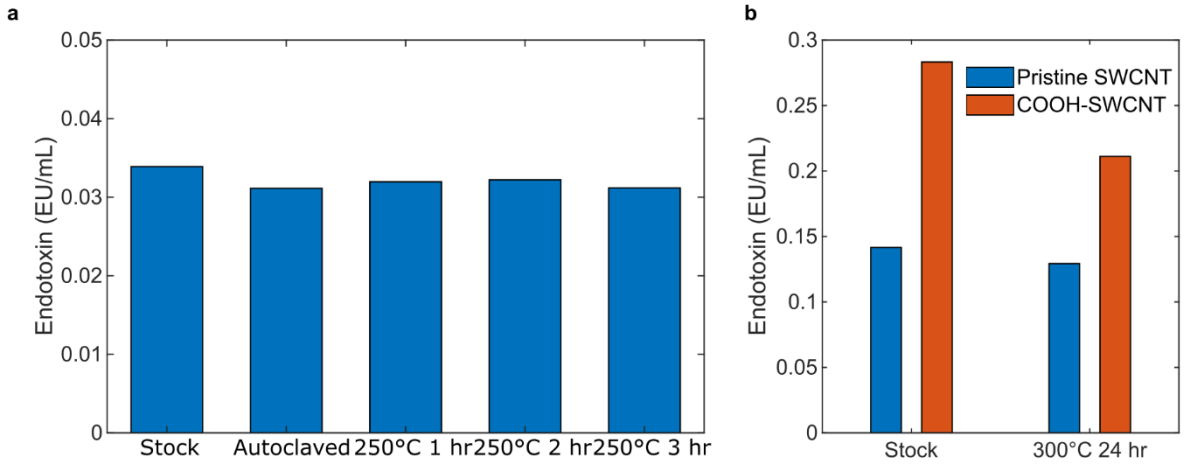

Figure A.3 Endotoxin concentration in SWCNT stocks before and after heating. (a) Endotoxin content of pristine SWCNTs with heat treatment (autoclave or heating under N_2). **(b)** Effect of heating pristine or carboxylated SWCNT in an Ar purged oven for 24 h on LAL assay quantified endotoxin concentration.

To quantify changes to the SWCNT graphene lattice due to heating, we use X-ray photoelectron spectroscopy (XPS) to analyze the SWCNT surface chemistry before and after treatment. Survey spectra from 0-1000 eV binding energy reveals an increase in the relative oxygen O1s orbital abundance compared to carbon C1s after 2.5 h at 250°C under N_2, suggesting oxidation of the carbon lattice from residual O_2 (**Figure A.4**). The Si2p vibrational mode likely originated from the solid substrate on which the SWCNT was deposited. Fe3p and Fe2p peaks were from iron catalyst from HiPCO SWCNT synthesis. Latent iron catalyst comprised only 3.8% of the total atomic composition.

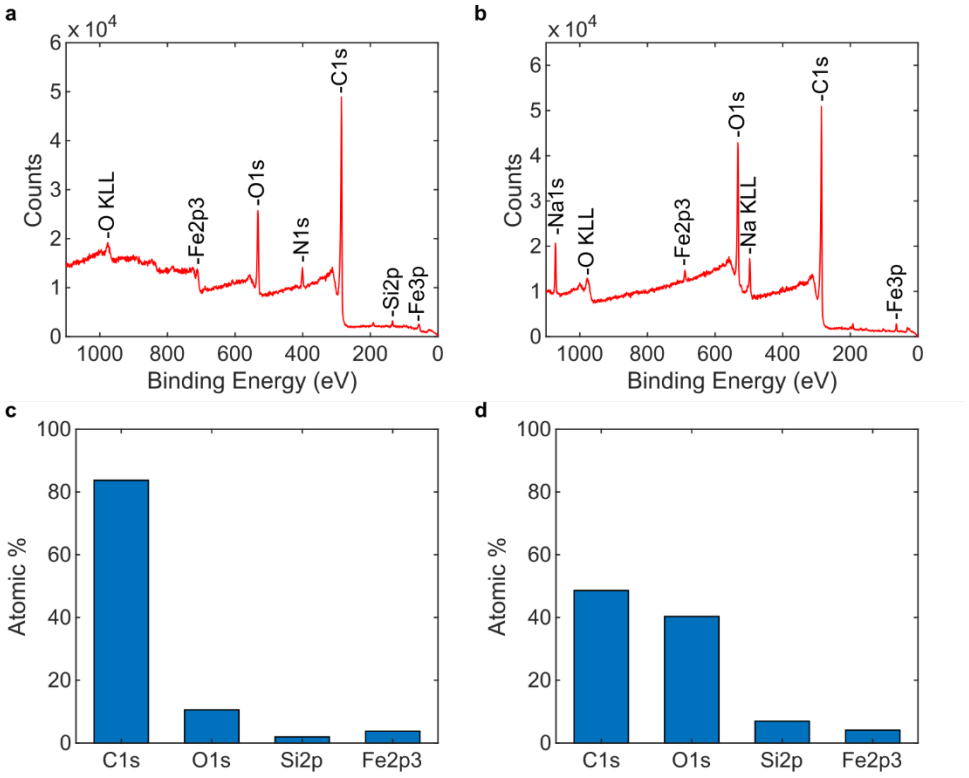

Figure A.4 XPS spectra of carbon nanotube stocks before and after heating. (a–b) XPS spectra of **(a)** untreated and **(b)** 2.5 h 250°C heat treated (under N_2) HiPCO SWCNT. Notable peaks are identified. **(b–c)** Deconvolution of spectra into relative atomic quantities with respect to atomic orbital binding modes. Samples are **(c)** untreated and **(d)** heat treated.

We further collected high-resolution spectra of O1s, Fe2p, and Fe3p vibrational modes to determine whether which element was predominantly affected by oxidation (**Figure A.5a–c**). These were deconvoluted into the different chemical states,[157–160] and the relative abundances were computed.

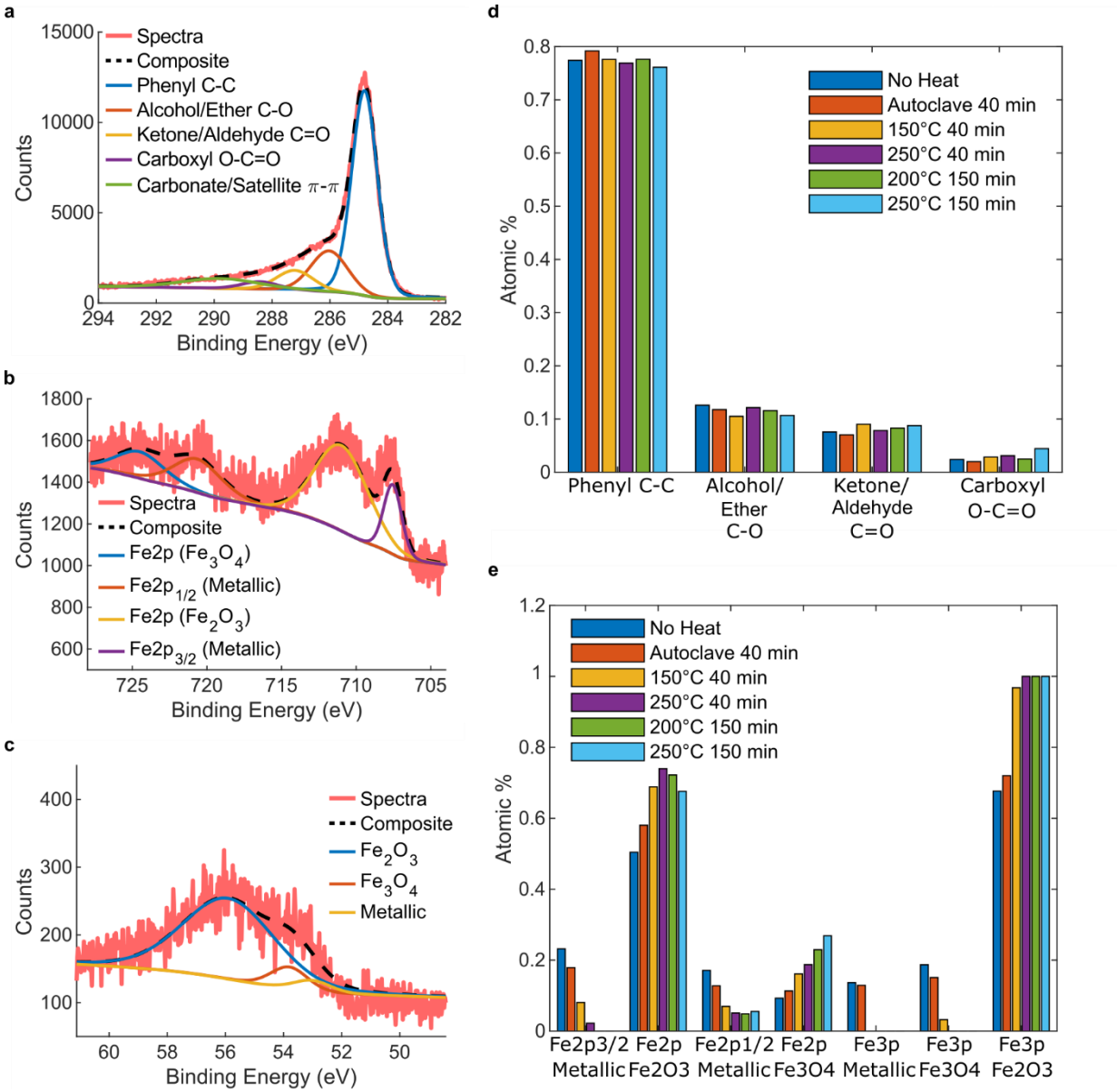

Figure A.5 High-resolution XPS spectra of O1s, Fe2p, and Fe3p vibrational modes. (a–c) High-resolution spectra of untreated, solid-phase HiPCO SWCNT for **(a)** C1s, **(b)** Fe2p, and **(c)** Fe3p vibrational modes. Spectra were deconvoluted into individual chemical components. Black dashed line indicates the summed spectra **(d–e)** Quantification of relative abundance for each chemical component with respect to the overall electron orbital signal for **(d)** C1s and **(e)** Fe2p and Fe3p orbitals.

The C1s deconvolution reveals no significant changes in carbon oxidation state (**Figure A.5d**). However, iron showed large increases in oxidation (**Figure A.5e**). Metallic Fe2p and Fe3p states were completely eliminated after 2.5 h at 250°C. This coincided with an increase in the relative atomic percentages of oxidized iron. In particular, Fe_2O_3 contribution of the Fe3p band reached 100% after heating at 250°C for only 40 min. Thus, while total oxygen content on the SWCNT surface increased dramatically upon heating, oxidation of residual iron catalyst was preferential over oxidation of the graphene lattice. Although the carbon lattice is maintained by heating, it is

unknown how the presence of iron oxides will affect SWCNT suspension properties. The conditions during the suspension process are crucial determinants of SWCNT surface density and photoluminescent properties.[161] Furthermore, the differential biological response observed for so-called 'decontaminated' MWCNTs may be due to oxidation of the SWCNT surface by heating in the presence of oxygen. Therefore, it is unknown how heating SWCNTs may impact downstream sensing or delivery applications.

While heat decontamination methods may marginally decrease endotoxin contamination in solid SWCNT stocks, the downsides of this method (e.g. alteration of the SWCNT surface chemistry) outweigh the benefits. Presently, sterile manufacturing processes for carbon nanomaterials are not yet widespread. Consequently, the most suitable approach for most laboratories working with carbon nanotubes is to prevent downstream bacterial contamination using sterile handing protocols in conjunction with containment systems.[162] LAL assay testing of carbon nanotube suspensions can then be used to ensure that beneath an acceptable threshold or the assay's limit of detection, where the latter limit is partially imposed by nanotube induced assay activation.

Appendix B:
Adsorption of Cell Lysate Proteins to SWCNT

Herein, we attempt to characterize the composition of the SWCNT corona phase in the presence of a protein rich biofluid. The following data are from initial experiments aimed at determining whether preferential adsorption of proteins can disproportionately favor proteins involved in specific cellular components and/or biological processes. To accomplish this, the pull-down assay for SWCNT protein corona characterization developed by Pinals *et al.* was performed using SIM-A9 cell lysate as the biofluid.[113] Lysate was prepared by adding 3 mL Native lysis buffer (Abcam) to approximately 5.0 x 10^6 cells on a 150 mm dish. Lysate was centrifuged at 1,000 rcf for 5 min to pellet cell debris. The supernatant was added to 100 µg/mL $(GT)_6$-SWCNTs in a 1:1 volume ratio and the resulting mixture was incubated for 1 h at room temperature causing formation of a protein corona and aggregation of SWCNTs. Protein corona was characterized as previously described (see **3.7 Materials and Methods**). Mass spectrometry analysis of the corona composition resulted in identification of 1,281 unique protein species, 171 of which were not detected in the lysate control (**Figure B.1**). This subset of proteins was highly *enriched* by adsorption to the SWCNT surface to concentrations greater than the protein mass spectrometry limit of detection. Furthermore, 2 proteins were identified in lysate but not found in appreciable concentrations on the SWCNT corona. These proteins were *depleted* relative to the lysate only control.

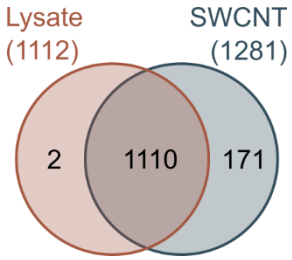

Figure B.1 Number of unique proteins identified in SIM-A9 cell lysate vs. SWCNT corona. Proteins identified by mass spectroscopy in SIM-A9 cell lysate compared to proteins extracted $(GT)_6$-SWCNT corona phase after 1 h incubation.

To gain an understanding of the overall corona composition, we identify the most highly abundant proteins in the $(GT)_6$-SWCNT corona phase following incubation in SIM-A9 microglial cell lysate (**Table B.1**). The 25 most prevalent proteins comprise 35.6% of the corona phase in terms of molar concentrations. Of these 25 proteins, 8 are nuclear proteins including 4th ranked nucleophosmin, a nucleic acid binding protein found in the nucleolus. Furthermore, 3 mitochondrial proteins were identified. DNA-wrapped SWCNTs are not thought to internalize within the nucleus or the mitochondrion of mammalian cells.[106,114] Therefore, these proteins are not expected to be in the protein corona of SWCNTs in a live tissue culture. Nevertheless, biologically relevant stress response proteins such as clusterin and heat shock proteins are also

identified in high abundance on the SWCNT surface following incubation in lysate. Hence, while this large dataset is primarily representative of corona formation in a complex and diverse protein mixture, it may contain valuable insights into cellular components which contain proteins of high affinity to the SWCNT surface and warrants further investigation.

Table B.1 Top 25 most abundant SIM-A9 lysate proteins in $(GT)_6$-SWCNT corona.

Rank	Protein
1	Glyceraldehyde-3-phosphate dehydrogenase
2	Elongation factor 1-alpha 1
3	Alpha-enolase
4	Nucleophosmin
5	Actin, cytoplasmic 1
6	Nucleolin
7	60S ribosomal protein
8	Polyadenylate-binding protein 1
9	ATP synthase subunit alpha, mitochondrial
10	Heterogeneous nuclear ribonucleoprotein K
11	Heterogeneous nuclear ribonucleoprotein U
12	Heat shock cognate 71 kDa protein
13	40S ribosomal protein S17
14	Ras GTPase-activating-like protein IQGAP1
15	Receptor of activated protein C kinase 1
16	60 kDa heat shock protein, mitochondrial
17	60S ribosomal protein L3
18	60S ribosomal protein L23
19	Heterogeneous nuclear ribonucleoprotein Q
20	Nucleolar protein 58
21	40S ribosomal protein S6
22	Heterogeneous nuclear ribonucleoprotein F
23	ATP synthase subunit beta, mitochondrial
24	Heterogeneous nuclear ribonucleoprotein A/B
25	40S ribosomal protein S7

The 1,110 commonly identified proteins were compared in terms of the protein abundance from corona sample vs. lysate alone (**Figure B.2a**). The degree of enrichment/depletion or fold change was defined as the ratio of normalized corona protein concentration to normalized lysate protein concentration. The majority of proteins show positive enrichment from SWCNT adsorption (fold change > 1) which points to the importance of low concentration proteins in the formation of the protein corona. A two-way ANOVA was used to determine the p value of enrichment/depletion for each protein. Plotting the negative $\log_{10}$ of the p value against the concentration $\log_2$ fold change reveals a biased subset of proteins with low statistical significance

despite relatively high $\log_2$ fold change (**Figure B.2b**). This trend was not observed in subsequent mass spectrometry analyses (see **Figure 3.8c–d** and **Figure B.4**) and may arise from the exclusion of an internal protein control which was included in later experiments to allow for protein concentration quantification. Nevertheless, downstream data analysis utilized a $p < 0.05$ cutoff to identify significantly enriched or depleted proteins.

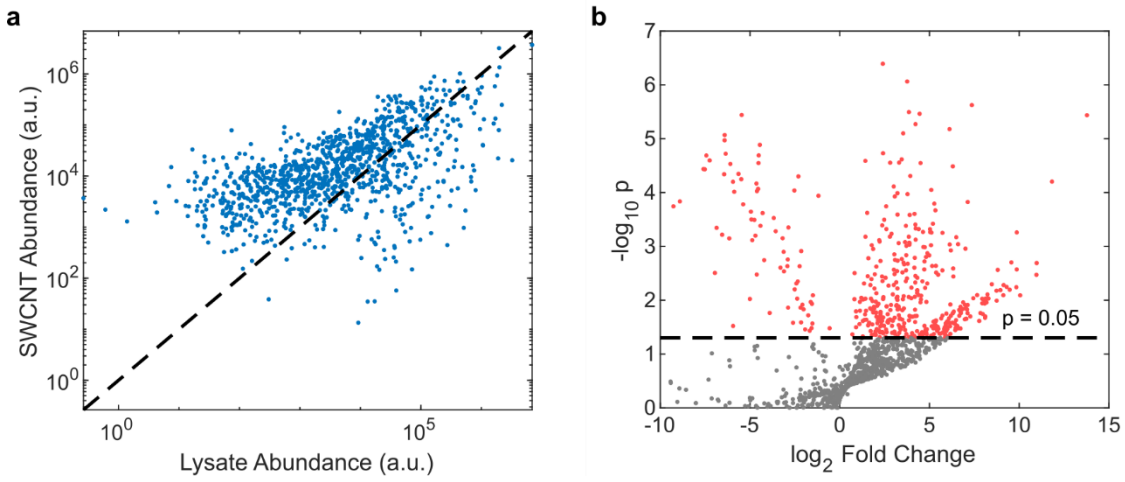

Figure B.2 Quantification of proteins identified from SWCNT corona pull-down assay vs. lysate alone. (a) Scatter plot of protein abundance in lysate control vs. in dissociated SWCNT corona. Protein concentrations are normalized to the total protein concentration in each sample. Each data point represents a protein identified in both SIM-A9 lysate and SWCNT corona. Proteins with zero or infinite enrichment are not shown. Dashed line represents enrichment fold change equal to 1. **(b)** Volcano plot of log fold change between protein abundance in corona over lysate alone vs. the negative log of p value calculated using a two-way ANOVA (N = 3). Dashed line represents a p value of 0.05. Proteins which were statistically significantly depleted or enriched are designated by red data points.

Next, the identified proteins were annotated with Gene Ontology (GO) cellular component terms using PANTHER[163] and protein lists were classified by the frequency of occurrence for these terms (**Figure B.3**). Three protein lists were analyzed: (1) all proteins found in the corona phase, (2) proteins which were enriched by SWCNT adsorption, and (3) proteins which were *statistically significantly* enriched. Change in the number of annotated proteins for each category from list (1) to list (3) may reflect enrichment of that cellular component within the SWCNT corona phase. Of note, organelle components showed an increase in representation among tightly adsorbed proteins whereas membrane proteins were less represented in latter data sets.

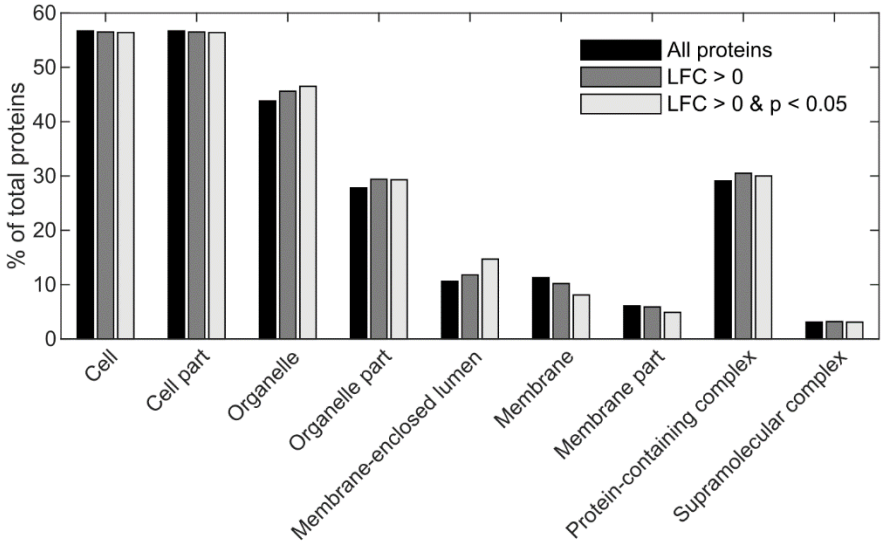

Figure B.3 Cellular component gene ontology terms represented by SWCNT protein corona. Top 9 most represented cellular component GO terms within lists of proteins found within the $(GT)_6$-SWCNT protein corona formed after incubation with SIM-A9 cell lysate. Protein lists comprise either all corona proteins identified (1281 total proteins), proteins which were enriched by adsorption to SWCNT (i.e. log fold change in protein concentration greater than 0, 1018 proteins), or (3) proteins underwent statistically significant enrichment ($p < 0.05$, 547 proteins). p values were calculated using a two-way ANOVA (N = 3).

Statistical analysis was performed in order to determine terms which showed significantly higher representation among the list of highly enriched corona proteins. An overrepresentation test was run using *topGO*[130] (Fisher's exact algorithm and false discovery rate correction) on GO cellular component terms (**Table B.2**). Three of the four significantly enriched terms corresponded to components within the cell nucleus: *Chromosome*, *Nucleolus*, and *Nuclear speck*. As such, upon exposure to a complex mixture of cellular proteins, $(GT)_6$-SWCNTs appear to preferentially adsorb proteins associated with the nucleus and mRNA processing in particular. Further research is required to determine whether this arises from specific interactions between these proteins and the SWCNT surface.

Table B.2 Significantly overrepresented GO cellular component terms by SWCNT corona proteins following cell lysate incubation

GO ID	Term	Annotated	Significant	Expected	p Value
GO:0005694	Chromosome	127	62	53.91	0.0002
GO:0005730	Nucleolus	155	83	65.79	0.0080
GO:0005762	Mitochondrial Large Ribosomal Subunit	32	20	13.58	0.0165
GO:0016607	Nuclear Speck	71	39	30.14	0.0199

To probe the corona formation process in a more biologically relevant cellular biofluid, we performed a similar experiment utilizing the supernatant of SIM-A9 cell tissue culture. Cells were

incubated in sera free DMEM/F12 media for 24 h before the supernatant containing secreted proteins was decanted and added to a suspension of 100 μg/mL $(GT)_6$-SWCNTs. Aggregated SWCNTs were pelleted and protein was extracted as detailed above. Mass spectrometry analysis revealed only 44 proteins of adequate concentration within the unaltered supernatant. Of these, 30 were present to a quantifiable degree in the SWCNT corona following desorption, the most abundant of which are listed below (**Table B.3**).

Table B.3 Top 25 most abundant SIM-A9 supernatant proteins in $(GT)_6$-SWCNT corona.

Rank	Protein
1	Galectin-3-binding protein
2	Nucleophosmin
3	Alpha-enolase
4	Clusterin
5	Nucleolin
6	Urokinase-type plasminogen activator
7	Heterogeneous nuclear ribonucleoprotein A/B
8	Myosin light polypeptide 6
9	Ran-specific GTPase-activating protein
10	H-2 class I histocompatibility antigen, Q10 alpha chain
11	Apolipoprotein E
12	Pyruvate kinase PKM
13	Stress-induced-phosphoprotein 1
14	Heat shock cognate 71 kDa protein
15	Endoplasmic reticulum resident protein 29
16	Peptidyl-prolyl cis-trans isomerase A
17	Actin, aortic smooth muscle
18	Heat shock protein HSP 90-beta
19	Cathepsin B
20	Heat shock protein HSP 90-alpha
21	Eukaryotic translation initiation factor 5A-1
22	Protein SET
23	Phosphoglycerate kinase 1
24	Serum albumin
25	Phosphoglycerate mutase 1

These results recapitulate findings from previous studies in which galectin-3-binding protein was both highly abundant and highly enriched (**Figure B.4**).[113] Furthermore, nucleophosmin, nucleolin, and clusterin were highly enriched by the SWCNT surface and were also highly abundant in the corona formed from cell lysate (**Figure B.4**). However, overrepresentation analysis using significantly enriched proteins from this dataset failed to reveal any significant GO terms represented. This may be due to the small reference subset of supernatant

proteins arising from the low concentrations of the SIM-A9 protein secretome and relatively high limit of detection of protein mass spectrometry.

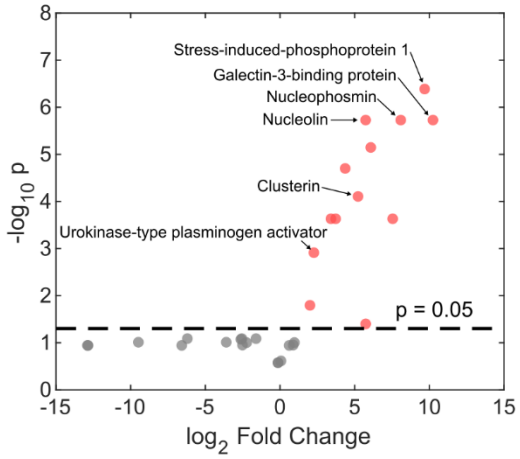

Figure B.4 Enrichment/depletion of SIM-A9 supernatant proteins in SWCNT corona phase. Volcano plot of log fold change between protein abundance in $(GT)_6$-SWCNT corona over supernatant alone vs. the negative log of p value calculated using a two-way ANOVA (N = 3). Dashed line represents a p value of 0.05. Proteins which were statistically significantly depleted or enriched are designated by red data points.

These experiments lay the groundwork for further proteomics studies in evaluating the biological impact of the SWCNT protein corona. Incubation of nanoparticles with these highly complex protein mixtures produces a surplus of quantitative compositional data. Further analysis using machine learning and other statistical analysis methods may also elucidate the thermodynamics and mechanisms by which proteins bind to the SWCNT surface.

References

(1) Beyene, A. G.; Delevich, K.; Del Bonis-O'Donnell, J. T.; Piekarski, D. J.; Lin, W. C.; Wren Thomas, A.; Yang, S. J.; Kosillo, P.; Yang, D.; Prounis, G. S.; Wilbrecht, L.; Landry, M. P. Imaging Striatal Dopamine Release Using a Nongenetically Encoded near Infrared Fluorescent Catecholamine Nanosensor. *Sci. Adv.* **2019**, *5* (7), 1–12.

(2) Jeong, S.; Yang, D.; Beyene, A. G.; Del Bonis-O'Donnell, J. T.; Gest, A. M. M.; Navarro, N.; Sun, X.; Landry, M. P. High-Throughput Evolution of near-Infrared Serotonin Nanosensors. *Sci. Adv.* **2019**, *5* (12), 1–13.

(3) Del Bonis-O'Donnell, J. T.; Beyene, A.; Chio, L.; Demirer, G.; Yang, D.; Landry, M. P. Engineering Molecular Recognition with Bio-Mimetic Polymers on Single Walled Carbon Nanotubes. *J. Vis. Exp.* **2017**, No. 119, 1–9.

(4) Zheng, Y.; Bachilo, S. M.; Weisman, R. B. Enantiomers of Single-Wall Carbon Nanotubes Show Distinct Coating Displacement Kinetics. *J. Phys. Chem. Lett.* **2018**, *9* (13), 3793–3797.

(5) Zheng, M.; Jagota, A.; Semke, E. D.; Diner, B. A.; McLean, R. S.; Lustig, S. R.; Richardson, R. E.; Tassi, N. G. DNA-Assisted Dispersion and Separation of Carbon Nanotubes. *Nat. Mater.* **2003**, *2* (5), 338–342.

(6) Hong, G.; Diao, S.; Chang, J.; Antaris, A. L.; Chen, C.; Zhang, B.; Zhao, S.; Atochin, D. N.; Huang, P. L.; Andreasson, K. I.; Kuo, C. J.; Dai, H. Through-Skull Fluorescence Imaging of the Brain in a New near-Infrared Window. *Nat. Photonics* **2014**, *8* (9), 723–730.

(7) Hong, G.; Antaris, A. L.; Dai, H. Near-Infrared Fluorophores for Biomedical Imaging. *Nat. Biomed. Eng.* **2017**, *1* (1), 0010.

(8) Giraldo, J. P.; Landry, M. P.; Kwak, S. Y.; Jain, R. M.; Wong, M. H.; Iverson, N. M.; Ben-Naim, M.; Strano, M. S. A Ratiometric Sensor Using Single Chirality Near-Infrared Fluorescent Carbon Nanotubes: Application to in Vivo Monitoring. *Small* **2015**, *11* (32), 3973–3984.

(9) Kruss, S.; Landry, M. P.; Vander Ende, E.; Lima, B. M. A.; Reuel, N. F.; Zhang, J.; Nelson, J.; Mu, B.; Hilmer, A.; Strano, M. Neurotransmitter Detection Using Corona Phase Molecular Recognition on Fluorescent Single-Walled Carbon Nanotube Sensors. *J. Am. Chem. Soc.* **2014**, *136* (2), 713–724.

(10) Kang, B. C.; Park, B. S.; Ha, T. J. Highly Sensitive Wearable Glucose Sensor Systems Based on Functionalized Single-Wall Carbon Nanotubes with Glucose Oxidase-Nafion Composites. *Appl. Surf. Sci.* **2019**, *470* (November 2018), 13–18.

(11) Bisker, G.; Dong, J.; Park, H. D.; Iverson, N. M.; Ahn, J.; Nelson, J. T.; Landry, M. P.; Kruss, S.; Strano, M. S. Protein-Targeted Corona Phase Molecular Recognition. *Nat. Commun.* **2016**, *7*, 10241.

(12) Beyene, A. G.; Alizadehmojarad, A. A.; Dorlhiac, G.; Goh, N.; Streets, A. M.; Král, P.; Vuković, L.; Landry, M. P. Ultralarge Modulation of Fluorescence by Neuromodulators in Carbon Nanotubes Functionalized with Self-Assembled Oligonucleotide Rings. *Nano Lett.* **2018**, *18* (11), 6995–7003.

(13) Kruss, S.; Salem, D. P.; Vukovi, L.; Lima, B.; Vander, E.; Boyden, E. S.; Strano, M. S. High-Resolution Imaging of Cellular Dopamine Efflux Using a Fluorescent Nanosensor Array. **2017**, *3*.

(14) Iverson, N. M.; Barone, P. W.; Shandell, M.; Trudel, L. J.; Sen, S.; Sen, F.; Ivanov, V.;

Atolia, E.; Farias, E.; McNicholas, T. P.; Reuel, N.; Parry, N. M. A.; Wogan, G. N.; Strano, M. S. In Vivo Biosensing via Tissue-Localizable near-Infrared-Fluorescent Single-Walled Carbon Nanotubes. *Nat. Nanotechnol.* **2013**, *8* (11), 873–880.

(15) Chio, L.; Yang, D.; Landry, M. Surface Engineering of Nanoparticles to Create Synthetic Antibodies. **2017**, *1575*, 363–380. https://doi.org/10.1007/978-1-4939-6857-2.

(16) Zhu, Z.; Garcia-Gancedo, L.; Flewitt, A. J.; Xie, H.; Moussy, F.; Milne, W. I. A Critical Review of Glucose Biosensors Based on Carbon Nanomaterials: Carbon Nanotubes and Graphene. *Sensors (Switzerland)* **2012**, *12* (5), 5996–6022.

(17) Puig, M. V.; Rose, J.; Schmidt, R.; Freund, N. Dopamine Modulation of Learning and Memory in the Prefrontal Cortex: Insights from Studies in Primates, Rodents, and Birds. *Front. Neural Circuits* **2014**, *8* (AUG), 1–15.

(18) Martorana, A.; Koch, G. Is Dopamine Involved in Alzheimer's Disease? *Front. Aging Neurosci.* **2014**, *6* (SEP), 1–6.

(19) Beyene, A. G.; McFarlane, I. R.; Pinals, R. L.; Landry, M. P. Stochastic Simulation of Dopamine Neuromodulation for Implementation of Fluorescent Neurochemical Probes in the Striatal Extracellular Space. *ACS Chem. Neurosci.* **2017**, *8* (10), 2275–2289.

(20) Sun, F.; Zeng, J.; Jing, M.; Zhou, J.; Feng, J.; Owen, S. F.; Luo, Y.; Li, F.; Wang, H.; Yamaguchi, T.; Yong, Z.; Gao, Y.; Peng, W.; Wang, L.; Zhang, S.; Du, J.; Lin, D.; Xu, M.; Kreitzer, A. C.; Cui, G.; Li, Y. A Genetically Encoded Fluorescent Sensor Enables Rapid and Specific Detection of Dopamine in Flies, Fish, and Mice. *Cell* **2018**, *174* (2), 481-496.e19.

(21) Beyene, A. G.; Yang, S. J.; Landry, M. P. Tools and Trends for Probing Brain Neurochemistry. *J. Vac. Sci. Technol. A* **2019**, *37* (4), 040802.

(22) Pinals, R. L.; Yang, D.; Lui, A.; Cao, W.; Landry, M. P. Corona Exchange Dynamics on Carbon Nanotubes by Multiplexed Fluorescence Monitoring. *J. Am. Chem. Soc.* **2020**, *142*, 1254–1264.

(23) Yang, D.; Yang, S. J.; Travis, J.; Donnell, D. B.; Pinals, R. L.; Landry, M. P. Mitigation of Carbon Nanotube Neurosensor Induced Transcriptomic and Morphological Changes in Mouse Microglia with Surface Passivation. *ACS Nano* **2020**. https://doi.org/10.1021/acsnano.0c06154.

(24) Zhang, J.; Landry, M. P.; Barone, P. W.; Kim, J. H.; Lin, S.; Ulissi, Z. W.; Lin, D.; Mu, B.; Boghossian, A. A.; Hilmer, A. J.; Rwei, A.; Hinckley, A. C.; Kruss, S.; Shandell, M. A.; Nair, N.; Blake, S.; Şen, F.; Şen, S.; Cray, R. G.; Li, D.; Yum, K.; Ahn, J. H.; Jin, H.; Heller, D. A.; Essigmann, J. M.; Blankschtein, D.; Strano, M. S. Molecular Recognition Using Corona Phase Complexes Made of Synthetic Polymers Adsorbed on Carbon Nanotubes. *Nat. Nanotechnol.* **2013**, *8* (November), 959–968.

(25) Liu, Z.; Tabakman, S.; Welsher, K.; Dai, H. Carbon Nanotubes in Biology and Medicine: In Vitro and in Vivo Detection, Imaging and Drug Delivery. *Nano Res.* **2009**, *2* (2), 85–120.

(26) Demirer, G. S.; Zhang, H.; Matos, J. L.; Goh, N. S.; Cunningham, F. J.; Sung, Y.; Chang, R.; Aditham, A. J.; Chio, L.; Cho, M. J.; Staskawicz, B.; Landry, M. P. High Aspect Ratio Nanomaterials Enable Delivery of Functional Genetic Material without DNA Integration in Mature Plants. *Nat. Nanotechnol.* **2019**, *14* (5), 456–464.

(27) Marchesan, S.; Prato, M. Under the Lens: Carbon Nanotube and Protein Interaction at the Nanoscale. *Chem. Commun.* **2015**, *51* (21), 4347–4359.

(28) Cedervall, T.; Lynch, I.; Lindman, S.; Berggård, T.; Thulin, E.; Nilsson, H.; Dawson, K. A.; Linse, S. Understanding the Nanoparticle-Protein Corona Using Methods to Quntify

Exchange Rates and Affinities of Proteins for Nanoparticles. *Proc. Natl. Acad. Sci. U. S. A.* **2007**, *104* (7), 2050–2055.
(29) Nel, A. E.; Mädler, L.; Velegol, D.; Xia, T.; Hoek, E. M. V.; Somasundaran, P.; Klaessig, F.; Castranova, V.; Thompson, M. Understanding Biophysicochemical Interactions at the Nano-Bio Interface. *Nat. Mater.* **2009**, *8* (7), 543–557.
(30) Gravely, M.; Safaee, M. M.; Roxbury, D. Biomolecular Functionalization of a Nanomaterial to Control Stability and Retention within Live Cells. *Nano Lett.* **2019**, *19* (9), 6203–6212.
(31) Bisker, G.; Bakh, N. A.; Lee, M. A.; Ahn, J.; Park, M.; O'Connell, E. B.; Iverson, N. M.; Strano, M. S. Insulin Detection Using a Corona Phase Molecular Recognition Site on Single-Walled Carbon Nanotubes. *ACS Sensors* **2018**, *3* (2), 367–377.
(32) Djit, J. C.; Cohen Stuart, M. A.; Fleer, G. . Competitive Adsorption Kinetics of Polymers Differing in Length Only. *Macromolecules* **1994**, *27*, 3219–3228.
(33) Landry, M. P.; Vuković, L.; Kruss, S.; Bisker, G.; Landry, A. M.; Islam, S.; Jain, R.; Schulten, K.; Strano, M. S. Comparative Dynamics and Sequence Dependence of DNA and RNA Binding to Single Walled Carbon Nanotubes. *J. Phys. Chem. C* **2015**, *119* (18), 10048–10058.
(34) Silvera-Batista, C. A.; Wang, R. K.; Weinberg, P.; Ziegler, K. J. Solvatochromic Shifts of Single-Walled Carbon Nanotubes in Nonpolar Microenvironments. *Phys. Chem. Chem. Phys.* **2010**, *12* (26), 6990–6998.
(35) Larsen, B. A.; Deria, P.; Holt, J. M.; Stanton, I. N.; Heben, M. J.; Therien, M. J.; Blackburn, J. L. Effect of Solvent Polarity and Electrophilicity on Quantum Yields and Solvatochromic Shifts of Single-Walled Carbon Nanotube Photoluminescence. *J. Am. Chem. Soc.* **2012**, *134* (30), 12485–12491.
(36) Choi, J. H.; Strano, M. S. Solvatochromism in Single-Walled Carbon Nanotubes. *Appl. Phys. Lett.* **2007**, *90* (22), 88–91.
(37) Oh, H.; Sim, J.; Ju, S. Y. Binding Affinities and Thermodynamics of Noncovalent Functionalization of Carbon Nanotubes with Surfactants. *Langmuir* **2013**, *29* (35), 11154–11162.
(38) Harvey, J. D.; Jena, P. V.; Baker, H. A.; Zerze, G. H.; Williams, R. M.; Galassi, T. V.; Roxbury, D.; Mittal, J.; Heller, D. A. A Carbon Nanotube Reporter of MicroRNA Hybridization Events in Vivo. *Nat. Biomed. Eng.* **2017**, *1* (March), 0041.
(39) Shankar, A.; Mittal, J.; Jagota, A. Binding between DNA and Carbon Nanotubes Strongly Depends upon Sequence and Chirality. *Langmuir* **2014**, *30* (11), 3176–3183.
(40) Roxbury, D.; Tu, X.; Zheng, M.; Jagota, A. Recognition Ability of DNA for Carbon Nanotubes Correlates with Their Binding Affinity. *Langmuir* **2011**, *27* (13), 8282–8293.
(41) Jena, P. V.; Safaee, M. M.; Heller, D. A.; Roxbury, D. DNA-Carbon Nanotube Complexation Affinity and Photoluminescence Modulation Are Independent. *ACS Appl. Mater. Interfaces* **2017**. https://doi.org/10.1021/acsami.7b05678.
(42) Jeng, E. S.; Moll, A. E.; Roy, A. C.; Gastala, J. B.; Strano, M. S. Detection of DNA Hybridization Using the Near-Infrared Band-Gap Fluorescence of Single-Walled Carbon Nanotubes. *Nano Lett.* **2006**, *6* (3), 371–375.
(43) Barone, P. W.; Baik, S.; Heller, D. A.; Strano, M. S. Near-Infrared Optical Sensors Based on Single-Walled Carbon Nanotubes. *Nat. Mater.* **2005**, *4* (1), 86–92.
(44) Zhu, Z.; Yang, R.; You, M.; Zhang, X.; Wu, Y.; Tan, W. Single-Walled Carbon Nanotube as an Effective Quencher. *Anal. Bioanal. Chem.* **2010**, *396* (1), 73–83.
(45) Umemura, K.; Sato, S.; Bustamante, G.; Ye, J. Y. Using a Fluorescence Quenching Method

to Detect DNA Adsorption onto Single-Walled Carbon Nanotube Surfaces. *Colloids Surfaces B Biointerfaces* **2017**, *160*, 201–206.
(46) Anderson, N. L.; Anderson, N. G. The Human Plasma Proteome: History, Character, and Diagnostic Prospects. *Mol. Cell. Proteomics* **2002**, *1* (11), 845–867.
(47) Lowe, G. D. O.; Rumley, A.; Mackie, I. J. Plasma Fibrinogen. *Ann Clin Biochem* **2004**, *41*, 430–440.
(48) Foroozandeh, P.; Aziz, A. A. Merging Worlds of Nanomaterials and Biological Environment: Factors Governing Protein Corona Formation on Nanoparticles and Its Biological Consequences. *Nanoscale Res. Lett.* **2015**, *10* (1).
(49) Monopoli, M. P.; Walczyk, D.; Campbell, A.; Elia, G.; Lynch, I.; Baldelli Bombelli, F.; Dawson, K. A. Physical-Chemical Aspects of Protein Corona: Relevance to in Vitro and in Vivo Biological Impacts of Nanoparticles. *J. Am. Chem. Soc.* **2011**, *133* (8), 2525–2534.
(50) Lundqvist, M.; Stigler, J.; Elia, G.; Lynch, I.; Cedervall, T.; Dawson, K. a. Nanoparticle Size and Surface Properties Determine the Protein Corona with Possible Implications for Biological Impacts. *Proc. …* **2008**, *105* (38), 14265–14270.
(51) Brunecker, F. K.; Schöppler, F.; Hertel, T. Interaction of Polymers with Single-Wall Carbon Nanotubes. *J. Phys. Chem. C* **2016**, *120* (18), 10094–10103.
(52) Lu, N.; Sui, Y.; Tian, R.; Peng, Y. Y. Adsorption of Plasma Proteins on Single-Walled Carbon Nanotubes Reduced Cytotoxicity and Modulated Neutrophil Activation. *Chem. Res. Toxicol.* **2018**, *31* (10), 1061–1068.
(53) Salvador-Morales, C.; Flahaut, E.; Sim, E.; Sloan, J.; Green, M. L. H.; Sim, R. B. Complement Activation and Protein Adsorption by Carbon Nanotubes. *Mol. Immunol.* **2006**, *43* (3), 193–201.
(54) Ge, C.; Du, J.; Zhao, L.; Wang, L.; Liu, Y.; Li, D.; Yang, Y.; Zhou, R.; Zhao, Y.; Chai, Z.; Chen, C. Binding of Blood Proteins to Carbon Nanotubes Reduces Cytotoxicity. *Proc. Natl. Acad. Sci. U. S. A.* **2011**, *108* (41), 16968–16973.
(55) Wertz, C. F.; Santore, M. M. Adsorption and Relaxation Kinetics of Albumin and Fibrinogen on Hydrophobic Surfaces: Single-Species and Competitive Behavior. *Langmuir* **1999**, *15* (26), 8884–8894.
(56) Mubarekyan, E.; Santore, M. M. Adsorption and Exchange Dynamics in Aging Hydroxyethylcellulose Layers on Silica. *J. Colloid Interface Sci.* **2000**, *227* (2), 334–344.
(57) Wertz, C. F.; Santore, M. M. Effect of Surface Hydrophobicity on Adsorption and Relaxation Kinetics of Albumin and Fibrinogen: Single-Species and Competitive Behavior. *Langmuir* **2001**, *17* (10), 3006–3016.
(58) Jungbauer, L. M.; Yu, C.; Laxton, K. J.; LaDu, M. J. Preparation of Fluorescently-Labeled Amyloid-Beta Peptide Assemblies: The Effect of Fluorophore Conjugation on Structure and Function. *J. Mol. Recognit.* **2009**, *22* (5), 403–413.
(59) Albertorio, F.; Hughes, M. E.; Golovchenko, J. A.; Branton, D. Base Dependent DNA-Carbon Nanotube Interactions: Activation Enthalpies and Assembly-Disassembly Control. *Nanotechnology* **2009**, *20* (39), 211–220.
(60) Röcker, C.; Pötzl, M.; Zhang, F.; Parak, W. J.; Nienhaus, G. U. A Quantitative Fluorescence Study of Protein Monolayer Formation on Colloidal Nanoparticles. *Nat. Nanotechnol.* **2009**, *4* (9), 577–580.
(61) Djit, J. C.; Stuart Cohen, M. A.; Fleer, G. J. Surface Exchange Kinetics of Chemically Different Polymers. *Macromolecules* **1994**, *27* (12), 3229–3237.
(62) Latour, R. A. The Langmuir Isotherm: A Commonly Applied but Misleading Approach for

the Analysis of Protein Adsorption Behavior. *J. Biomed. Mater. Res. - Part A* **2015**, *103* (3), 949–958.
(63) De Paoli, S. H.; Diduch, L. L.; Tegegn, T. Z.; Orecna, M.; Strader, M. B.; Karnaukhova, E.; Bonevich, J. E.; Holada, K.; Simak, J. The Effect of Protein Corona Composition on the Interaction of Carbon Nanotubes with Human Blood Platelets. *Biomaterials* **2014**, *35* (24), 6182–6194.
(64) Tenzer, S.; Docter, D.; Kuharev, J.; Musyanovych, A.; Fetz, V.; Hecht, R.; Schlenk, F.; Fischer, D.; Kiouptsi, K.; Reinhardt, C.; Landfester, K.; Schild, H.; Maskos, M.; Knauer, S. K.; Stauber, R. H. Rapid Formation of Plasma Protein Corona Critically Affects Nanoparticle Pathophysiology. *Nat. Nanotechnol.* **2013**, *8* (10), 772–781.
(65) Chio, L.; Del Bonis-O'Donnell, J. T.; Kline, M. A.; Kim, J. H.; McFarlane, I. R.; Zuckermann, R. N.; Landry, M. P. Electrostatic Assemblies of Single-Walled Carbon Nanotubes and Sequence-Tunable Peptoid Polymers Detect a Lectin Protein and Its Target Sugars. *Nano Lett.* **2019**, *19* (11), 7563–7572.
(66) Godin, A. G.; Varela, J. A.; Gao, Z.; Danné, N.; Dupuis, J. P.; Lounis, B.; Groc, L.; Cognet, L. Single-Nanotube Tracking Reveals the Nanoscale Organization of the Extracellular Space in the Live Brain. *Nat. Nanotechnol.* **2017**, *12* (3), 238–243.
(67) Nißler, R.; Mann, F. A.; Chaturvedi, P.; Horlebein, J.; Meyer, D.; Vukovic, L.; Kruss, S. Quantification of the Number of Adsorbed DNA Molecules on Single-Walled Carbon Nanotubes. *J. Phys. Chem. C* **2019**. https://doi.org/10.1021/acs.jpcc.8b11058.
(68) Schöppler, F.; Mann, C.; Hain, T. C.; Neubauer, F. M.; Privitera, G.; Bonaccorso, F.; Chu, D.; Ferrari, A. C.; Hertel, T. Molar Extinction Coefficient of Single-Wall Carbon Nanotubes. *J. Phys. Chem. C* **2011**, *115* (30), 14682–14686.
(69) Roxbury, D.; Jena, P. V.; Shamay, Y.; Horoszko, C. P.; Heller, D. A. Cell Membrane Proteins Modulate the Carbon Nanotube Optical Bandgap via Surface Charge Accumulation. *ACS Nano* **2016**, *10* (1), 499–506.
(70) Moore, V. C.; Strano, M. S.; Haroz, E. H.; Hauge, R. H.; Smalley, R. E.; Schmidt, J.; Talmon, Y. Individually Suspended Single-Walled Carbon Nanotubes in Various Surfactants. *Nano Lett.* **2003**, *3* (10), 1379–1382.
(71) Okazaki, T.; Saito, T.; Matsuura, K.; Ohshima, S.; Yumura, M.; Iijima, S. Photoluminescence Mapping of "as-Grown" Single-Walled Carbon Nanotubes: A Comparison with Micelle-Encapsulated Nanotube Solutions. *Nano Lett.* **2005**, *5* (12), 2618–2623.
(72) Gill, S. C.; von Hippel, P. H. Calculation of Protein Extinction Coefficients from Amino Acid Sequence Data [Published Erratum Appears in Anal Biochem 1990 Sep;189(2):283]. *Anal Biochem* **1989**, *182* (2), 319–326.
(73) Marder, V. J.; Shulman, N. R. High Molecular Weight Derivatives of Human Fibrinogen Produced by Plasmin. *J. Biol. Chem.* **1969**, *244* (8), 2120–2125.
(74) Laemmli, U. K. Cleavage of Structural Proteins during the Assembly of the Head of Bacteriophage T4. *Nature* **1970**, *227* (5259), 680–685.
(75) Flory, P. J. *Principles of Polymer Chemistry*; Cornell University Press, 1953.
(76) Nam, K. T.; Shelby, S. A.; Choi, P. H.; Marciel, A. B.; Chen, R.; Tan, L.; Chu, T. K.; Mesch, R. A.; Lee, B. C.; Connolly, M. D.; Kisielowski, C.; Zuckermann, R. N. Free-Floating Ultrathin Two-Dimensional Crystals from Sequence-Specific Peptoid Polymers. *Nat. Mater.* **2010**, *9* (5), 454–460.
(77) Kang, M.; Jung, S.; Zhang, H.; Kang, T.; Kang, H.; Yoo, Y.; Hong, J. P.; Ahn, J. P.; Kwak,

J.; Jeon, D.; Kotov, N. A.; Kim, B. Subcellular Neural Probes from Single-Crystal Gold Nanowires. *ACS Nano* **2014**, *8* (8), 8182–8189. https://doi.org/10.1021/nn5024522.

(78) Patil, A. C.; Thakor, N. V. Implantable Neurotechnologies: A Review of Micro- and Nanoelectrodes for Neural Recording. *Med. Biol. Eng. Comput.* **2016**, *54* (1), 23–44.

(79) Zhang, S.; Song, Y.; Wang, M.; Xiao, G.; Gao, F.; Li, Z.; Tao, G.; Zhuang, P.; Yue, F.; Chan, P.; Cai, X. Real-Time Simultaneous Recording of Electrophysiological Activities and Dopamine Overflow in the Deep Brain Nuclei of a Non-Human Primate with Parkinson's Disease Using Nano-Based Microelectrode Arrays. *Microsystems Nanoeng.* **2018**, *4* (1), 1–9.

(80) Nance, E. A.; Woodworth, G. F.; Sailor, K. A.; Shih, T. Y.; Xu, Q.; Swaminathan, G.; Xiang, D.; Eberhart, C.; Hanes, J. A Dense Poly(Ethylene Glycol) Coating Improves Penetration of Large Polymeric Nanoparticles within Brain Tissue. *Sci. Transl. Med.* **2012**, *4* (149).

(81) Yang, H. Nanoparticle-Mediated Brain-Specific Drug Delivery, Imaging, and Diagnosis. *Pharm. Res.* **2010**, *27* (9), 1759–1771.

(82) Hrabetova, S.; Cognet, L.; Rusakov, D. A.; Nägerl, U. V. Unveiling the Extracellular Space of the Brain: From Super-Resolved Microstructure to in Vivo Function. *J. Neurosci.* **2018**, *38* (44), 9355–9363.

(83) Keefer, E. W.; Botterman, B. R.; Romero, M. I.; Rossi, A. F.; Gross, G. W. Carbon Nanotube Coating Improves Neuronal Recordings. *Nat. Nanotechnol.* **2008**, *3* (7), 434–439.

(84) Schmidt, A. C.; Wang, X.; Zhu, Y.; Sombers, L. A. Carbon Nanotube Yarn Electrodes for Enhanced Detection of Neurotransmitter Dynamics in Live Brain Tissue. *ACS Nano* **2013**, *7* (9), 7864–7873.

(85) Mohy-Ud-Din, Z.; Woo, S. H.; Kim, J. H.; Cho, J. H. Optoelectronic Stimulation of the Brain Using Carbon Nanotubes. *Ann. Biomed. Eng.* **2010**, *38* (11), 3500–3508.

(86) Beyene, A. G.; Delevich, K.; Yang, S. J.; Landry, M. P. New Optical Probes Bring Dopamine to Light. *Biochemistry* **2018**, *57* (45), 6379–6381.

(87) Long, T. C.; Saleh, N.; Tilton, R. D.; Lowry, G. V.; Veronesi, B. Titanium Dioxide (P25) Produces Reactive Oxygen Species in Immortalized Brain Microglia (BV2): Implications for Nanoparticle Neurotoxicity. *Environ. Sci. Technol.* **2006**, *40* (14), 4346–4352.

(88) Albanese, A.; Sykes, E. A.; Chan, W. C. W. Rough around the Edges: The Inflammatory Response of Microglial Cells to Spiky Nanoparticles. *ACS Nano* **2010**, *4* (5), 2490–2493.

(89) Xue, Y.; Wu, J.; Sun, J. Four Types of Inorganic Nanoparticles Stimulate the Inflammatory Reaction in Brain Microglia and Damage Neurons in Vitro. *Toxicol. Lett.* **2012**, *214* (2), 91–98.

(90) Graeber, M. B.; Streit, W. J. Microglia: Biology and Pathology. *Acta Neuropathol.* **2010**, *119* (1), 89–105.

(91) Hines, D. J.; Hines, R. M.; Mulligan, S. J.; Macvicar, B. A. Microglia Processes Block the Spread of Damage in the Brain and Require Functional Chloride Channels. *Glia* **2009**, *57* (15), 1610–1618.

(92) Mukandala, G.; Tynan, R.; Lanigan, S.; O'Connor, J. J. The Effects of Hypoxia and Inflammation on Synaptic Signaling in the CNS. *Brain Sci.* **2016**, *6* (1).

(93) Treadway, M. T.; Cooper, J. A.; Miller, A. H. Can't or Won't? Immunometabolic Constraints on Dopaminergic Drive. *Trends Cogn. Sci.* **2019**, *23* (5), 435–448.

(94) Villegas, J. C.; Álvarez-Montes, L.; Rodríguez-Fernández, L.; González, J.; Valiente, R.; Fanarraga, M. L. Multiwalled Carbon Nanotubes Hinder Microglia Function Interfering

with Cell Migration and Phagocytosis. *Adv. Healthc. Mater.* **2014**, *3* (3), 424–432.
(95) Shigemoto-Mogami, Y.; Hoshikawa, K.; Hirose, A.; Sato, K. Phagocytosis-Dependent and Independent Mechanisms Underlie the Microglial Cell Damage Caused by Carbon Nanotube Agglomerates. *J. Toxicol. Sci.* **2016**, *41* (4), 501–509.
(96) Nagamoto-Combs, K.; Kulas, J.; Combs, C. K. A Novel Cell Line from Spontaneously Immortalized Murine Microglia. *J Neurosci Methods* **2014**, No. Serres 1985, 759–785.
(97) Jeong, H.-K.; Ji, K.; Min, K.; Joe, E.-H. Brain Inflammation and Microglia: Facts and Misconceptions. *Exp. Neurobiol.* **2013**, *22* (2), 59.
(98) Fernández-Arjona, M. del M.; Grondona, J. M.; Fernández-Llebrez, P.; López-Ávalos, M. D. Microglial Morphometric Parameters Correlate With the Expression Level of IL-1β, and Allow Identifying Different Activated Morphotypes. *Front. Cell. Neurosci.* **2019**, *13* (October), 1–15.
(99) Bernier, L. P.; Bohlen, C. J.; York, E. M.; Choi, H. B.; Kamyabi, A.; Dissing-Olesen, L.; Hefendehl, J. K.; Collins, H. Y.; Stevens, B.; Barres, B. A.; MacVicar, B. A. Nanoscale Surveillance of the Brain by Microglia via CAMP-Regulated Filopodia. *Cell Rep.* **2019**, *27* (10), 2895-2908.
(100) Mukherjee, S. P.; Bondarenko, O.; Kohonen, P.; Andón, F. T.; Brzicová, T.; Gessner, I.; Mathur, S.; Bottini, M.; Calligari, P.; Stella, L.; Kisin, E.; Shvedova, A.; Autio, R.; Salminen-Mankonen, H.; Lahesmaa, R.; Fadeel, B. Macrophage Sensing of Single-Walled Carbon Nanotubes via Toll-like Receptors. *Sci. Rep.* **2018**, *8* (1), 1–17.
(101) Ritter, N.; Cooper, J. New Resolution Independent Measures of Circularity. *J. Math. Imaging Vis.* **2009**, *35* (2), 117–127.
(102) Yaron, P. N.; Holt, B. D.; Short, P. A.; Lösche, M.; Islam, M. F.; Dahl, K. N. Single Wall Carbon Nanotubes Enter Cells by Endocytosis and Not Membrane Penetration. *J. Nanobiotechnology* **2011**, *9* (1), 45.
(103) Maruyama, K.; Haniu, H.; Saito, N.; Matsuda, Y.; Tsukahara, T.; Kobayashi, S.; Tanaka, M.; Aoki, K.; Takanashi, S.; Okamoto, M.; Kato, H. Endocytosis of Multiwalled Carbon Nanotubes in Bronchial Epithelial and Mesothelial Cells. *Biomed Res. Int.* **2015**, *2015*.
(104) Kettler, K.; Veltman, K.; van de Meent, D.; van Wezel, A.; Hendriks, A. J. Cellular Uptake of Nanoparticles as Determined by Particle Properties, Experimental Conditions, and Cell Type. *Environ. Toxicol. Chem.* **2014**, *33* (3), 481–492.
(105) Jin, H.; Heller, D. a; Sharma, R.; Strano, M. S. Size-Dependent Cellular Uptake and Expulsion of Single-Walled Carbon Nanotubes : Single Particle Tracking and Nanoparticles. *ACS Nano* **2009**, *3* (1), 149–158.
(106) Budhathoki-Uprety, J.; Langenbacher, R. E.; Jena, P. V.; Roxbury, D.; Heller, D. A. A Carbon Nanotube Optical Sensor Reports Nuclear Entry via a Noncanonical Pathway. *ACS Nano* **2017**, *11* (4), 3875–3882.
(107) Tîlmaciu, C.-M.; Morris, M. C. Carbon Nanotube Biosensors. *Front. Chem.* **2015**, *3* (October), 1–21.
(108) Cui, X.; Wan, B.; Yang, Y.; Ren, X.; Guo, L. H. Length Effects on the Dynamic Process of Cellular Uptake and Exocytosis of Single-Walled Carbon Nanotubes in Murine Macrophage Cells. *Sci. Rep.* **2017**, *7* (1), 1–13.
(109) Parakalan, R.; Jiang, B.; Nimmi, B.; Janani, M.; Jayapal, M.; Lu, J.; Tay, S. S. W.; Ling, E. A.; Dheen, S. T. Transcriptome Analysis of Amoeboid and Ramified Microglia Isolated from the Corpus Callosum of Rat Brain. *BMC Neurosci.* **2012**, *13* (1), 1.
(110) Wörle-Knirsch, J. M.; Pulskamp, K.; Krug, H. F. Oops They Did It Again! Carbon

Nanotubes Hoax Scientists in Viability Assays. *Nano Lett.* **2006**, *6* (6), 1261–1268.
(111) Wang, G.; Zhang, J.; Dewilde, A. H.; Pal, A. K.; Bello, D.; Therrien, J. M.; Braunhut, S. J.; Marx, K. A. Understanding and Correcting for Carbon Nanotube Interferences with a Commercial LDH Cytotoxicity Assay. *Toxicology* **2012**, *299* (2–3), 99–111.
(112) Manzetti, S.; Gabriel, J.-C. P. Methods for Dispersing Carbon Nanotubes for Nanotechnology Applications: Liquid Nanocrystals, Suspensions, Polyelectrolytes, Colloids and Organization Control. *Int. Nano Lett.* **2019**, *9* (1), 31–49.
(113) Pinals, R. L.; Yang, D.; Rosenberg, D. J.; Chaudhary, T.; Crothers, A. R.; Iavarone, A. T.; Hammel, M.; Landry, M. Quantitative Protein Corona Composition and Dynamics on Carbon Nanotubes in Biological Environments. *Angew. Chemie* **2020**. https://doi.org/10.1002/anie.202008175.
(114) Jena, P. V.; Roxbury, D.; Galassi, T. V.; Akkari, L.; Horoszko, C. P.; Iaea, D. B.; Budhathoki-Uprety, J.; Pipalia, N.; Haka, A. S.; Harvey, J. D.; Mittal, J.; Maxfield, F. R.; Joyce, J. A.; Heller, D. A. A Carbon Nanotube Optical Reporter Maps Endolysosomal Lipid Flux. *ACS Nano* **2017**, *11* (11), 10689–10703.
(115) Findlay, M. R.; Freitas, D. N.; Mobed-Miremadi, M.; Wheeler, K. E. Machine Learning Provides Predictive Analysis into Silver Nanoparticle Protein Corona Formation from Physicochemical Properties. *Environ. Sci. Nano* **2018**, *5* (1), 64–71.
(116) Mohammad-beigi, H.; Hayashi, Y.; Zeuthen, C. M.; Eskandari, H.; Scavenius, C.; Juul-madsen, K.; Vorup-jensen, T.; Enghild, J. J.; Sutherland, D. S. Mapping and Identification of Soft Corona Proteins at Nanoparticles and Their Impact on Cellular Association. *Nat. Commun.* **2020**, *11* (4535).
(117) Shliaha, P. V.; Bond, N. J.; Gatto, L.; Lilley, K. S. Effects of Traveling Wave Ion Mobility Separation on Data Independent Acquisition in Proteomics Studies. *J. Proteome Res.* **2013**, *12* (6), 2323–2339.
(118) Distler, U.; Kuharev, J.; Navarro, P.; Levin, Y.; Schild, H.; Tenzer, S. Drift Time-Specific Collision Energies Enable Deep-Coverage Data-Independent Acquisition Proteomics. *Nat. Methods* **2014**, *11* (2), 167–170.
(119) Plumb, R. S.; Johnson, K. A.; Rainville, P.; Smith, B. W.; Wilson, I. D.; Castro-Perez, J. M.; Nicholson, J. K. UPLC/MSE; a New Approach for Generating Molecular Fragment Information for Biomarker Structure Elucidation. *Rapid Commun. Mass Spectrom.* **2006**, *20* (13), 1989–1994.
(120) Neilson, K. A.; Ali, N. A.; Muralidharan, S.; Mirzaei, M.; Mariani, M.; Assadourian, G.; Lee, A.; Van Sluyter, S. C.; Haynes, P. A. Less Label, More Free: Approaches in Label-Free Quantitative Mass Spectrometry. *Proteomics* **2011**, *11* (4), 535–553.
(121) Nahnsen, S.; Bielow, C.; Reinert, K.; Kohlbacher, O. Tools for Label-Free Peptide Quantification. *Mol. Cell. Proteomics* **2013**, *12* (3), 549–556.
(122) Silva, J. C.; Gorenstein, M. V.; Li, G. Z.; Vissers, J. P. C.; Geromanos, S. J. Absolute Quantification of Proteins by LCMSE: A Virtue of Parallel MS Acquisition. *Mol. Cell. Proteomics* **2006**, *5* (1), 144–156.
(123) Simon, D. F.; Domingos, R. F.; Hauser, C.; Hutchins, C. M.; Zerges, W.; Wilkinson, K. J. Transcriptome Sequencing (RNA-Seq) Analysis of the Effects of Metal Nanoparticle Exposure on the Transcriptome of Chlamydomonas Reinhardtii. *Appl. Environ. Microbiol.* **2013**, *79* (16), 4774–4785.
(124) Gliga, A. R.; Di Bucchianico, S.; Lindvall, J.; Fadeel, B.; Karlsson, H. L. RNA-Sequencing Reveals Long-Term Effects of Silver Nanoparticles on Human Lung Cells. *Sci. Rep.* **2018**,

8 (1), 1–14.
(125) Bussy, C.; Al-Jamal, K. T.; Boczkowski, J.; Lanone, S.; Prato, M.; Bianco, A.; Kostarelos, K. Microglia Determine Brain Region-Specific Neurotoxic Responses to Chemically Functionalized Carbon Nanotubes. *ACS Nano* **2015**, *9* (8), 7815–7830.
(126) Law, C. W.; Chen, Y.; Shi, W.; Smyth, G. K. Voom: Precision Weights Unlock Linear Model Analysis Tools for RNA-Seq Read Counts. *Genome Biol.* **2014**, *15* (2), 1–17.
(127) Akashi, S.; Saitoh, S. I.; Wakabayashi, Y.; Kikuchi, T.; Takamura, N.; Nagai, Y.; Kusumoto, Y.; Fukase, K.; Kusumoto, S.; Adachi, Y.; Kosugi, A.; Miyake, K. Lipopolysaccharide Interaction with Cell Surface Toll-like Receptor 4-MD-2: Higher Affinity than That with MD-2 or CD14. *J. Exp. Med.* **2003**, *198* (7), 1035–1042.
(128) Robinson, M. D.; McCarthy, D. J.; Smyth, G. K. EdgeR: A Bioconductor Package for Differential Expression Analysis of Digital Gene Expression Data. *Bioinformatics* **2009**, *26* (1), 139–140.
(129) McCarthy, D. J.; Chen, Y.; Smyth, G. K. Differential Expression Analysis of Multifactor RNA-Seq Experiments with Respect to Biological Variation. *Nucleic Acids Res.* **2012**, *40* (10), 4288–4297.
(130) Alexa, A.; Rahnenführer, J. TopGO: Enrichment Analysis for Gene Ontology. **2019**, *R package*.
(131) Alexa, A.; Rahnenführer, J.; Lengauer, T. Improved Scoring of Functional Groups from Gene Expression Data by Decorrelating GO Graph Structure. *Bioinformatics* **2006**, *22* (13), 1600–1607.
(132) Subramanian, A.; Tamayo, P.; Mootha, V. K.; Mukherjee, S.; Ebert, B. L.; Gillette, M. A.; Paulovich, A.; Pomeroy, S. L.; Golub, T. R.; Lander, E. S.; Mesirov, J. P. Gene Set Enrichment Analysis: A Knowledge-Based Approach for Interpreting Genome-Wide Expression Profiles. *Proc. Natl. Acad. Sci. U. S. A.* **2005**, *102* (43), 15545–15550.
(133) Liberzon, A.; Birger, C.; Ghandi, M.; Mesirov, J. P.; Tamayo, P. The Molecular Signatures Database (MSigDB) Hallmark Gene Set Collection. *Cell Syst.* **2016**, *1* (6), 417–425.
(134) Halleskog, C.; Mulder, J.; Dahlström, J.; Mackie, K.; Hortobágyi, T.; Tanila, H.; Kumar Puli, L.; Färber, K.; Harkany, T.; Schulte, G. WNT Signaling in Activated Microglia Is Proinflammatory. *Glia* **2011**, *59* (1), 119–131.
(135) Boitard, M.; Bocchi, R.; Egervari, K.; Petrenko, V.; Viale, B.; Gremaud, S.; Zgraggen, E.; Salmon, P.; Kiss, J. Z. Wnt Signaling Regulates Multipolar-to-Bipolar Transition of Migrating Neurons in the Cerebral Cortex. *Cell Rep.* **2015**, *10* (8), 1349–1361.
(136) Miyoshi, J.; Takai, Y. Structural and Functional Associations of Apical Junctions with Cytoskeleton. *Biochim. Biophys. Acta - Biomembr.* **2008**, *1778* (3), 670–691.
(137) Onoda, A.; Kawasaki, T.; Tsukiyama, K.; Takeda, K.; Umezawa, M. Carbon Nanoparticles Induce Endoplasmic Reticulum Stress around Blood Vessels with Accumulation of Misfolded Proteins in the Developing Brain of Offspring. *Sci. Rep.* **2020**, *10* (1), 1–3.
(138) Amara, U.; Rittirsch, D.; Flierl, M.; Bruckner, U.; Klos, A.; Gebhard, F.; Lambris, J. D.; Huber-Lang, M. Interaction between the Coagulation and Complement System. *Adv. Exp. Med. Biol.* **2008**, *632* (Davis 2004), 71–79.
(139) Dobin, A.; Davis, C. A.; Schlesinger, F.; Drenkow, J.; Zaleski, C.; Jha, S.; Batut, P.; Chaisson, M.; Gingeras, T. R. STAR: Ultrafast Universal RNA-Seq Aligner. *Bioinformatics* **2013**, *29* (1), 15–21.
(140) G, K.; Sukhov, V.; Sergushichev, A. Fast Gene Set Enrichment Analysis. *bioRxiv* **2019**.
(141) Meyers, S. R.; Grinstaff, M. W. Biocompatible and Bioactive Surface Modifications for

Prolonged in Vivo Efficacy. *Chem Rev* **2012**, *112* (3).
(142) Bhirde, A. A.; Patel, S.; Sousa, A. A.; Patel, V.; Molinolo, Y. J.; Leapman, R. D.; Gutkind, J. S.; Rusling, J. F. Distribution and Clearance of PEG-Single-Walled Carbon Nanotube Cancer Drug Delivery Vehicles in Mice. *Nanomedicine* **2010**, *5* (10), 1535–1546.
(143) Wang, J.; Shea, M. J.; Flach, J. T.; McDonough, T. J.; Way, A. J.; Zanni, M. T.; Arnold, M. S. Role of Defects as Exciton Quenching Sites in Carbon Nanotube Photovoltaics. *J. Phys. Chem. C* **2017**, *121* (15), 8310–8318.
(144) Zhao, J.; Park, H.; Han, J.; Lu, J. P. Electronic Properties of Carbon Nanotubes with Covalent Sidewall Functionalization. *J. Phys. Chem. B* **2004**, *108* (14), 4227–4230.
(145) Yang, M.; Zhang, M.; Nakajima, H.; Yudasaka, M.; Iijima, S.; Okazaki, T. Time-Dependent Degradation of Carbon Nanotubes Correlates with Decreased Reactive Oxygen Species Generation in Macrophages. *Int. J. Nanomedicine* **2019**, *14*, 2797–2807.
(146) Kagan, V. E.; Kapralov, A. A.; St. Croix, C. M.; Watkins, S. C.; Kisin, E. R.; Kotchey, G. P.; Balasubramanian, K.; Vlasova, I. I.; Yu, J.; Kim, K.; Seo, W.; Mallampalli, R. K.; Star, A.; Shvedova, A. A. Lung Macrophages Digest Carbon Nanotubes Using a Superoxide/Peroxynitrite Oxidative Pathway. *ACS Nano* **2014**, *8* (6), 5610–5621.
(147) Novitsky, T. J. Monitoring and Validation of High Purity Water Systems with the Limulus Amebocyte Lystate Test for Pyrogens. *Parm Eng* **1984**, 21.
(148) Malyala, P.; Singh, M. Endotoxin Limits in Formulations for Preclinical Research. *J. Pharm. Sci.* **2008**, *97* (6), 2041–2044.
(149) Schwarz, H.; Schmittner, M.; Duschl, A.; Horejs-Hoeck, J. Residual Endotoxin Contaminations in Recombinant Proteins Are Sufficient to Activate Human CD1c+ Dendritic Cells. *PLoS One* **2014**, *9* (12).
(150) Brown, G. C. The Endotoxin Hypothesis of Neurodegeneration. *J. Neuroinflammation* **2019**, *16* (1), 180.
(151) Vallhov, H.; Qin, J.; Johansson, S. M.; Ahlborg, N.; Muhammed, M. A.; Scheynius, A.; Gabrielsson, S. The Importance of an Endotoxin-Free Environment during the Production of Nanoparticles Used in Medical Applications. *Nano Lett.* **2006**, *6* (8), 1682–1686.
(152) Yang, M.; Nie, X.; Meng, J.; Liu, J.; Sun, Z.; Xu, H. Carbon Nanotubes Activate Limulus Amebocyte Lysate Coagulation by Interface Adsorption. *ACS Appl. Mater. Interfaces* **2017**, *9* (10), 8450–8454.
(153) Li, Y.; Boraschi, D. Endotoxin Contamination: A Key Element in the Interpretation of Nanosafety Studies. *Nanomedicine* **2016**, *11* (3), 269–287.
(154) Lahiani, M. H.; Gokulan, K.; Williams, K.; Khodakovskaya, M. V.; Khare, S. Graphene and Carbon Nanotubes Activate Different Cell Surface Receptors on Macrophages before and after Deactivation of Endotoxins. *J. Appl. Toxicol.* **2017**, *37* (11), 1305–1316.
(155) Barbosa, G. M.; Fagan, S. B.; Martinez, D. S. T.; Alves, O. L.; Rodrigues Junior, L. C. Lipopolysaccharide Influences on the Toxicity of Oxidised Multiwalled Carbon Nanotubes to Murine Splenocytes in Vitro. *J. Exp. Nanosci.* **2015**, *10* (9), 729–737.
(156) Xu, F.; Sun, L. X.; Zhang, J.; Qi, Y. N.; Yang, L. N.; Ru, H. Y.; Wang, C. Y.; Meng, X.; Lan, X. F.; Jiao, Q. Z.; Huang, F. L. Thermal Stability of Carbon Nanotubes. *J. Therm. Anal. Calorim.* **2010**, *102* (2), 785–791.
(157) Kundu, S.; Wang, Y.; Xia, W.; Muhler, M. Thermal Stability and Reducibility of Oxygen-Containing Functional Groups on Multiwalled Carbon Nanotube Surfaces: A Quantitative High-Resolution Xps and TPD/TPR Study. *J. Phys. Chem. C* **2008**, *112* (43), 16869–16878.
(158) Lakshminarayanan, P. V.; Toghiani, H.; Pittman, C. U. Nitric Acid Oxidation of Vapor

Grown Carbon Nanofibers. *Carbon* **2004**, *42* (12–13), 2433–2442.
(159) Martínez, M. T.; Callejas, M. A.; Benito, A. M.; Cochet, M.; Seeger, T.; Ansón, A.; Schreiber, J.; Gordon, C.; Marhic, C.; Chauvet, O.; Fierro, J. L. G.; Maser, W. K. Sensitivity of Single Wall Carbon Nanotubes to Oxidative Processing: Structural Modification, Intercalation and Functionalisation. *Carbon* **2003**, *41* (12), 2247–2256.
(160) McIntyre, N. S.; Zetaruk, D. G. X-Ray Photoelectron Spectroscopic Studies of Iron Oxides. *Anal. Chem.* **1977**, *49* (11), 1521–1529.
(161) Kallmyer, N. E.; Huynh, T.; Graves, J. C.; Musielewicz, J.; Tamiev, D.; Reuel, N. F. Influence of Sonication Conditions and Wrapping Type on Yield and Fluorescent Quality of Noncovalently Functionalized Single-Walled Carbon Nanotubes. *Carbon* **2018**, *139*, 609–613.
(162) Gangoli, V. S.; Raja, P. M. V.; Esquenazi, G. L.; Barron, A. R. The Safe Handling of Bulk Low-Density Nanomaterials. *SN Appl. Sci.* **2019**, *1* (6), 1–6.
(163) Thomas, P. D.; Campbell, M. J.; Kejariwal, A.; Mi, H.; Karlak, B.; Daverman, R.; Diemer, K.; Muruganujan, A.; Narechania, A. PANTHER: A Library of Protein Families and Subfamilies Indexed by Function. *Genome Res.* **2003**, *13* (9), 2129–2141.